Nanostructuring of SiC for novel defect-based quantum technologies

Gard Momrak Selnesaunet

Thesis presented for the degree of
Master of Science in Materials Science and Nanotechnology
60 credits

Department of Chemistry

UNIVERSITY OF OSLO

Spring 2021

The dude abides

– the Dude

Preface

This thesis is submitted in partial fulfillment of the requirements for the degree of *Master of Science* in Material Science for Energy and Nanotechnology at the University of Oslo. The research presented herein was conducted at the University of Oslo, under the supervision of Professor Lasse Vines and Dr. Marianne Etzelmüller Bathen. The research was performed in the Norwegian Micro- and Nano-Fabrication Facility (MiNaLab), which is a semiconductor cleanroom laboratory at the University of Oslo. The Research Council of Norway is acknowledged for the support to the Norwegian Micro- and Nano-Fabrication Facility, NorFab, project number 295864.

Abstract

Point defects in semiconductors have emerged as viable candidates for quantum-based technologies such as quantum computing, communication, and sensing. The present work is related to quantum compatible point defects in silicon carbide (SiC), particularly the silicon vacancy, a point defect and material system that has received considerable research interest in the last few years.

In this thesis, a fabrication process was developed for producing structures in SiC that can be used as, e.g., waveguides for single-photon emission. This was performed by depositing a SiO_2 layer with plasma chemical vapor deposition (PECVD) on a high purity 4H-SiC wafer. Next, with photolithography, the SiO_2 layer was patterned with a photoresist mask in a reactive ion etching (RIE) step. The patterned SiO_2 layer was then used as a hard mask for a subsequent RIE step, finalizing the photonic device. A thin nickel layer was deposited on the structures with physical vapor deposition (PVD) for the charge-state control through a lift-off process with a photoresist mask. Defect creation was achieved by 21 keV He implantation to a fluence of 1×10^{11} cm^{-2} with an ion implanter. In a scanning electron microscope (SEM), the device morphology showed sharply defined features with almost vertical sidewalls. The diffraction limit from the photolithography resulted in increasingly tilted sidewalls as the structures decreased in size. The optical properties were characterized with cathodoluminescence (CL) spectroscopy and exhibited emission in the V1 and V1' zero-phonon lines (ZPLs) associated with the V_{Si}. Charge-state control of the V_{Si} was identified by enhancing the V_{Si}^{-} CL emission intensity in the depletion region of the Schottky contact, with a reduction in intensity towards the depletion region edge. By utilizing angle-resolved cathodoluminescence (ARCL) spectroscopy, the radiation profiles of the photonic structures were shown to be altered compared to the Lambertian radiation profile of the implanted wafer. Though no electromagnetic wave propagation in discrete modes (waveguiding effect) was observed, the photonic devices enhanced the emission intensity of the V_{Si} in all directions by functioning as a lens with a higher numerical aperture than the wafer, and the lens had characteristics similar to a combination of a solid immersion lens (SIL) and an optical fiber. The findings presented herein are important for further photonic device fabrication in 4H-SiC,

and lay the groundwork for incorporating quantum compatible point defects in electrically driven quantum technology devices.

Acknowledgments (Norwegian)

Først og fremst vil jeg takke min hovedveileder Prof. Lasse Vines for all den gode hjelp jeg har fått. Måten du har engasjert deg i både problemstillingen og resultatene mine har vært ekstremt motiverende og fått meg til å føle meg som en del av en forskningsgruppe. At du av ren nysgjerrighet kom innom etter kontortid bare for å se hvordan CL-målingene mine gikk, det er noe jeg alltid kommer til å huske. Under innspurten har du alltid vært tilgjengelig på mail med dine konstruktive tilbakemeldinger, selv i helger og på kvelder. Jeg kunne ikke vært mer fornøyd med valg av hovedveileder. Tusen takk!

Videre vil jeg takke min fantastiske medveileder Dr. Marianne Etzelmüller Bathen. Du har vært tilgjengelig til alle døgnets tider under innspurten, tusen, tusen takk for det. Dine grundige tilbakemeldinger har løftet kvaliteten på oppgaven betraktelig. Du har en unik evne til å forklare svært vanskelige konsepter på en forståelig måte, du har definitivt vekket min interesse for forskning, og mer spesifikt for kvanteteknologi og halvlederfysikk. Doktorgradsavhandlingen din har vært svært hyppig brukt ressurs, og dannet fundamentet for oppgaven min.

En stor takk til PhD-student Snorre som svarte på utallige av mine ofte dumme spørsmål. Uten din hjelp ville ingen av CL-resultatene mine eksistert. Jeg kommer til å savne CL-øktene våre med prat om alt fra kinesisk politikk til gaming.

Christoph, all hjelpen du har gitt meg i MiNaLaben har vært avgjørende, både i form av opplæring av instrumenter og hjelp med prosessutviklingen. Viktor, du sprer godt humør og trygghet i MiNaLaben. Takk for all hjelp under prossesutvikling og bestråling av prøver. Takk for all CL-hjelp, Jon og Cristian. Robert, takk for hjelp til tillaging av prøver.

Tusen takk til alle masterstudenter på LENS. En spesiell takk til Vetle og Ylva for vår lille bordtennis-Troika. Det har vært en spesiell tid å skrive masteroppgave i. Til tider har jeg vært fraværende på LENS, men dere har passet på at jeg ikke har forsvunnet helt. At dere regelmessig har tatt kontakt for å høre hvordan det går betyr mer enn dere aner.

Jeg ønsker å takke hele LENS for at dere har skapt en forskningsgruppe som inkluderer studentene på en måte som får oss til å føle oss som kolleger. Det har vært en glede å skrive masteroppgave hos dere. Takk alle sammen!

Og sist, men ikke minst, ønsker jeg å takke mine fantastiske venner og familie for at dere beriker livet mitt slik dere gjør. Tusen takk til alle mine fantastiske kolleger på Post 4, dere har vært uverdelige å ha dette rare året. Spesielt takk til deg Kristi, for vårt uventede og givende vennskap. Sebastian, takk for at du har gjort de siste 8 månedene til den mest lærerike perioden i mitt liv. Uten deg hadde jeg aldri vært der jeg er i dag. Anders og Håkon, dere vil alltid være som brødre for meg, uansett hvor dere bor i verden. Vilde, selv om du ikke har tatt del i den siste delen av reisen min, så har du vært helt avgjørende for store deler av den. Du har en unik evne til å få meg til å ville være den beste versjonen av meg selv. Du vil alltid være min muse, min kilde til evig inspirasjon. Ragnhild og Alf, dere har alltid troen på meg og støtter meg i alt, uansett hva. Dere er mine rollefigur både i kjærligheten og i livet. Marie og Erlend, dere er ikke bare mine søsken, men også bestevennene mine. Jeg setter så utrolig stor pris på at jeg kan snakke med dere om absolutt alt. Mamma, Pappa, Marie og Erlend, jeg er så glad i dere.

Takk til dere alle!

Gard Momrak Selnesaunet, 31. mai 2021, Oslo.

Table of contents

Preface iii

Abstract v

Acknowledgements vii

1 Introduction 1

2 Theoretical background 4

2.1 Quantum technology 4
2.2 Semiconductor physics 9
2.2.1 Crystal lattices 9
2.2.2 **k**-space 10
2.2.3 Energy band model 13
2.2.4 Carrier statistics 14
2.3 Defects in semiconductors 17
2.3.1 Single-photon emitters in semiconductors 20
2.3.2 Nitrogen vacancy center in diamond 21
2.4 Silicon carbide as a quantum host material 21
2.4.1 4H-SiC crystal structure 22
2.4.2 Charge-state control of defect energy levels 24
2.5 Waveguides and other photonic structures 25

3 Methods 28

3.1 Device processing 28
3.1.1 Ion implantation 28
3.1.2 Plasma-enhanced chemical vapor deposition 29
3.1.3 Photolithography 29
3.1.4 Reactive ion etching 34
3.1.5 Physical vapor deposition 36
3.2 Defect and device characterization 36

3.2.1 Scanning electron microscopy 36
3.2.2 Cathodoluminescence spectroscopy 38
3.2.3 Angle-resolved cathodoluminescence spectroscopy 40
3.2.4 Stylus profilometer 42

4 Process development 43
4.1 Process flow 43
4.2 Using standard Si-based lithography process 45
4.3 Optimizing the lithography process for 4H-SiC 46
4.4 Optimization of reactive ion etch processes 48
4.4.1 Optimization of RIE for PR mask and SiO_2 49
4.4.2 Optimization of RIE for SiO_2 mask and 4H-SiC 51
4.4.3 RIE of PR and 4H-SiC 55
4.5 Metal deposition 58

5 Results and discussion 60
5.1 Defect generation in the structures 60
5.2 Identification of the silicon vacancy 62
5.3 Optimization of the CL signal 65
5.3.1 Current test 65
5.3.2 Voltage test 67
5.4 Cathodoluminescence measurements of the V_{Si} emission from the structures 69
5.5 Angle-resolved emission from the 4H-SiC structures 72
5.5.1 Angle-resolved cathodoluminescence measurements 72
5.6 Charge-state control of the V_{Si} 80

6 Concluding remarks and further work 85
6.1 Suggestions for further work 86

Appendices 87

A Cylindrical waveguide theory 87

B CASINO simulations 91

C Radiation profiles of structures with r=3 μm and r=2 μm 93

Bibliography 101

Chapter 1

Introduction

Since the invention of the first transistor at Bell Telephone Laboratories in 1947 [1], the computer has drastically changed the way we live our lives. The first silicon transistor created by Texas Instruments a few years later began the ongoing *silicon age* [1]. To this day, the number of transistors in a computer has almost doubled every second year, a trend which is commonly called *Moore's law* [2]. Modern fabrication methods like CMOS 3D sequential integration to design integrated circuits in 3D rather than the traditional 2D are promising for computers [3], but reduced transistor size is still the most critical part of the increase in computing power [4]. The size limit of the transistor will soon be reached [4] and is today the Achilles' heel of Moore's law. Thus, there is a dire need for novel technologies to keep the computer revolution alive.

At the turning point of the 19$^{\text{th}}$ century, it was believed that most of the physics was discovered and that *Newton's laws* governed the universe. After the *ultraviolet catastrophe*, scientists knew there was a massive problem in physics, and thankfully Max Planck solved this problem by describing the radiative energy from a black body as discrete sets of energy called *quanta*. With the help of Einstein to describe the *photoelectric effect* [5], quantum mechanics was born [6]. For many years quantum mechanics was only a theoretical research field, but in recent years quantum-based technologies have been incorporated into functional devices [4][7]. In the first quantum revolution that began over 100 years ago, we tried to understand the world through quantum mechanics. In the second quantum revolution that is happening right now, we are using quantum mechanics to alter the quantum face of our physical world [7]. Richard Feynman famously said that quantum computers would be an effective way to solve computationally difficult problems in physics and chemistry [8]. In 1994, Peter Shor developed a quantum algorithm that would crack advanced encryption algorithms in seconds, problems that the best classical computer would use trillions of years to solve [9].

Recently, in 2019, Google demonstrated practically that a quantum computer of only 53 qubits was capable of outperforming a classical supercomputer [10]. In the last years, there has been an explosive growth in quantum technology, not just quantum computing. Other aspects of technology like communication and sensing will be drastically changed by utilizing quantum mechanics. One day, quantum-based technologies will change the fate of all of us.

The current quantum computers are based on superconducting circuits [10], but several other candidates exist for building quantum-based components such as trapped ions, quantum dots, and point defects in semiconductors. They all have their pros and cons, but as we will see later, point defects in semiconductors have many properties that make them advantageous to quantum computers and other quantum technologies. In the most straightforward sense, a semiconductor is a material that, depending on the conditions, can carry a current of charge carriers. A forbidden energy gap separates the conducting band from the non-conducting band. A point defect can be a foreign species or an inherent fault in the semiconductor. Certain point defects can change the electrical and optical properties of the host material, and these properties have proven to be useful for quantum technologies. The most well-known point defect with quantum properties is the nitrogen-vacancy (NV) center in diamond [11], but because of costly manufacturing and difficulties with device integration [11][4], the hunt for other quantum point defects is still active. One of the promising candidate materials is silicon carbide (SiC). Structurally, SiC is very similar to diamond, and especially the four hexagonal (4H-SiC) polytype hosts multiple promising quantum defects which potentially can be used in quantum computing, quantum sensing, and quantum communication [4]. The silicon vacancy (V_{Si}) is perhaps the most studied [4], and this defect was chosen for further study in this thesis.

The V_{Si} exists in several charge states as the vacancy can trap several charge carriers [12]. The singly negative vacancy (V_{Si}^{-}) has been shown to exhibit favorable properties for quantum technology applications, including single-photon emission (SPE) at room temperatures [13][4]. The spin of the trapped electron can also be coherently controlled [13], and these properties combined with having optical read-out protocols [4] make the V_{Si} a suitable spin-based qubit system for quantum computers. In order to integrate single spin-based qubits in a more extensive network, they should be efficiently controlled. By creating metal-semiconductor junctions, the charge-state of the defect can be modulated by an external bias [12]. Thus, charge-state modulation can be a method of turning the SPE on/off [14]. Unfortunately, the V_{Si} suffers from relatively weak emission intensities and having no existing entanglement protocols, obstacles that have to be passed before the

V_{Si} can function as an SPE and be used in quantum technologies.

This thesis aims to develop a process for creating devices in 4H-SiC, which hopefully both enhance and modulate the emission of the V_{Si} by photonic structures and charge-state control. As mentioned above, the V_{Si} has low emission intensity, but photonic structures can be an approach to modulate and increase the emission in specific directions [15]. The (V_{Si}^-) is preferentially chosen by charge-state manipulation [12], possibly enhancing the defect emission intensity. The research in this thesis was performed in the MiNaLab by developing and optimizing such a device fabrication process. The material system used in this thesis, 4H-SiC, is promising for both quantum technology and power electronics [16]. The research in this thesis is important both for further development of effective fabrication processes of structures in 4H-SiC and to study how photonic structures can influence the defect emission in 4H-SiC.

The thesis is structured so that the reader in Chapter 2 first is introduced to quantum technology and the necessary theory to understand the properties we search for in a quantum point defect. Semiconductors are introduced as a quantum platform, and 4H-SiC and its defects are presented before the charge-state control of defects and photonic structures are explained. Next, in Chapter 3, the different methods for fabricating the devices and later characterize them are outlined. After this, in Chapter 4, the development of the fabrication process is explained. The process development was an iterative and lengthy process, and each step in the fabrication process will be told as a story from the starting point to the end result. Discussions of errors made and changes in process parameters will also be given to inform the reader of how the process was formed and give other researchers the chance to avoid the same mistakes. Finally, the characterization of the constructed devices will be discussed in Chapter 5, along with an analysis of whether the desired properties were achieved.

Chapter 2

Theoretical background

This chapter briefly explains some of the most important quantum technologies (QT), and the underlying principles that enable QT will be given. After introducing QT and their role in the technological revolution, a more rigorous treatment of semiconductor theory will pave the way for explaining how they can act as QT host materials. Lastly, 4H-SiC and its promising point defects are introduced before an explanation of how they can be incorporated in devices promising for QTs finishes this chapter.

2.1 Quantum technology

We are currently in the midst of a *second quantum revolution*. Over the last 70 years, there has been an extraordinary increase in all aspects of technology, especially in computer technology, integrated circuit technology, and communication technology. The problem these technologies/branches are facing is that the basic building blocks they use, like the transistor in an integrated circuit, are approaching the size of single atoms simultaneously as the human thirst for improvement demands faster, more powerful technologies. In this size domain, the *de Broglie* wavelength, or *matter* wavelength, can no longer be neglected, and the exotic quantum laws become significant and even dominating. This also means that we can utilize these laws in order to improve our current technologies. From the turn of the 19th century to the present day, there have been established six important quantum principles which we can utilize for quantum technologies [17]:

1. **Quantization of energy** This means that energy levels are no longer continuous, and in quantum systems, these levels are restricted to discrete sets.
2. **Heisenberg uncertainty principle** If at least one measurement of a quantum state is completely certain, there exists at least one uncertain mea-

surement.

3. **Superposition** If there can be two or more outcomes to an event, the system is in a superposition of each outcome simultaneously until it is measured. When a measurement is made, the system collapses into one of the outcomes. Two quantum states can also be superimposed without affecting each other, like two waves traveling against each other and colliding.
4. **Entanglement** The superposition principle applied to more than one system. For example, two quantum systems can be coupled so that a measurement on one of the systems forces a change to the other system.
5. **Tunneling** A particle can be found in a classically forbidden region.
6. **Decoherence** Loss of information from a quantum system to the environment, for example, loss of superposition after a measurement.

For a more elaborate explanation of these phenomena, *Introduction to Quantum Mechanics* by Griffiths [17] or a similar under-graduate level book on quantum mechanics is recommended to the reader. Key technologies where these principles are either already in use or on the rise are quantum computing, quantum cryptography and communication, and quantum sensing.

Quantum computers

As mentioned in the introduction, the emerging quantum computer can outperform a classical computer at certain computations, some of which until recently have been practically impossible to solve because of extensive time scales. The classical computers approach their limit at the transistor gate length, which now is at 5 nanometers for the smallest FinFETs [18].

The classical computer is based on boolean logic with a binary number system of either *true* or *false*, usually represented by 1 and 0, respectively. A classical transistor can represent these values by either switching ON (1) or OFF (0) utilizing electrical signals in a circuit. The basic operations in boolean logic are the operations *and*, *or* and *not*, and these operations can be represented by multiple transistors connected in a specific order to make up a *gate* [4]. By creating a vast network of billions of such gates, today's modern computers are realized.

By comparison, the smallest building block in the quantum computer is the quantum bit (qubit), which is a quantum state that by the *superposition* principle can be both 1 and 0 simultaneously, as well as either of the two [4]. The implication of this is that instead of sequentially analyzing a 1 or a 0, a qubit represents both possibilities simultaneously. Extensive networks of qubits can be constructed, and by additionally exploiting the *entanglement* principle, a quantum computer has already outperformed classical computers at a particular task. The state-of-the-art quantum computer is Google's with the Sycamore processor superconducting

qubits based on Josephson's junctions [10].

In order to realize commercial quantum computers, several technological barriers have to be passed. Decoherence of the quantum state is one of the major problems at the present moment. As explained above, decoherence is the loss of the indistinguishable information in the quantum state, and the time for a state to stay coherent is called *coherence time* and is an important metric for the quality of a qubit candidate. For a qubit system to be used in a quantum computer, six other vital criteria have been proposed by DiVincenzo [19], and Bathen [4] has summarized these and other important ideas from Ref. [20] and [21] and made a list of properties which a functional qubit system in a logic-gate based QC should have. The qubit system should have

1. a two-level quantum system with discrete energy levels
2. a system that is practically isolated from the environment with coherence times long enough to execute computations
3. an optically initialized cycle
4. a proven read-out mechanism
5. an established material platform that can be large-scale fabricated and inegrated into devices.

Several promising qubit candidates already exist who can meet these criteria, and the most important will be outlined here.

Single photons Single photons in an optical fiber cable have a polarization state, and by exploiting the fact that this polarization state can be rotated, single-qubit gates can be created [20]. Although single photons have advantages like low decoherence, several technological barriers must be surpassed, such as effective single-photon sources before QC can be based on these qubits [4].

Superconducting Josephson junctions As already mentioned, the state-of-the-art QC has a processor based on a superconducting circuit with Josephson junctions [10]. A Josephson junction in the most general form is composed of two superconductors separated by an insulator. A superconductor has the property of conducting electricity without any loss below a *critical* temperature because Cooper-pairs are formed through an attraction between electrons [4][22]. One of the advantages of Josephson junctions is that instead of being confined to qubits with parameters set by nature, the qubits are realized in an electrical circuit with resemblance to how modern integrated circuits are made. This makes it possible to alter the parameters of the qubit considerably more straightforward than for other types of qubits [23]. The Josephson junction is very promising and, today, the strongest competitor in the QC race. However, it still suffers from short coherence

times and low operating temperatures (mK) [4], motivating the continued search for other qubit systems.

Trapped atoms and ions Ions and atoms can be isolated by electric fields or lasers, respectively, and the resulting qubits have discrete internal energy levels [20]. They can be entangled and initialized by lasers [4]. Like the other qubit systems, they require low temperatures, and scaling to a more extensive system is challenging [4].

Quantum dots Quantum dots (QDs) can be realized in various materials, but here we consider the QDs in semiconductors. By making nanoscale structures in a semiconductor, artificial atoms called quantum dots can be made, either as junctions or self-assembled nanoparticles [4]. The small junctions create potentials within the band gap, which can trap electrons or holes to discrete energy levels [4], similar to the famous electron in a box situation [17]. The discrete energy levels in the QD can be optically initialized and read-out. They have similar properties as the trapped ions and atoms but do not require a method of confinement [4]. However, QDs have their limitations because the fabrication of the self-assembled QDs does not create similar-sized particles, resulting in different energy levels of the QDs [4][20]. The exchange interaction of the junction-type QDs is short-ranged and limits entanglement on a larger scale [4].

Point defects in semiconductors So far, qubits based on different platforms have been introduced. They all have pros and cons, from qubit properties and operating conditions to scalability and fabrication ease, but point defects in semiconductors have properties that make them advantageous in QTs like cryptography, computing, and sensing [4]. Similar to QDs, semiconductor point defects have optical transitions that are restricted to discrete energies and manipulable coherent spin states. However, point defects can achieve substantially longer spin coherence times, and some defect-based qubits can even operate at ambient temperatures [4][15]. Defect-based qubits are also available in well-known materials such as diamond and SiC, and some of these materials already have established fabrication of high-quality wafers [15]. These properties are auspicious, e.g., for a commercial quantum computer.

Quantum communication and cryptography

When exchanging information with a counterpart over distances, we want the information conveyed to be secret to an uninvited third party. In order to secure the message, different encryption protocols can be used. In modern communication, one of the standard protocols is the public key distribution (PKD). The tradi-

tional PKD exploits trapdoor functions to encrypt the meaning of the message [24]. A trapdoor function is a mathematical problem that is easy to compute in one direction, but the inverse is very difficult and computationally demanding [25]. By creating keys based on these trapdoor functions, the sender (in cryptography often called Alice) can send a private key to the receiver (called Bob), decrypting the messages received from Alice. There are many different key exchange schemes, each with its strengths and weaknesses, but all have in common that they are based on these trapdoor functions [24][26][27]. With the emerging quantum computer, this is a problem because the inverse part of the trapdoor function that protects the keys' integrity is expected to be easily computed by a quantum computer [4]. Luckily, there are already quantum cryptography solutions in use to provide safe communication for the future.

One of the novel and active quantum cryptography solutions are quantum key distribution (QKD) systems. In QKD, the communication channel is initially only used to send random bits between Alice and Bob without using any pre-existing secret keys. If the bits sent are quantum states, any measurement on the bits will destroy the *superposition* of the states. This means that any eavesdropping of the message can be detected, and Alice and Bob can agree to use the shared secret bits as an encryption key if the message is uninterrupted. The polarization of photons is are already in use in QKD as a transmitted quantum state and allows the distribution of information across long distances with an indecipherable communication path ensured by the *uncertainty* principle [24]. The no-cloning theorem ensures that an eavesdropper can not simply copy and retransmit the quantum state without being detected [26].

So far, the major obstacle for realizing quantum communication is the limitation on the distance that the photons can travel before the optical loss is too significant. The limit is at 300 km because the current optoelectronic circuits that amplify the light beam in an optical fiber will destroy the quantum states of the photons [22][4]. The concept of a quantum repeater is a hot topic, and hopefully, soon, we will be able to safely communicate over long distances with repeaters that exploit the principles of entanglement, superposition, and no-cloning [28].

Quantum sensing

Quantum sensing offers detection of physical quantity with nanoscale resolution by exploiting the sensitive nature of quantum states [22]. Quantum sensors utilize quantum objects with quantized energy levels or quantum coherence or quantum entanglement to measure physical quantities, e.g., temperature, pressure, and electromagnetic fields [29]. Degen *et al.* have put forth a set of required attributes for a quantum system to function as a quantum sensor, including three of the original DiVincenzo criteria. The quantum sensor object should (i) exhibit a dis-

crete two-level energy system, (ii) be coherently manipulable, (iii) have a proven initialization, and read-out mechanism, and (iv) must interact with the relevant physical quantity. (i) and (iii) are not strict requirements for all quantum sensors. Examples of quantum sensors are atomic spins in neutral atoms, trapped ions, superconducting circuits, and solid-state spins and single photon emitters in semiconductors [29]. Solid-state spin systems include deep level point defects in semiconductors like the NV center in diamond, which with its long spin coherence time is promising for, e.g., magnetic imaging [29][30]. Other host materials like silicon carbide contain several point defects with high electron spin states that can be addressed optically, possess single-photon emission capabilities [30][4], and can be used in quantum sensors for magnetometry, thermometry, electrometry, and strain [30], but are also promising for use in quantum communication and quantum computing [4].

Thus, point defects in semiconductors, particularly the silicon vacancy in SiC, are the topic of this thesis, warranting a more thorough introduction to semiconductors and point defects.

2.2 Semiconductor physics

2.2.1 Crystal lattices

Solid materials manifest themselves mainly in two types of configurations, namely amorphous materials, which have no periodic long range order, or crystalline materials, which have a periodicity. Because of the periodicity of the crystal structure, any two equivalent points in the crystal are identical, and the arrangement of the atoms in the crystal is called the lattice. The lattice is a symmetrical grid, and if we define a basis which contains a repeating unit of atoms, the whole crystal can be reproduced where the crystal lattice is said to have translational symmetry. The smallest repeating unit is called *the primitive unit cell*. The primitive unit cell consists of *primitive* vectors which span the lattice and are given by

$$\boldsymbol{R} = n_1\boldsymbol{a_1} + n_2\boldsymbol{a_2} + n_3\boldsymbol{a_3}, \tag{2.1}$$

where $n_i,\ i = 1, 2, 3$ are integers. There are infinte possibilities on how to describe a crystal structure, but in 3 dimensions there exist 14 unique unit cells that with translational symmetry can describe any lattice. These are called *Bravais lattices*. The hexagonal primitive unit cell is shown in Figure 2.1.

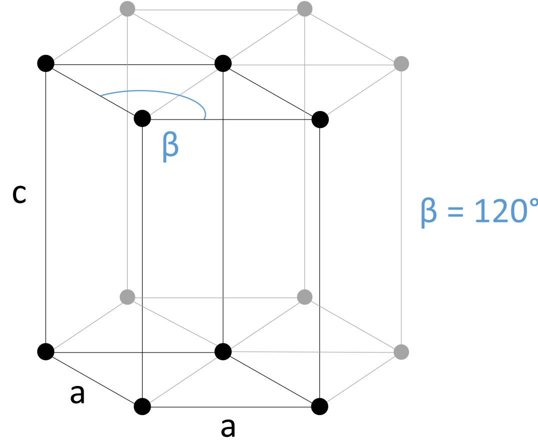

Figure 2.1: Hexagonal bravais lattice.

2.2.2 k-space

To furher explore the crystal symmetry, we first consider the general Schrödinger equation of the crystalline material,

$$\left(-\frac{\hbar^2\nabla^2}{2m_e}+V(\boldsymbol{r})\right)\Psi(\boldsymbol{r})=E\Psi(\boldsymbol{r}). \tag{2.2}$$

Since the crystal structure has a well defined periodicity, the potential of the crystal will be perodic, i.e., $V(\boldsymbol{r})=V(\boldsymbol{r}+\boldsymbol{R})$, where $\boldsymbol{r}$ is a continuous vector in real space and $\boldsymbol{R}$ is given by Eq. (2.1). Because the cystal potential is periodic, it is convenient to use Fourier analysis as a tool to describe the crystal lattice. We have

$$V(\boldsymbol{r})=\sum_{\boldsymbol{G}}V_{\boldsymbol{G}}e^{i\boldsymbol{G}\cdot\boldsymbol{r}}, \tag{2.3}$$

where $\boldsymbol{G}$ will be introduced shortly. Hence,

$$V(\boldsymbol{r}+\boldsymbol{R})=\sum_{\boldsymbol{G}}V_{\boldsymbol{G}}e^{i\boldsymbol{G}\cdot(\boldsymbol{r}+\boldsymbol{R})}=\sum_{\boldsymbol{G}}V_{\boldsymbol{G}}e^{i\boldsymbol{G}\cdot\boldsymbol{r}}e^{i\boldsymbol{G}\cdot\boldsymbol{R}}=\sum_{\boldsymbol{G}}V_{\boldsymbol{G}}e^{i\boldsymbol{G}\cdot\boldsymbol{r}}=V(\boldsymbol{r}),$$

which is only true if

$$e^{i\boldsymbol{G}\cdot\boldsymbol{R}}=e^{(m_1\boldsymbol{b_1}+m_2\boldsymbol{b_2}+m_3\boldsymbol{b_3})\cdot(n_1\boldsymbol{a_1}+n_2\boldsymbol{a_2}+n_3\boldsymbol{a_3})}=1. \tag{2.4}$$

$\boldsymbol{G}$ is defined as the reciprocal lattice vector $\boldsymbol{G}=m_1\boldsymbol{b_1}+m_2\boldsymbol{b_2}+m_3\boldsymbol{b_3}$ with integers $m_i,\ i=1,2,3$. Additionally,

$$\boldsymbol{b_1} = \frac{2\pi \ \boldsymbol{a_2} \times \boldsymbol{a_3}}{V} \qquad \boldsymbol{b_2} = \frac{2\pi \ \boldsymbol{a_3} \times \boldsymbol{a_1}}{V} \qquad \boldsymbol{b_1} = \frac{2\pi \ \boldsymbol{a_1} \times \boldsymbol{a_2}}{V} \qquad , \tag{2.5}$$
$$\text{with} \qquad V = \boldsymbol{a_1} \cdot (\boldsymbol{a_2} \times \boldsymbol{a_3})$$

can be constructed from the primitive unit vectors in real space. The reciprocal vectors $\boldsymbol{b_1}$, $\boldsymbol{b_2}$ and $\boldsymbol{b_3}$ span the reciprocal space. The choice of using reciprocal space instead of real space is a choice, however a very convenient one. We can define an area, called the *Wigner-Seitz cell* (WS), as the primitive cell which contains only one atom. The Wigner-Seitz cell is the locus of all points that are closer to the atom than to any other atom, and it will always have the same symmetry as the Bravais lattice it is constructed from. By transforming the WS cell to reciprocal space by using Eq. (2.5) we get the WS cell of reciprocal space, which is called the *Brillouin zone* (BZ). Both are shown in Figure 2.2 [31].

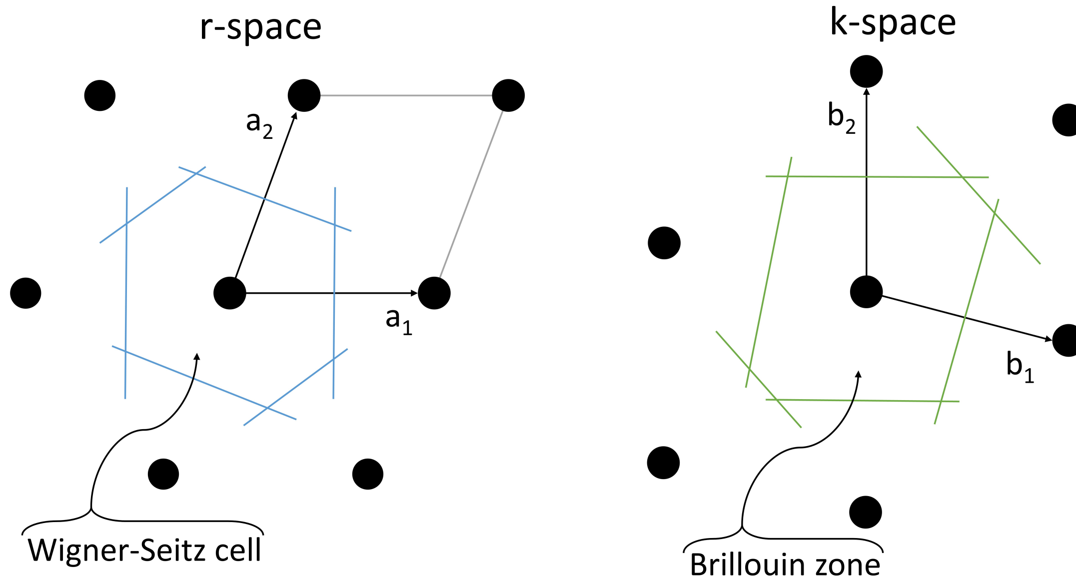

Figure 2.2: Wigner-Seitz cell and 1st Brillouin zone with primitive unit vectors.

Electrons in high energy states are called *valence electrons*, and are said to be delocalized over the lattice. With the right assumptions their wave functions can be written as

$$\psi_{n\boldsymbol{k}}(\boldsymbol{r}) = u_{n\boldsymbol{k}}(\boldsymbol{r})e^{i\boldsymbol{k}\cdot\boldsymbol{r}}. \tag{2.6}$$

Here, $u_{n\boldsymbol{k}}(\boldsymbol{r})$ is a so called Bloch period part, and $\boldsymbol{k}$ refers to the $\boldsymbol{k}$'th state and

$\boldsymbol{n}$ is the band index. The wave vector is $\boldsymbol{k} = \frac{2\pi}{a}$ where a is the lattice spacing. Eq. (2.6) is called Bloch's theorem, and states that the wave functions of the electrons can be considered as plane waves with a periodic modulating function. The modulating function $u_{n\boldsymbol{k}}(\boldsymbol{r})$ obey the same periodicity as the potential, namely $u_{n\boldsymbol{k}}(\boldsymbol{r}) = u_{n\boldsymbol{k}}(\boldsymbol{r} + \boldsymbol{R})$. Because of this simplification of the wave functions of the electrons, we find that $\psi_{\boldsymbol{k}}(\boldsymbol{r}) = \psi_{\boldsymbol{k}+\boldsymbol{G}}(\boldsymbol{r})$ and $< p_{\boldsymbol{k}} > = < p_{\boldsymbol{k}+\boldsymbol{G}} >$, where p is the electron momentum. This means that any state $\boldsymbol{k} + \boldsymbol{G}$ outside the Brillouin zone can be represented as a state $\boldsymbol{k}$ inside the BZ, and hence we only need the 1st BZ to describe all properties of the whole crystal. The band index $\boldsymbol{n}$ is used to specify which Brillouin zone the state originate from [31].

By solving Eq. (2.2) for the case $V(\boldsymbol{r}) = 0$ we get the energy eigenvalue $E_{\boldsymbol{k}} = \frac{\hbar^2 \boldsymbol{k}^2}{2m_e}$ for free electrons. However, we also have to include the potential of the cystal, and because the nearly free electrons can be described by a plane wave part, diffraction will occur. The diffraction is described by the *Bragg condition* and given by

$$(\boldsymbol{k} + \boldsymbol{G})^2 = \boldsymbol{k}^2 \qquad \Rightarrow \qquad \boldsymbol{k} = \pm\frac{1}{2}\boldsymbol{G} = \pm\frac{n\pi}{a}, \qquad n = 0, 1, 2, 3, ... \tag{2.7}$$

The Bragg condition is fulfilled at the borders of the Brillouin zone, which means that the periodic crystal potential will force a discontinuity at the BZ borders. If $E \propto \boldsymbol{k}^2$ is plotted, we will have gaps between energy levels at $\pm\frac{n\pi}{a}$, and this gap is commonly called the *band gap*, E_g. The E *vs* $\boldsymbol{k}$ relationship is called the *dispersion relation* [31].

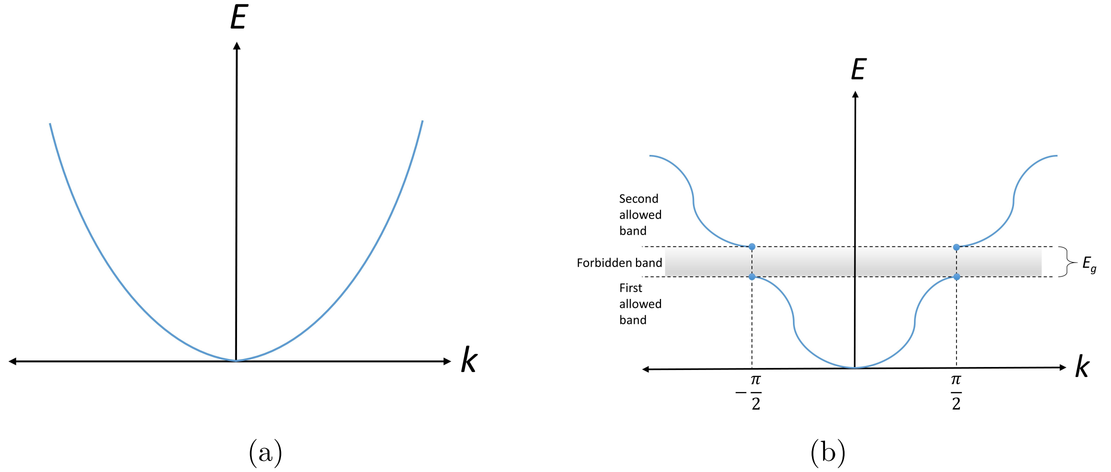

Figure 2.3: (a) shows energy vs **k**-vector for a free electron, while (b) shows the same relationship for an electron in a periodic potential.

These bands will be filled with electrons which behave according to the Pauli exclusion principle. The uppermost occupied energy band is called the *valence band* E_V, while the lowest unoccupied band is called the *conduction band* E_C [31].

2.2.3 Energy band model

The electronic properties of the semiconductor are dominated by the valence and conduction bands, we can therefore limit our analysis of many important effects and properties to a simplified energy band model as the one shown in Figure 2.4. This is a superposition of the (E *vs* $\boldsymbol{k}$) band structure in the x-direction [32], and to the left in the figure is the Fermi-Dirac distribution which will be introduced shortly.

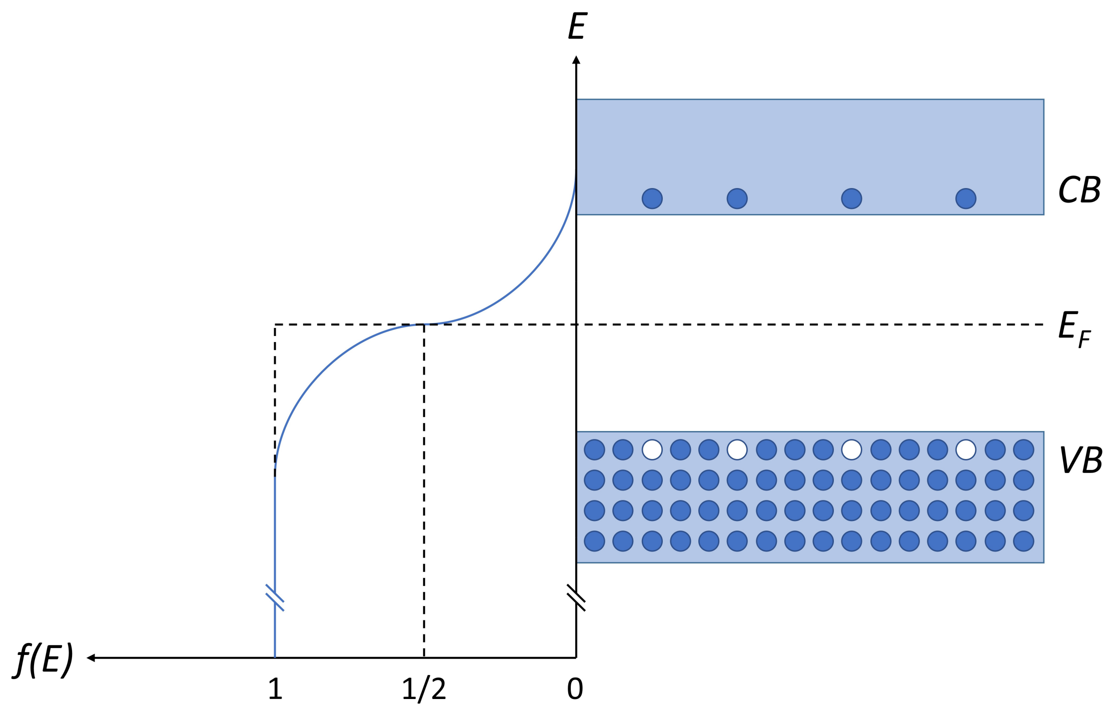

Figure 2.4: To the left is the Fermi-Dirac distribution for temperatures above 0 K. To the right is a simplified band structure, where electrons (blue) are excited from the valence band across the band gap to the conduction band, leaving behind holes (white). A hole is not a real particle, but can be considered as a positive point charge opposite to the electron. The Fermi-Dirac distribution shows that at temperatures T > 0 K, electrons have a probability of occupying avaliable states in the conduction band and holes in the valence band.

2.2.4 Carrier statistics

The population of electron states can be described by the *density of states.* It describes the number of availiable **k**-states in a given **k**-volume with cube sides L, and is given as

$$N(E)\mathrm{d}E = \frac{\sqrt{2}}{\pi^2}\left(\frac{m_e}{\hbar^2}\right)^{\frac{3}{2}} E^{\frac{1}{2}}\mathrm{d}E. \tag{2.8}$$

We observe that we have an $N(E)$ vs E relationship that is parabolic. Each energy level has a propability of being occupied that can be described statistically. Since electrons are fermions which obey the Pauli exclusion principle, the probability is modeled by the Fermi-Dirac distribution

$$f(E) = \frac{1}{e^{(E-E_F)/kT} + 1}\ , \tag{2.9}$$

where k is the Boltzmann constant, T is temperature and E_F is the Fermi level. The Fermi level indicates the energy level which has a probability of 0.5 of being occupied at thermodynamic equilibrium. Figure 2.4 shows how the Fermi-Dirac distribution changes with temperatures above 0 K [32].

We know that semiconductors are able to efficiently conduct electrons in certain scenarios. A pure semiconductor is called an *intrinsic* semiconductor, and the Fermi level is then positioned in the middle of the band gap. If we substitute an atom in the lattice with another element which has either more or fewer valence electrons, the foreign atom will alter the position of the Fermi level by either accepting or donating an electron. The material is then called an *extrinsic* semiconductor. The process of intentionally introducing a foreign species to the lattice is called *doping.* For an intrinsic semiconductor at absolute zero, there is no conduction of electrons because no electrons are thermally excited across the band gap. However, at ambient temperatures electrons can gather enough energy to make the jump to the unoccupied conduction band and traverse the lattice if as they were nearly free. If an electron is excited from the valence band to the CB, it will leave behind a *hole* in the valence band, and this hole can be regarded as a positively charged particle that moves within the valence band. It is of great interest to calculate the concentrations of electrons (n_0) and holes (p_0) in the conduction and valence band, respectively. With Eq. (2.8) and Eq. (2.9) we can calculate the concentration of occupied states. At the conduction band edge, we see that the product $f(E)N(E)$ decreases rapidly at higher energy levels, and similarly, empty states at the valence band edge decrease at lower energy levels. An often used approxaimation is therefore to replace the density of states with an effective density of states at the conduction or valence band edge, reducing the integral above to a product that is easier to calculate;

$$n_0 = \int_{E_C}^{\infty} f(E)N(E)\mathrm{d}E \simeq N_C e^{-(E_C - E_F)/kT} \ , \tag{2.10}$$

$$p_0 = \int_{0}^{E_V} [1 - f(E)]N(E)\mathrm{d}E \simeq N_V e^{-(E_V - E_F)/kT} \ , \tag{2.11}$$

where $N_C = 2\left(\frac{2\pi m_e kT}{h^2}\right)^{3/2}$ is the effective density of states at the conduction band edge and $N_V = 2\left(\frac{2\pi m_h kT}{h^2}\right)^{3/2}$ is the effective density of states at the valence band edge. The Fermi-Dirac distribution is here simplified because kT is 0.026 eV at ambient temperature, and the exponential is therefore much larger than 1. From n_0 and p_0 above we see that the electron/hole concentrations increase as the Fermi level is moved closer to E_C or E_V, respectively. For an intrinsic material, the Fermi level is at some intrinsic level E_i, and since electrons and holes are paired in intrinsic materials ($n_i = p_i$), the electron and hole concentrations are related by [32]

$$n_0 p_0 = n_i^2, \qquad n_i = \sqrt{N_C N_V} e^{-E_g/2kT}. \tag{2.12}$$

Metal-semiconductor junctions

Since all materials have different band structures, it is interesting to examine the effects that occur at the interface between two different materials. As we have seen, in a typical intrinsic semiconductor, the Fermi level is in the middle of the band gap. For a metal, the Fermi level is inside a band, which explains their ability to conduct current. The joining of two different materials is a junction, and in this case a semiconductor-metal junction is formed. Depending on the parameters of the materials used, both rectifying and non-rectifying contacts can be made [32].

The *work function* $q\mathbf{\Phi}$ of a material is defined as the energy required to remove an electron from the Fermi level to vacuum, and when a metal and a semiconductor is joined, there will be a transfer of charge until the Fermi levels of two materials align at equilibrium. At equilibrium the Fermi levels of the two materials are aligned by either lowering or raising of the electrostatic potential of the semiconductor, and this is decided by the difference between $q\mathbf{\Phi}_m$ and $q\mathbf{\Phi}_s$. In Figure 2.5, an n-type semiconductor forms an Schottky barrier with $\mathbf{\Phi}_s < \mathbf{\Phi}_m$. After the charges diffuse from the semiconductor, they leave behind uncompensated donor ions in an area called the *depletion region*, and this region has a width of W. Here we see that an equilibrium potential barrier V_0 is made by joining the two different materials, and V_0 will prevent further diffusion of charges across the junction, thus working as a rectifying contact called a Schottky contact. In the depletion zone, the Fermi level position is shifted with respect to the edges of the band gap. By

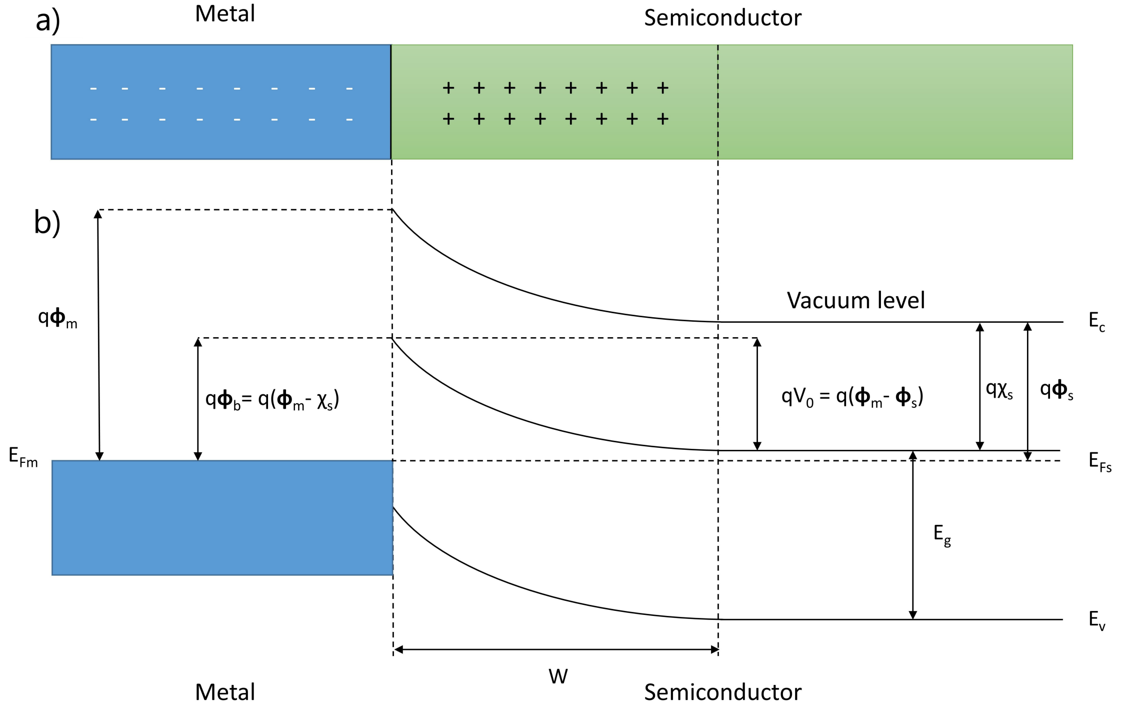

Figure 2.5: a) shows a semiconductor-metal junction where a n-type semiconductor is brought to contact with a metal with a larger work function. Negative charges from the semiconductor flows into the metal, leaving behind uncompansated positive ions. b) shows the equilibrium band diagram of the junction, where $\mathbf{\Phi}_\mathrm{b}$ is the barrier height, $\mathbf{\Phi}_\mathrm{m}$ is the work function of the metal, $\mathbf{\Phi}_\mathrm{s}$ is the work function of the semiconductor, χ_s is the electron affinity of the semiconductor, E_Fm is the metal Fermi level, E_Fs is the semiconductor Fermi level, E_C and E_V are the conduction band and valence bands, respectively, and E_g is the band gap. W is the depletion region width and q is the electron charge.

joining a p-type semiconductor with $\mathbf{\Phi}_s > \mathbf{\Phi}_m$, a Schottky barrier for holes is made instead. By applying a forward-bias voltage to a Schottky barrier, the barrier can be either lowered or raised, and thus the current passing the Schottky barrier can be manipulated [32]. The depletion region width can be calculated by

$$W = \sqrt{\frac{2\varepsilon(\mathbf{\Phi}_m) - V_b}{qN_d}}, \tag{2.13}$$

where ε is the absolute permittivity of the semiconductor, q is the electron charge, N_d is doping of the semiconductor and V_b is the applied bias [32]. As we will see later, interesting effects can occur in the depletion region of junction.

If the junction is composed of an n-type semiconductor and a metal with $\mathbf{\Phi}_s > \mathbf{\Phi}_m$ or a p-type semiconductor and a metal with $\mathbf{\Phi}_s < \mathbf{\Phi}_m$, a non-rectifying contact is formed with a linear $I-V$ relationship according to *Ohm's law* $V = IR$, where V is voltage, I is current and R is resistance. These contacts are called *ohmic* contacts [32] and are very important in integrated circuits, but are less relevant to the work in this thesis.

2.3 Defects in semiconductors

Doping of a semiconductor is the process of introducing a foreign atom to the structure, as stated above. A foreign atom will be an imperfection to the perfect crystal lattice called an extrinsic defect, and will consequently influence the properties of the semiconductor. An intrinsic defect is an impurity that is native to the crystal. There are many different types of defects, both intrinsic and extrinsic, and the defects most important to this thesis will be outlined below.
Point defects are 0-dimensional defects, and consist of vacancies, interstitials, interstitial foreign atoms, substitutional intrinsic atoms (antisites) and substitutional foreign extrinsic atoms (e.g., dopants). Line defects are 1-dimensional defects, and here we have, for instance, a row of point defects or dislocations. Planar defects are 2-dimensional and here the line of point defects can be extended to, e.g., a plane of point defects, such as stacking faults. We also have row of dislocations and grain boundaries. 3-dimensional defects are considered precipitations of separate phases in the crystal lattice [32]. In this thesis we will exclusively consider point defects.

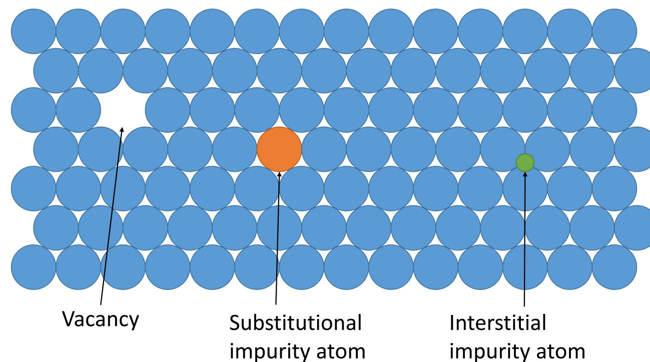

Figure 2.6: Point defects in a crystal lattice.

When a point defect is present, there will consequently be changes in the crystal around the defect. There will be both structural relaxation and electronic modifications. Defects can be electrically active, and if so they introduce energy levels in

the band gap, as shown in Fig. 2.7. Charge carriers can bind to these defects, and depending on the position of the defect energy levels within the band gap, they influence the behaviour of the bound charge carriers, and so also the properties of the semiconductor. Shallow defects are closer to either band gap edge ($\leq$ 0.2 eV) and the bound charge carriers wavefunctions can become *delocalized*, meaning that the hole or electron associated with the defect can be, e.g., thermally excited to the energy bands and contribute to the electronic properties of the semiconductor. Shallow defects can have pronounced effects on the semiconductor such as increasing the concentration of charge carriers, but unwanted dopants can limit or destroy the operation of components. Depending on the band gap energy, deep level defects reside closer to the middle of the energy gap, and charge carriers bound to those have highly *localized* electron wavefunctions. Deep level defects can both capture and trap charge carriers, but they can also behave as recombination centers for EHPs. The defect can capture multiple charge carriers, and the energy levels associated with such a deep level defect is labelled *charge-state transition* levels. Multiple transition levels may be associated with each defect, as shown in Fig. 2.7 for a conceptual defect. The Fermi level defines the prevailing charge state of the defect [4].

So far, only charge carrier energy transitions due to thermodynamics have been considered, but transitions can occur due to excitations by, e.g., electron beams and lasers as well. If the charge carriers are excited by photons we can name the transition an optical transition. Optical transitions are fast, i.e., they are much faster than the motion of atoms and an adiabatic approximation can be used. Based on this approximation, the configuration coordinate (CC) model is used to describe recombination for localized charge carriers [33][4]. Thermodynamic and optical transitions are shown in Fig. 2.7.

For internal energy transitions, the defect absorbs energy, e.g. a photon, and the system is in an excited state (ES). A particularly relevant case for this thesis is when the ES is within the band gap, meaning that the energy difference between GS and ES is less than that of the energy required to excite the charge carrier to the conduction band. This absorption process is approximated as an adiabiatic process, and is indicated by the vertical orange arrow in Fig. 2.7 from A$\rightarrow$B. The charge carrier wave function can be localized at one of the bonds, and if so, will change the symmetry of the surrounding lattice. This atomic relaxation will interact with phonons because of vibrations in the lattice. After exchange of phonons, the charge carrier relaxes to the zero vibrational level of the ES, indicated by B$\rightarrow$C in Fig. 2.7 and rearrengements in the lattice has occured. After some time, the charge carrier relaxes back to the GS by emitting a photon, as shown

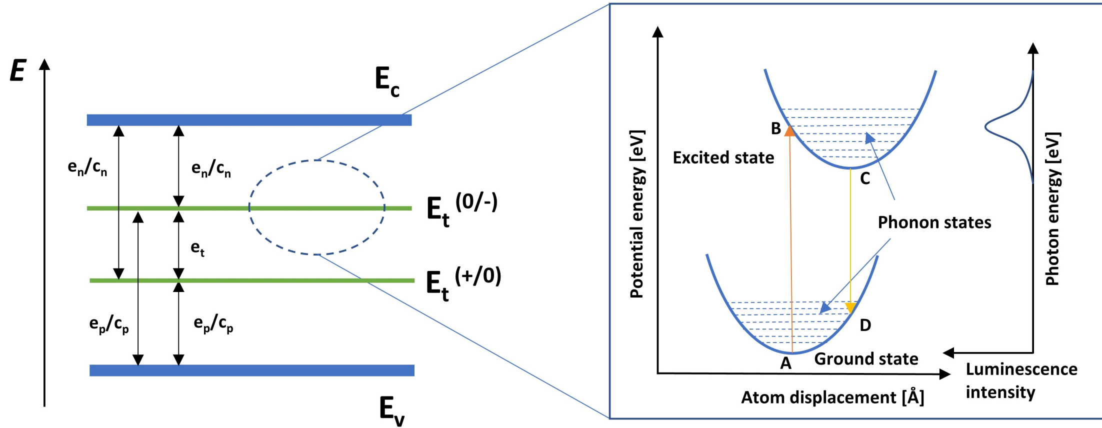

Figure 2.7: To the left is a diagram of the band gap, showing the charge states of a defect. The EHP capture and emission events for electrons and holes are indicated by the arrows and $c_{n/p}$ and $e_{n/p}$, respectively. Transitions between the charge states are indicated by e_t. To the right is a configuration coordinate (CC) diagram showing adiabatically approximated potentials representing the total potential energy of the defect system.

by the yellow arrow in Fig. 2.7 from C→D. Finally the system relaxes to the zero vibrational level of the GS by phonon-interaction, D→A, and the original lattice arrangement is restored. Depending on the electron-phonon coupling of the system, the ES and GS can be displaced so that any excitation and emission processes will include phonons. A direct (vertical transition in Fig. 2.7) energy transition can release a photon with energy corresponding to the energy difference between the ES and GS, but both the ES and GS have multiple vibronic states, and an energy transition typically involves multiple vibronic states. Therefore the radiation energy is reduced by the amount of energy lost to phonon emission [34]. A direct optical transition from the ES to the GS is called a zero-phonon line (ZPL), and the photon energy E_{ZPL} associated with this transition will be a sharp peak in a luminescence spectrum. Energy transitions involving phonon interactions will result in lines at different energies than the ZPL or broader bands called phonon side-bands (PSB) in the same spectrum. In the case of strong electron-phonon coupling, the ZPL will not be visible in the spectrum due to the strong PSB emission. A measure of how much of the emission that is due to the ZPL relative to PSB is the Debye-Waller (DW) factor [35][36]. The luminescence intensity to the right in Fig. 2.7 shows how the emission bands can be broadened due to phonon emission. For a more rigorous treatment of defect states and charge carrier kinetics, the PhD thesis by Bathen [4] is highly recommended to the interested reader.

2.3.1 Single-photon emitters in semiconductors

Each defect charge state can have internal energy transitions with corresponding ES, GS and vibronic states, as well as acting as recombination centers. Charge-carrier transitions can be internal transitions and transitions involving different charge-states and band edges, an all of them can result in luminescence. However, when a single photon is emitted one at a time with a given time delay between each event, the defects that exhibit this property are called single-photon emitters (SPEs). The single-photon emission typically occur when the energy of the internal transition is lower than that of the energy transition between the charge state and one of the bands, as described above. They can have the characteristic ZPL that other defects with ES to GS transitions have, but the single-photon emission is what makes them useful for a range of QT applications [4][11].

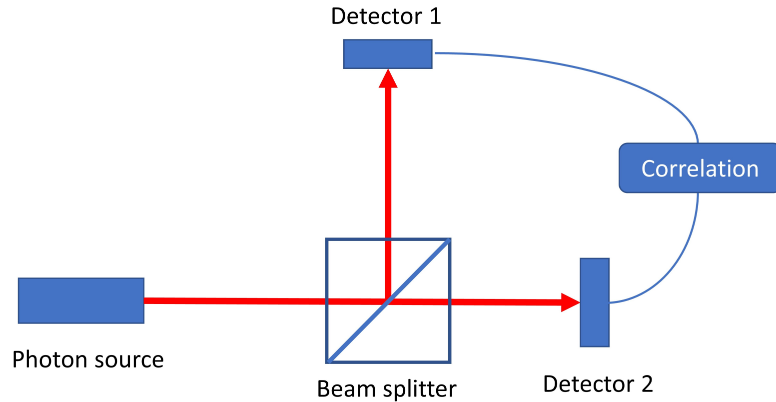

Figure 2.8: Schematic presentation of the Hanbury-Brown and Twiss interferometer. The photon beam is aimed at the 50/50 beam splitter, and the two resulting beams are incident on avalanche photodiodes with single photon measurement capabilities. The detectors are coupled to a counter which measures the time delay between detection events.

A Hanbury-Brown and Twiss interferometer is used to measure if a defect has the characteristics of an SPE. A schematic presentation of how such an experiment is performed is shown in Fig. 2.8. Each detector has the capability of single-photon measurement, and the setup can measure the correlation (bunching) or anticorrelation (anti-bunching) of the emitted photons. When one detector detects a photon, a counter is started. The counter is stopped when the other detector is stimulated, and when repeating this, a histogram of the time delays can be created. A second order correlation function $g^{(2)}(\tau)$ is used and describes the correlation of the intensitites measured at each detector. For $g^{(2)}(0) < 0.5$, the measured photons are not correlated at zero time delay, and are said to be *anti-bunched*. This means

that exactly one photon is emitted at a time, and $g^{(2)}(\tau)$ is a method to measure if, e.g., a defect is an SPE [4][37].

SPEs found in semiconductors have several properties that make them advantagous, such as long coherence times and ambient operating temperatures [4]. The semiconductor host we are looking for should meet the criteria summarized by Bathen [4]. The wavefunction of the charge carrier associated with the defect should be isolated from the environment, so the semiconductor should have a wide band gap, and the defect energy levels should reside deep within the band gap. The material should in addition possess low spin-orbit coupling to provide long coherence times. The ZPL of the SPE should furthermore have a weak electron-phonon coupling to ensure sharp emission peaks. The host material should also be scalable and high purity material should be accesible [4]. With these critera in mind, there exist several candidates. The most known candidate will be introduced, before the host material of this thesis is further explored.

2.3.2 Nitrogen vacancy center in diamond

The most well known quantum point defect system with SPE capabilities is the nitrogen vacancy (NV) center in diamond, which consists of a vacancy with a substitutional nitrogen atom as its closest neighbour [11][38]. The NV center exists in many different charge states, but the NV^0 and NV^- are the only ones found in photoluminescence (PL) spectroscopy, with the negative charge state being most beneficial for QT [38]. Diamond has a wide band gap and low spin-orbit coupling [38], and the NV^- has been shown to be a stable SPE at room temperature [39]. Fabricated devices in diamond have shown to give the NV^- spin very long spin coherence times (1.8 ms) at room temperature [40]. However, because of the expensive manufacturing and difficulties in fabricating devices with diamond [4], and unwanted properties such as low DW factor (4 % at 6 K [41]), other quantum point defect systems are more attractive.

2.4 Silicon carbide as a quantum host material

Silicon carbide was first synthesized over 130 years ago, and its uses range from brake disks to power electronics. The covalent Si-C bonds are strong and SiC therefore has a very high thermal conductivity and stability. It is almost as hard as diamond, which makes it very useful in industry [16]. Due to many of the same properties as diamond, such as a wide band gap, long coherence times and low spin-orbit coupling, with the inclusion of an established production, SiC is a promising candidate as a quantum platform [30]. There are many different types

of defects in SiC, but the defects that are most promising for QT are the silicon vacancy (V_{Si}), the divacancy ($V_{\mathrm{Si}}V_{\mathrm{C}}$), the carbon antisite-vacancy pair ($\mathrm{C_{Si}}V_{\mathrm{C}}$) and the nitrogen vacancy center ($V_{\mathrm{Si}}\mathrm{N_C}$), all found in 4H-SiC. 4H-SiC also has the widest band gap of the SiC crystal variations (3.2 eV) [42][16][4][15].

2.4.1 4H-SiC crystal structure

There exist many different crystal structures for SiC, and we call these different structures *polytypes* of SiC [4][43]. There exist infinte possibilites of how the atoms can arrange in a lattice, but experimentally, over 200 different polytypes of SiC has been made [16]. In this thesis we work with 4H-SiC. As mentioned above, this polytype has the widest band gap. It consists of bilayers of covalently bonded silicon and carbon atoms, stacked on top of each other in the (0001) direction. We can define three different bilayers A, B and C, where A and B are oriented similarly, but are shifted with respect to each other, while bilayer C is rotated 60° with respect to A and B. The bilayers are stacked in a ABCB... sequence, which means there are 4 bilayers. This stacking is shown in Fig. 2.9. The overall unit cell composed of the 4 layers is hexagonal giving the name 4<u>H</u>-SiC. Note that not all atomic sites for the Si and C atoms are equal. Their closest neighbouring atoms are identical for all sites, but the second nearest neighbour may differ. The different types of sites in 4H-SiC are hexagonal sites (h) and quasi-cubic sites (k). Because the (h) and (k) bilayers alternate, both the Si and C atoms have two distinct configurations [4][43].

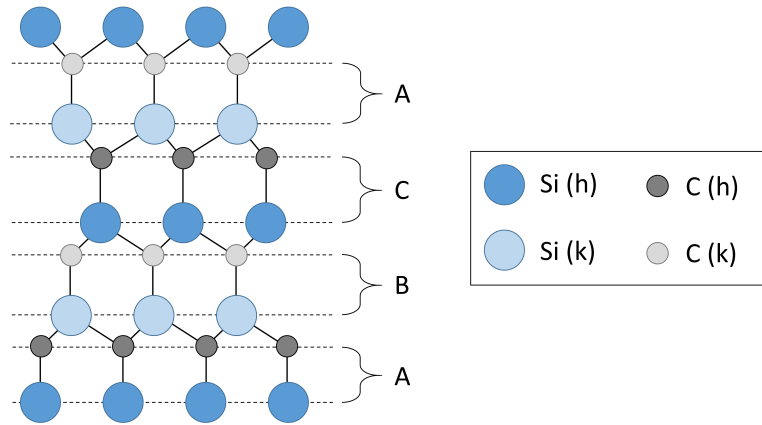

Figure 2.9: 4H-SiC crystal structure and stacking sequence.

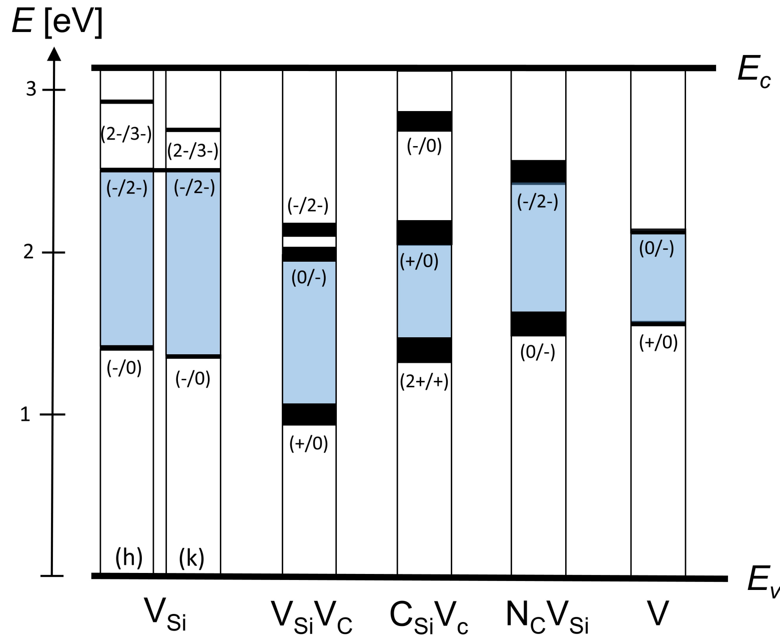

Figure 2.10: Energy levels in the 4H-SiC band gap for the V_{Si}, VV, CAV, NV and V defects and their charge states. The quantum compatible charge state for each defect type is highlighted by the blue-colored regions. See references in Ref. [46]

Silicon vacancy

The V_{Si} has been demonstrated as serving as a SPE with ZPL at cryogenic temperatures at λ_{ZPL}=861 nm (V1), λ_{ZPL}=858 nm (V1') and λ_{ZPL}=917 nm (V2) in PL in the most stable charge state (V_{Si}^-), and can operate as a SPE at room temperature [44][4]. The different V1 and V2 ZPLs occur because there are two inequivivalent V_{Si} sites in 4H-SiC, and the V1' ZPL is from a higher excited state than the V1 for the V_{Si}^-(h) [45][30]. The spin state can also be coherently controlled, and has millisecond spin coherence time [13]. Fuchs *et al.*[44] also found that the defect is extremely stable without any change in charge state after stimulated emission for long time periods.

Divacancy

The $V_{\text{Si}}V_{\text{C}}$ has also been shown to be a SPE, and having very long spin coherence time, even exceeding 1 ms at 20 K [47]. Because the defect is composed of two lattice sites, there exists four inequivalent $V_{\text{Si}}V_{\text{C}}$ configurations, namely (*hh*), (*hk*), (*kh*) and (*kk*)[43]. There are six ZPLs in the infrared regime ($\sim$ 1100 nm), with four of them corresponding to the above mentioned defects, but two of the ZPLs have not yet been identified. These unidentified defects can be coherently controlled by

the same techniques used to manipulate the NV- center in diamond [47].

Carbon antisite-vacancy pair

The $C_{Si}V_C$ is composed of a carbon atom at a silicon site, leaving the neighbouring carbon site vacant. Just like with $V_{Si}V_C$, the defects binary composition results in four different configurations. The defect has eight ZPLs called AB-lines, in the range 648-677 nm due to 4 inequivalent sites with 2 excited states [48][30]. The findings by Castelletto *et al.* also reveal that the ZPLs arise from the positively charged defect $C_{Si}V_C^+$ and that the defect is an ultrabright SPE operating at room temperature [30].

Other defects

There are other quantum emitters in 4H-SiC such as the NV center ($V_{Si}N_C$), similar to the NV center in diamond [49], and vanadium impurity (V) [50], but as they are not relevant to this thesis, they will only be mentioned briefly here.

2.4.2 Charge-state control of defect energy levels

As shown in Figure 2.10 and mentioned in above, not all charge states of a point defect have the properties necessary for functioning as a building block for quantum technology. Because the different charge state transitions are located at different energy levels within the band gap, a shift in the Fermi level means that different charge states can be addressed. A way to change the Fermi level of the semiconductor locally is by forming a Schottky contact, as we have already seen. Figure 2.11 shows how the different charge states in the band gap are repositioned with respect to the Fermi level. The Fermi level depends on the metal used and the doping of the semiconductor used. As we have seen earlier, applying a forward-bias to a Schottky diode can change the Fermi level position even further, and de las Casas *et al.*[14] have done this on the $V_{Si}V_C$ defect in 4H-SiC, and shown that this can be a method for switching the qubit on/off, meaning that it will act as a SPE depending on which charge state it is in. When applying an external electrical field, there can be a splitting of spectral lines called the *Stark effect* [51], and occur because the electric field influences the energy levels of the electron bound to the defect.

To be able to incorporate a quantum system into a larger unit we want it to be controllable. A SPE-based quantum device should include a way to manipulate the charge state of the defect, and a goal of this thesis was to fabricate a process for creating Schottky contacts on structured samples for charge control of the silicon

vacancy. A device should also include a way to manipulate the radiation emitted from the SPE, and such devices will be introduced below.

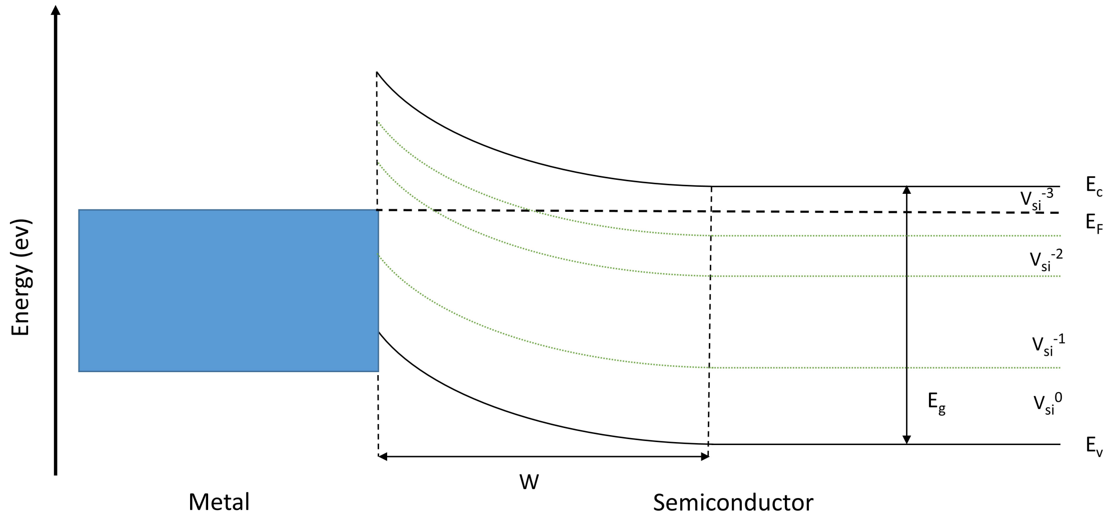

Figure 2.11: Conceptual scheme demonstrating how the carge-state transition levels are altered in the band gap by forming a Schottky barrier with a metal. The semiconductor is n-doped and posesses a work function smaller than the metal. Since the Fermi level position in the band gap is shifted, the probability of a V_{Si}^{-} state being occupied is increased close to the interface. See references in Ref. [12].

2.5 Waveguides and other photonic structures

When a defect with the properties of a SPE is excited, it later emits a photon. For the un-guided case, the defect will to a first approximation emit the photons randomly in every direction possible. If the defect is inside a structure which alters the electromagnetic radiaton the photon emission direction can be very different, similar to how visible light is influenced by lenses and mirrors. The structure can be of any size and dimension, but most interesting to QT applications and SPEs are photonic structures, which have dimensions in the size domain of the photons emitted. Let us consider a cylindrical structure like the one shown in Fig. 2.12.

If the diameter of the structure is large compared to the wavelength of the light, the model of *Geometrical Optics* is sufficient, and the electromagnetic (EM) waves can be considered as rays and are guided in the structure by the principles of total internal reflection [52]. However, when the diameter of the waveguide is comparable to the wavelength of the photons, the wave nature of the photons has to be taken into account, and the EM waves propagate as discrete sets, called modes. By solving *Maxwells equations* for the boundary conditions and physical

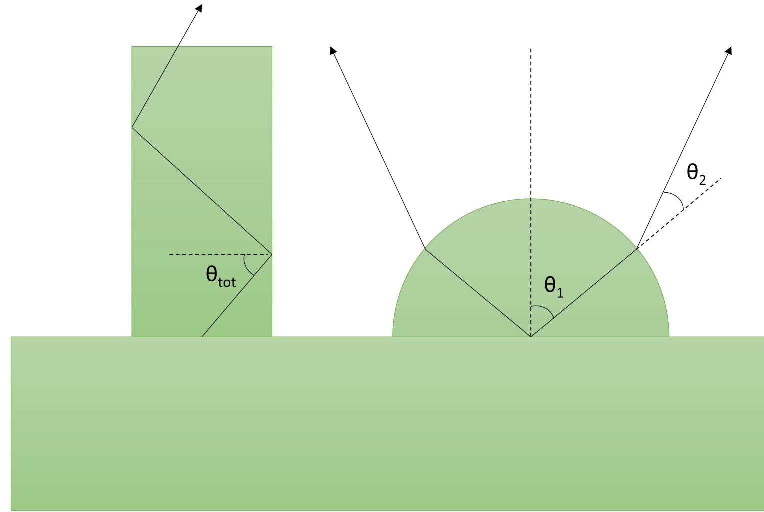

Figure 2.12: To the left is a schematic representation of a cylindrical structure in 4H-SiC. The diameter of the cylinder is much larger than the wavelength of light, thus the light can be considered as rays. Depending on the refractive index of the material, rays incident on the interface material/air at angles larger than a critical angle will be subjective to total internal reflection. To the right is a SIL. The rays will refract depending on where they hit the curved interface. Because more light can leave the lens compared to a flat surface, the numerical aperture is increased.

parameters of the system, these modes can be found [53][52] (see Appendix A for a derivation of the modes of a cylindrical waveguide). EM waves in waveguides have minimal loss of energy because the transmission of energy is restricted to one dimension, and waveguiding in 4H-SiC has shown to increase counts of photons per second (kcps) by up to three-fold for cylindrical waveguides with 600 nm and 1000 nm width and height of 800 nm, compared to bulk [54].

Other structures like solid immersion lenses (SILs) have also been used to influence the radiation characteristics of SPEs in 4H-SiC [55]. SILs are made by e.g. ion milling of the host material and creating a hemispherical surface. This overcomes the problem of materials having a high refractive index by using a curved surface so refraction occurs for angles that otherwise would not escape the interface between the material and outside. A typical hemispherical SIL is shown in Fig. 2.12. Widmann *et al.* found a 4-fold increase in kcps from emission from SILs compared to wafer [13]. SILs in diamond are also promising for enhancing the emission intensity from the NV center [56][57][58].

The development of a fabrication process for photonic structures to increase the yield from the SPEs in 4H-SiC is one of the main goals of this thesis. As we

will see later, 4H-SiC is a challenging material to work with because of its physcial properties which are very similar to diamond. The next chapter will introduce and explain the different methods used to develop a fabrication process and the characterization techniques used to examine the structures made.

Chapter 3

Methods

3.1 Device processing

3.1.1 Ion implantation

Ion implantation is a technique where high energy ions are accelerated and directed to the substrate. The fluence of the ions control how many ions that are incorporated. The ions have kinetic energies up to several MeV, and they interact elastically with the atoms in the lattice, as well as colliding with the surrounding electrons. The term stopping power describes the interaction between the incident ions and the atoms and electrons in the lattice. The stopping power has an electronic and a nuclear contribution. For low implantation velocities, the nuclear part of stopping power dominates, while for high velocities, the electronic part is largest. After collision with the substrate, the ions lose their kinetic energy to the lattice. After the ions lose their energy, they will come to rest at an average penetration depth. Depending on the energy, mass and angle of the ions, the projected range and distribution of implanted ions is determined. The ion distribution will have a nearly Gaussian form around the projected range. This distribution is dependent on random collisions, which do not occur in crystalline materials. Thus, to stop the ions from following pathways in the lattice, the ion beam has to be incident on the sample at an angle not parallel to the surface normal [4].

Ion implantation is a controlled approach to introduce foreign species to the lattice in a controlled manner. However, the collisions can also result in damage to the sample. These damages can manifest themselves as defects in the lattice, and ion implantation is therefore also a method to induce defects in a controllable manner [32]. The dose In this thesis, controlled defect creation was achieved by 21 keV He implantation to a fluence of 1×10^{11} cm^{-2}. This resulted in a projected range for the He ions of 150 nm.

3.1.2 Plasma-enhanced chemical vapor deposition

The Plasma-enhanced chemical vapor deposition (PECVD) system can deposit thin films of a given material on a substrate by introducing vapor which chemically reacts with the surface of the substrate. A typical setup is shown in Fig. 3.1.

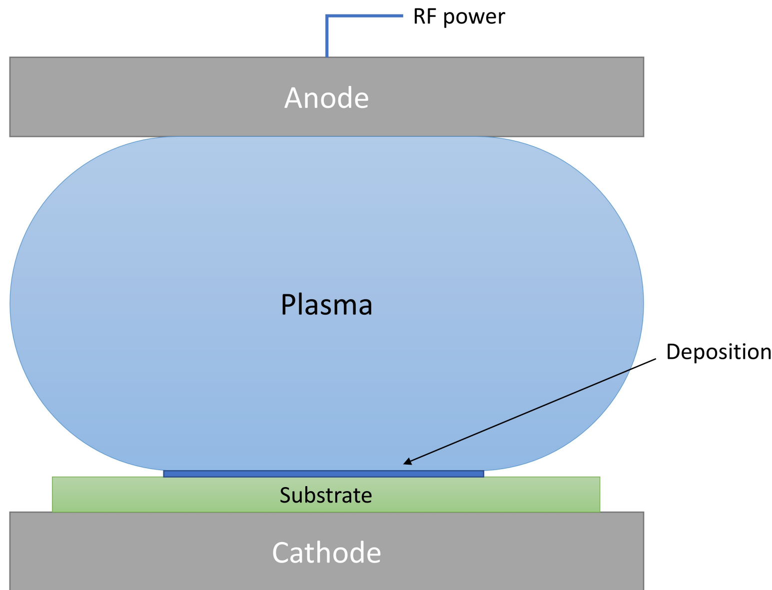

Figure 3.1: Schematic presentation of the PECVD chamber.

In the PECVD chamber, volatile precursors are exposed to the substrate, and they react with the substrate surface. A plasma of the reactants is created to enhance the reaction rates of the volatile precursors. The plasma is made by radio frequency between two electrodes. Volatile by-products can be produced, and they are removed from the chamber [32].

The setup in the MiNaLab is a Advanced Vacuum Vision 310 MK II, and is used mainly for deposition of SiO_2, Si_3N_4 and α-Si. In this thesis, a SiO_2 thin film was used, and it was deposited with a $SiH_4/N_2/N_2O$ gas chemistry at low pressure and 300°C.

3.1.3 Photolithography

Lithography is a printing method to develop an image on a surface. In semiconductor industry, this is a commonly used method to make the microelectronics that we have today. Generally, a chemical (*resist*) is deposited on the substrate, and a mask is typically used to pattern the resist. The resist undergoes chemical

changes where it has been exposed, and depending on the type of resist, the pattern from the mask is transferred to the resist. Depending on the type of resist used, one can use light (near UV to deep UV), ions, x-rays or electrons to induce changes in the resist. After exposure, the resist pattern is developed in a base or a solvent. With the patterned resist, it is possible to, e.g., etch or deposit other materials. This process can be repeated to realize complex nanostructures. When using light, the technique is called *photolithography*, and the most important steps in photolithography will be outlined here [32].

Cleaning

In order to prepare the substrate for photolithography, the wafer is thoroughly cleaned. This is performed to remove dirt or unwanted chemical species. For SiC, a quick and effective cleanse is to ultrasonically bath the wafer in acetone for 10 minutes. For a more comprehensive cleanse, a cleaning process called RCA (Radio Corporation of America) is used. This process is composed of three steps;

1. Submerge the wafer in a chemical solution of $NH_4OH : H_2O_2 : H_2O$ in a 1:1:5 ratio at 80°C for 10 minutes. Use glassware for this step. Rinse the wafer with a 5 minute DI water bubble rinse before the next step.
2. Submerge the wafer in a chemical solution of $HF : H_2O$ in a 1:50 ratio at 25°C for 2 minutes. Use plastic beaker suited for HF. Rinse the wafer with a 5 minute DI water bubble rinse before the next step.
3. Submerge the wafer in a chemical solution of $HCl : H_2O_2 : H_2O$ in a 1:1:5 ratio at 80°C for 10 minutes. Use glassware for this step. Rinse the wafer with a 5 minute DI water bubble rinse.

Dehydration bake

A dehydration bake is performed to remove as much water as possible from the surface. The surface of SiC can have reactive oxides, and these oxides may form hydrogen bonds with water in the air. If the surface is covered with water, the adhesion of the photoresist will be lower because it will bind to the water instead of the substrate.

Primer

As mentioned above, water on the SiC surface is a crucial point for the adhesion of the resist. By using a primer such as hexamethyldisilazane (HMDS), the adhesion of the resist is increased. HMDS works by binding its Si atom to the oxides on, e.g., the SiC surface and releasing ammonia. The methyl groups of the HMDS then create a hydrophobic surface.

Spinning

In order to achieve a desired uniform thickness of the photoresist, the sample (wafer) is held in place by a vacuum pump and then spun at a predetermined revolution per minute (rpm) speed. The photoresist thickness is determined by the spin speed, although each resist behaves differently, depending on its viscosity. The primer is also spun on the wafer in order to cover the wafer uniformly.

Photoresist

Exposure of the resist will induce a chemical change, as mentioned above, and since we are using light, we call the resist a *photoresist* (PR). When the photoresists chemical structure is changed, it will react differently to certain solvents. By using properly chosen solvents, the exposed areas or the unexposed areas can be removed by the solvent. Such solvents are called developers because they highlight parts of the design that are of interest. If the exposed areas are more soluble to the developer, they will be removed, and this type of photoresist is a *positive* photoresist. A *negative* photoresist is the opposite, where the exposed areas are hardened with respect to the developer. Both types are shown in Figure 3.2.

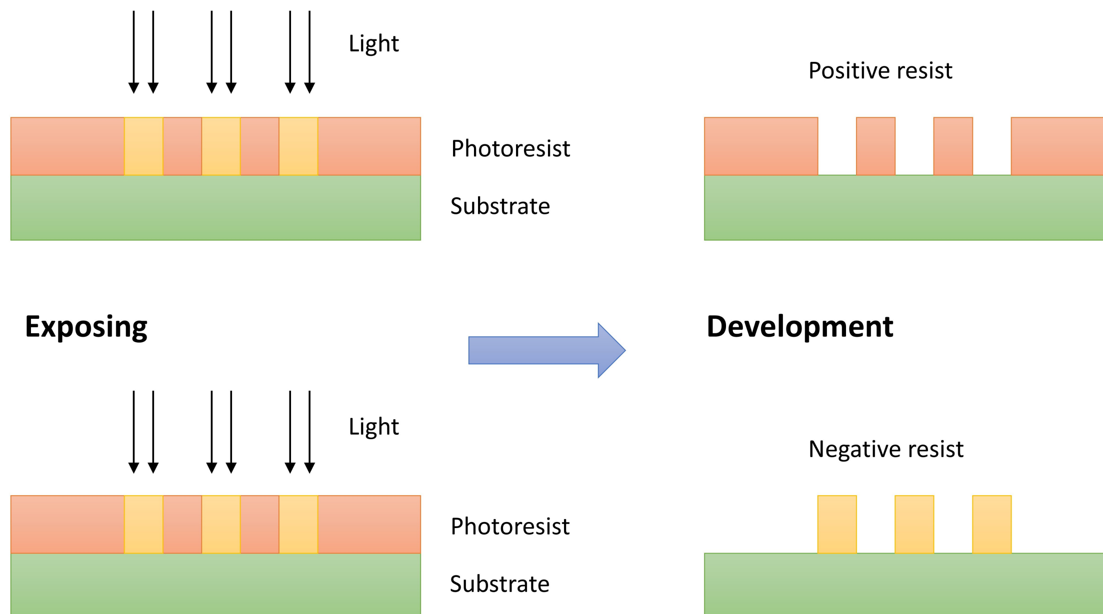

Figure 3.2: Illustration of how the different types of photoresist behave after being exposed to light and then to a developer.

There are many different types of photoresists available with different properties. In this thesis, a positive photoresist named MICROPOSIT S1813 from

Shipley is used because it is a well-known photoresist in the MiNaLab that can be used in dry etching, wet etching, and lift-off processes. The thickness varies with spin speed during coating but generally is between 1.0 μm and 2.0 μm, as shown in the datasheet from Shipley in Figure 3.3(b). S1813 is, as most photoresists, a system based on novolak resin with a diazonaphthoquinone sensitizer. The sensitizer makes the novolak base-insoluble as well as acting as the photoactive compound (PAC). After light exposure, the PAC is transformed into a base soluble product, and is no longer acting as a dissolution inhibitor. The spectral sensitivity of photoresists differs, and the absorbance spectrum is shown in Fig. 3.3(a).

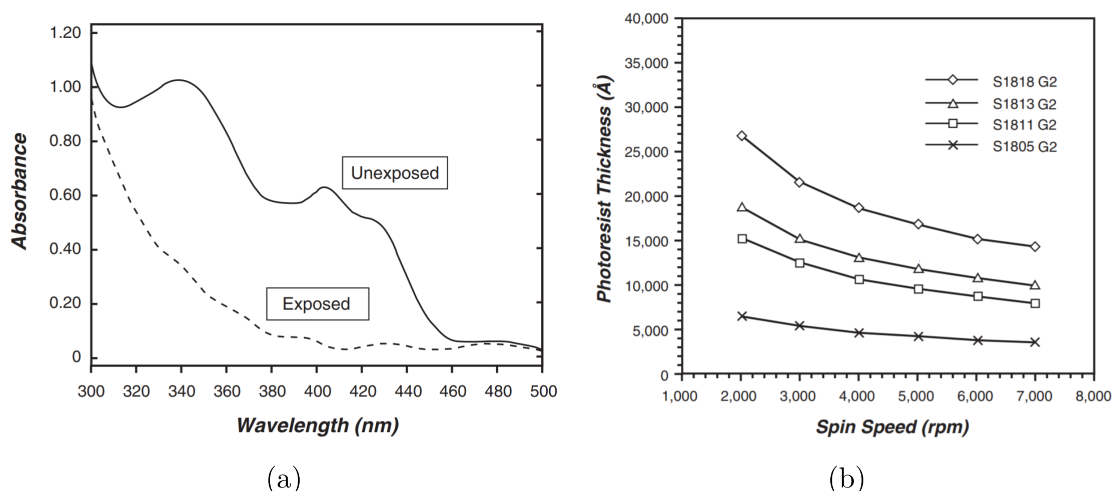

Figure 3.3: Panel (a) shows the absorbance spectrum for the S1813 photoresist, panel (b) shows the resist thickness vs spin speed for S1813. Both figures are taken from the product datasheet that follows the S1813 photoresist from Shipley [59].

For optimal patterning of the S1813 photoresist, we want the unexposed absorbance to be as high as possible simultaneously as the exposed absorbance is low. This is because we want the exposed regions to be transparent so that the resist is exposed all the way to the substrate, as well as having high contrast. If the contrast of the resist is low, there will be sloped sidewall profiles. Figure 3.3(a) indicates that S1813 behaves best at wavelengths around 430 nm.

Soft bake

A soft bake is done pre-exposure, typically on a hot plate, to remove the remaining solvents of the resist film. The softbake will improve the resist adhesion and avoid contamination of the resist.

Exposure

Exposing the resist to light is done in the aligner, in our case in a maskless aligner, as the system does not rely on shadow masks. The machine will dose short pulses of light at a specific wavelength in a design made in a computer software, in contrast to the more conventional illumination through a shadow mask. The exposure time can be changed in order to optimize the pattern. Shorter exposure times may give better resolution because there is less time for vibrations, but correspondingly will the developing time be longer.

The main limitation for photolithography is the *diffraction limit* and is a phenomenon that occurs when dimensions in the design are in the range of the wavelength of the light used. At this point, the wave nature of light has to be taken into account. If we consider the mask as an aperture, then according to the *Huygen-Fresnel* principle, each point in the aperture plane can be considered as a source of a plane spherical wave. The wave is considered a scalar wave, which is not consistent with electromagnetics, but the resulting model is practical and gives good results according to practice [32][52]. The diffraction limit is given by

$$I_{min} = 0.8\lambda/NA, \tag{3.1}$$

where λ is the wavelength of ligh used and NA is the numerical aperture of the lens [32].

Developing

After exposure of the photoresist, the wafer is placed in an alkaline solution, and depending on what type of resist is used, either the exposed or unexposed resist is removed. As mentioned above, the exposure time will decide how long exposure time is needed.

Hard bake

A post-develop bake is sometimes performed in order to harden the resist and making it more resistant to etching. In the case of the work done in this thesis, a harder photoresist will increase the etching selectivity of the photoresist with respect to the SiC.

Stripping

With the patterned photoresist, further processing such as deposition of oxides or metals or etching is usually carried out. After these steps, the remaining photoresist is removed. Usually, it is sufficient with acetone in an ultrasonic bath, but after dry etching, the photoresist can harden drastically, and a strong photoresist

stripper or a plasma etch with oxygen may be required to remove the hardened photoresist.

Lift-off

In order to form a metal pattern on the wafer, a method called lift-off is performed. This is done after photoresist patterning, and a metal layer is deposited on the wafer. Then the wafer is placed in an ultrasonic acetone bath, so the resist with metal on top is removed, and the metal in the exposed areas will remain on the wafer. The process is shown in Figure 3.4 below.

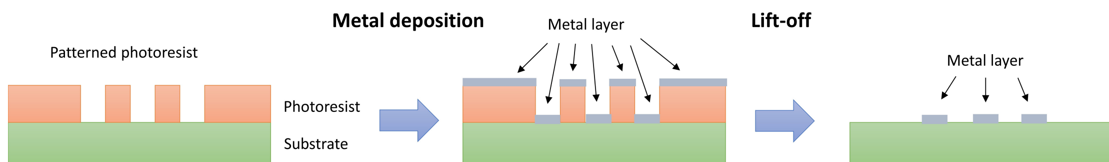

Figure 3.4: Demonstration of the lift-off process. The areas that we want to cover with metal are exposed to light subsequently developed. The metal layer will cover the whole wafer, but the parts that cover the photoresist will be removed if the photoresist is removed.

The aligner system used is the μPG 501 from Heidelberg instruments, a table-top maskless lithography system with a high-power LED light source with a wave-length of 390 nm. The resist spinner is the CEE 100 from Brewer Science, Inc.

3.1.4 Reactive ion etching

Reactive ion etching is a highly anisotropic and directional type of dry etch. In a dry etch, a plasma of reactive gases is bombarding the substrate. RIE is often used in semiconductor industry to achieve vertical structures with high aspect ratios (height/width). In the case of SiC, a dry etch has to be used because SiC is chemically resistant to almost all wet etches. In the RIE chamber, two electrodes create an electric field, and the ions in the plasma are accelerated towards the sample surface, where they react with the materials. Because of the high energy, they will break bonds in the sample materials and then create preferably volatile species, which are then ventilated out of the chamber. If the reactive ions create non-volatile species with the sample materials, they can deposit on the sample and work as micro masks, contaminating the sample. Different materials requires different etching chemistries, so the plasma gases used have to be modified for different etches [32]. A schematic presentation of the RIE chamber is shown in Figure 3.5.

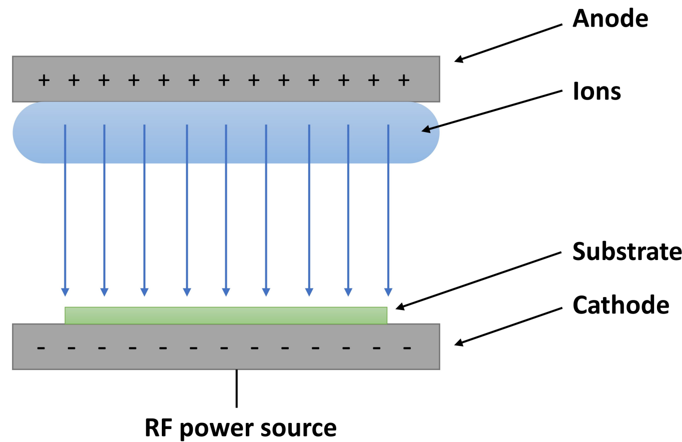

Figure 3.5: Schematic presentation of the RIE chamber. The electrodes will accelerate the ions and direct them towards the substrate. This is the main principle behind RIE, but there are many other important components of the chamber that are excluded here.

RIE of SiC with SiO_2 mask

Dry etching of SiC is normally achieved using a SiF_6/O_2 plasma chemistry in a 4:1 ratio [60][61][62]. The etch mechanism starts by breaking the Si-C bond by a physical mechanism and follows by a chemical mechanism that forms SiF_x $(1 < x < 4)$ volatile products. The C atoms react with O atoms to form CO and CO_2. The oxygen decreases the C-F bond concentration, but it can also form SiO_2 which can redeposit on the substrate and lead to micromasking [61].

SiC is a very hard material, so proper choice of mask material is crucial. The etching of organic-based photoresists such as the S1813 is typically much morerapid than the etching of SiC. Hence it will result in a lower than unity *selectivity* (etch rate[Si]/etch rate[PR]). Hard masks such as nickel, copper, and aluminium have been used extensively in other works [63][62][64][60], but because they are inert to fluorine chemistry (or form non-volatile metal species), they cannot be used as mask material in the 320 MK II in the MiNaLab as they will contaminate the chamber. SiO_2 is another hard mask material that can be used, and some studies have achieved a selectivity as high as 3.7 [65]. However, many other studies used an inductively coupled plasma reactive ion etch (ICP-RIE) setup, which is different from the ordinary RIE setup in the MiNaLab [32].

RIE of SiO_2 with PR mask

The process for etching SiO2 with a PR mask is already developed and used extensively in the MiNaLab. The etching gases used in this process are the fluorinated hydrocarbon CHF_3, CF_4, and O_2. F-radicals are generated in the plasma through electron impacts, and then they are accelerated to the substrate. Impact with SiO_2 forms volatile Si compounds. The addition of O_2 increases the etch rate of SiO_2 by creating even more F-radicals.

The RIE setup used in this thesis is the Advanced Vacuum Vision 320 MK II.

3.1.5 Physical vapor deposition

Physical vapor deposition (PVD) is a method for thin film deposition of different materials. PVD includes both sputtering and evaporation techniques. Evaporation of materials can be achieved by thermal heating or by heating the material with an electron beam. The result is Angstrom resolution of thin films [66]. The system used in the MiNaLab is an Angstrom e-beam evaporator.

3.2 Defect and device characterization

3.2.1 Scanning electron microscopy

In a scanning electron microscope (SEM), the sample surface is scanned with a focused electron beam and the emission from the interaction caused by these electrons, and in particular, the secondary electrons ejected from the sample surface, are analyzed. In the SEM, an electron gun, e.g., a LaB_6 or tungsten filament, is heated to produce monochromatic electrons. The electrons are condensed by the first condenser lens shown in Fig. 3.6, and the beam current is also limited by this lens. The aperture eliminates wide-angle electrons. The second condenser lens forms the thin (1 to 10 nm) and coherent e-beam. The scan coils move the beam in a raster fashion, much like an old cathode ray tube television. x- and y-directions of the beam are controlled by two wave-generators operating at different frequencies. The objective lens focuses the scanning beam on the sample. Image magnification M is given by $M = \frac{\textit{Scan distance in the image}}{\textit{Scan distance on the specimen}}$. Hence magnification is controlled by current applied to the x and y scanning coils [67].

The electrons can scatter both elastically (interaction with nuclei) and inelastically (by interaction with atomic electrons). Electrons that are elastically scattered through an angle of more than 90° are called backscattered electrons (BSE), while inelastic scattering can occur through many different interactions, but usually, the

beam transfers energy to the sample. Excited specimen electrons resulting from inelastic scattering are called secondary electrons (SE) if they possess energies less than 50 eV. The interaction volume is defined as the volume of the sample containing the scattered electrons [67]. The interaction volume decreases with atomic number Z and increases with incident electron energy E_0.

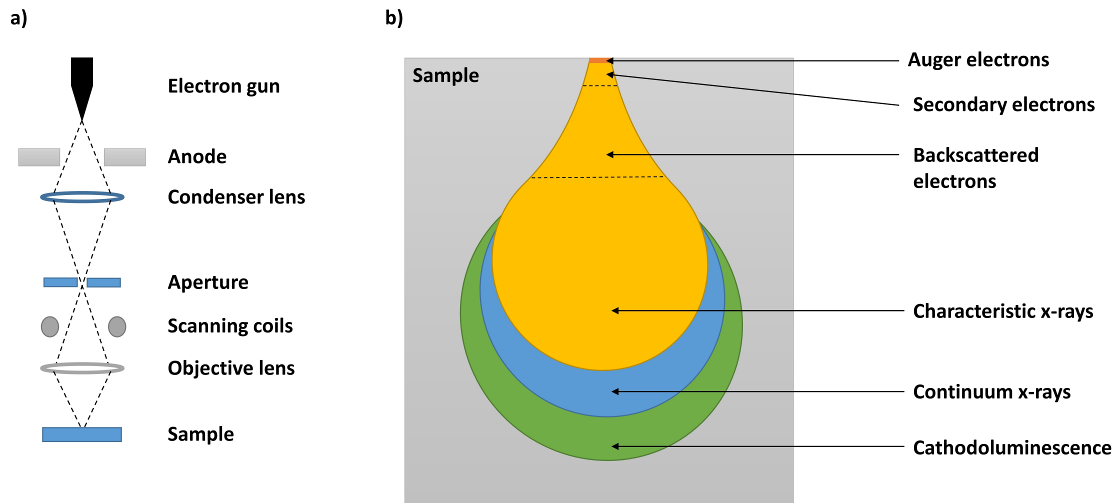

Figure 3.6: Panel (a) shows a schematic presentation of a scanning electron microscope (SEM). Panel (b) demonstrates the interaction volume and the different signals produced in the sample by the electron beam.

Secondary electrons move as charged particles and will scatter with other atomic electrons and lose their kinetic energy. The probability of inelastic scattering depends inversely on kinetic energy, so a SE only travels 1 to 2 nm in a solid. Most SE comes to an end inside the interaction volume, except the ones close to the surface. This means that the escape depth is defined as the region the SE must be within to escape the material. The resulting SE image, therefore, describes the surface topography. The surfaces that are not normal to the beam have a larger escape depth volume. Thus, the SE signal will be greater, and hence the slanted surfaces appear brighter. The SE detector is usually located on one side of the SEM chamber, so the sides tilted towards the detector will also appear brighter in the SE image. Most BSEs scattered to the vacuum retain most of their energy, and BSE and SE are easily distinguished by their different kinetic energies. Other signals from the SEM are characteristic X-rays, auger-electrons, cathodoluminescence, and transmitted electrons. High-angle scattering is proportional to Z^2. Therefore, a BSE image can show contrast due to change in chemical composition. BSE imaging gives information from 10 to 100 nm deep into the sample (approx. half the penetration depth), compared to only a couple of nm for

SE imaging. The SEM operator can control electron-acceleration voltage, distance between specimen and objective lens, called working distance (WD), probe current, and lastly the aperture of the objective lens to control spherical aberration. Spherical aberration is an optical problem which occurs because the lens fails to converge all the ray paths to the same focal point. For biological non-conducting sample, a thin metal layer such as gold is used to coat the sample and imaging of the surface topography will be achieved [67].

The SEM setup in the MiNaLab is the JEOL JSM-IT300 SEM. By utilizing a LaB_6 filament, up to 200.000× magnification with 4-10 nm resolution can be achieved. The system is equipped with secondary electrons (SE) and electron backscattering (BE) detectors for surface imaging, and a ThermoFisher UltraDry electron dispersive x-ray spectroscopy (EDS) detector is included for chemical analysis of samples. A Keythley 6485 PicoAmperimenter monitors the e-beam current from 10 pA to $\sim$1 μA. For measurements at low temperatures, the Gatan Model 1905 Temperature Controller for the Gatan c1002 cold stage operates at 80 K to 473 K with a liquid N_2 cooling system.

3.2.2 Cathodoluminescence spectroscopy

Cathodoluminescence spectroscopy (CL) is a technique mainly used to analyze the optical response of a material. Looking at the simplified band gap representation in Figure 2.4, if an electron in the conduction band and a hole in the valence band recombines, a photon with $hv = E_g$ is emitted. Semiconductors with *direct* band gaps have band edges with the same momentum, and recombination of EHP results in photon emission with energy close to the band gap energy. For semiconductors with *indirect* band gaps, recombination occurs through interaction with phonons, and recombination can occur at defects. EHPs can recombine at defects, either by interchanging charge carriers with band edges or by internal energy transitions. The emission of photons from energy transitions is called *luminescence*. If the charge carrier undergoing an energy transition with subsequent luminescence is excited by an incoming high energy electron, the effect is called *cathodoluminescence* and is the opposite of the *photoelectric effect* described by Albert Einstein [5]. These excited states can for, e.g., move in the lattice as *excitons*. Such an exciton has no net electric charge because it is a quasiparticle made of an electron and an empty electron site (hole). These excitons can recombine to their ground state spontaneously, which occurs close to the band gap, and may also occur at defects [4]. Photon emission may also occur due to charge-state transitions, or internal energy transitions in defects, described in Section 2.3.

The photon emission energies can be measured and may give useful information about the semiconductor properties such as the band gap, and the defects present

and their charge states. Because the emission from the band gap is usually very strong, a filter can be used to only gather the interesting parts of the spectrum. Since the SEM has an electron beam, a CL setup is often included in the SEM chamber.

Since the electron beam from the Lab_6 is in the order of keV, each electron has too much energy to create an EHP, and it is after a scattering cascade through the different type of signals mentioned in the SEM section above that the secondary electron has sufficient energy to create an EHP. Usually, one impinging electron results in 10^{10} secondary electrons. In order to maximize the CL yield, a parabolic mirror is used, as shown in Figure 3.7, and a piezoelectric engine is used to manually align the mirror so that the focus of the mirror is on the detector. The electron beam enters through a small hole in the top. The emitted photons are guided through a lens with a filter so certain wavelength regions can be excluded. This is necessary because the CL spectra are realized from a diffraction grating, and each hv can have multiple signals at higher diffraction orders according to Eq. 2.7. Cathodoluminescence is more efficient at low temperatures, so the sample stage is cooled down (preferably at 80 K (or below) with liquid N_2)[68][69].

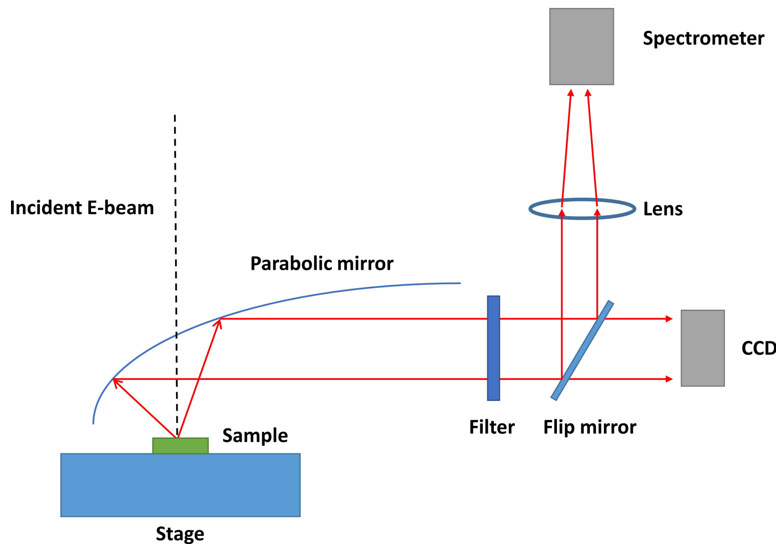

Figure 3.7: Schematic presentation of a CL setup in a SEM chamber. When the flip mirror is engaged, the light is guided towards the spectrometer for spectral analysis. For angle-resolved cathodoluminescence, the light is directed onto a CCD screen. A filter can be applied to block out certain wavelenghts.

3.2.3 Angle-resolved cathodoluminescence spectroscopy

Angle-resolved cathodoluminescence spectroscopy (ARCL) is a technique that can detect angle-dependent emission from a sample, giving more information about the photonic properties of the material than spectral CL. Similar to the CL setup described above, a parabolic mirror is used to collect the emission from the sample. Instead of focusing the signal to a diffraction grating, the signal is projected onto a charge-coupled device (CCD). Each pixel on the CCD image corresponds to a unique point on the paraboloid and similarly is each point on the paraboloid associated with a unique emission angle from the sample. The emission angle is described by a zenithal angle θ from 0° to 90°, and an azimuthal angle ϕ from 0° to 360°. The *solid angle* is a measure of the amount of angle an object covers from a viewpoint and is measured in *steradians* (sr), and since the 3D paraboloid is projected into a 2D CCD screen, the solid angle per pixel has to be corrected. The total hemisphere above the sample covers 2π steradians, but the mirror has an opening in the top for E-beam and an opening in one end to let the signal out, as well as a small opening between the mirror and the sample, so full coverage of the hemisphere is not possible. By rotating the sample, one can achieve a NA = 0.999 [69][68]. The emission angles are unique, so a 2D polar plot of the intensity of each direction can give useful information about the radiation properties of the material and how structuring the material also affects the radiation profile.

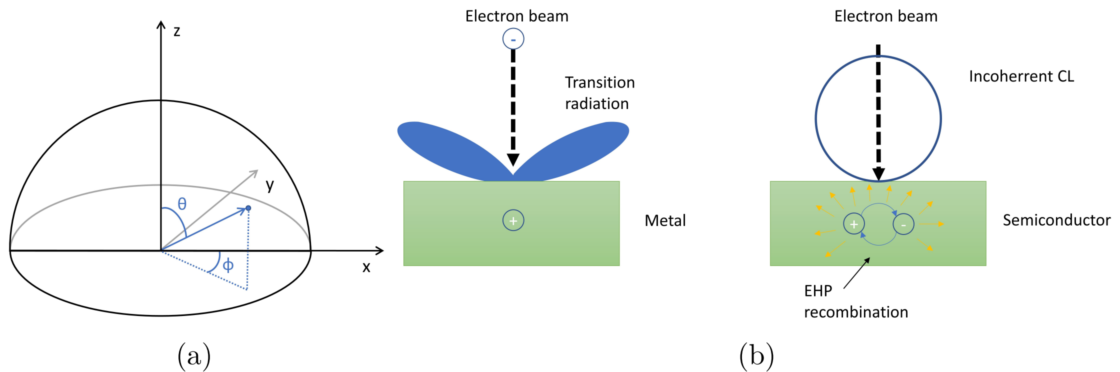

Figure 3.8: Panel (a) shows the unit hemisphere. Every point on the hemisphere can be described with a unique combination of the ϕ and θ angles. Panel (b) is a schematic presentation of how the radiation profile of dipole transition radiation in a metal and the incoherent CL looks like from a profile view.

Radiation from a sample in CL can be separated in *coherent* and *incoherent* radiation. Coherent radiation has a fixed phase-relation with the E-field of the incoming electrons and is composed of transition radiation at the surface, plasmon generation, and Cherenkov radiation. Coherent radiation is the dominant process

in metals, but for most other materials, the effect is weak. Luminescence from EHP recombination in semiconductors is considerably stronger and is a form of incoherent radiation because it happens spontaneously after the cascade event from an incomming electron described in the SEM section above. Transition radiation will have a toroidal radiation profile because the negatively charged incident electron will induce a positive charge on the metal surface that creates a varying dipole moment. In contrast is the incoherent radiation profile *Lambertian*, which means that the emitted radiance ($\mathrm{W \cdot sr^{-1} \cdot m^{-2}}$) is independent of observation direction [70][52]. This is due to Snell's law

$$n_1 \cos\theta_1 = n_2 \cos\theta_2, \tag{3.2}$$

where n_1 and n_2 are the refractive indices of the two materials at the interface, and θ_1 and θ_2 are angles of the light beam at each side of the interface. This means that the radiation profile is cosine dependent on the zenithal angle θ because light at larger angles is refracted at the surface of the emitter. The radiance is constant because the reduction in solid angle is proportional to the cosine dependent emitted power. The radiation profile of TR and incoherent radiation is shown in Figure 3.8(b) [52][70].

In some materials like Si, the emission can be composed of both incoherent and coherent radiation, and the contributions of both of them to the total emission is both dependent on the wavelength of the emitted electrons and the energy of the incident electrons. Brenny and Coenen [70] found that for certain wavelengths (λ=400 nm), the radiation from Si was mostly due to surface effects such as TR instead of typical semiconductor properties such as recombination centers or band gap. Since the probe is in the nano size (the e-beam), nanostructures will also affect the radiation profile. For a planar surface with incoherent radiation, the profile will be Lambertian, but a hemispherical surface will have a hemispherical angular radiation distribution. Thus a spectrum analysis of the material combined with AR-CL can be a useful technique to both strengthen the understanding of the CL spectrum and to examine how nanostructures influence the radiation profile [70][69][68].

The CL setup used was the Delmic SPARC Cathodoluminescence System. The setup utilizes a Andor Shamrock SR-193i spectrograph with two motorized double grating turrets (Grating turret 1: Mirror and 300 g/mm grating blazed at 500 nm, and Grating Turret 2: 300 g/mm grating blazed at 1200 and 600 g/mm grating blazed at 300 nm). For spectral filtration, band pass filters at 400, 550, 700 and 1000 nm are available. A UV detector Andor Newton 940 CCD camera with 2048×512 array of back-illuminated (BU2) sensors covers from 250 to 1100 nm wavelengths, and IR detector Andor iDus InGaAs 1.7 with one array of 1024

sensors covers from 600 to 1700 nm wavelengths.

3.2.4 Stylus profilometer

A stylus profilometer is a tool for measuring surface profiles to analyze their roughness. It works by approaching the sample with a small tip and with the use of a feedback loop, it is in constant contact with the surface. When moving around the sample, the system will detect changes in the topography and move the tip in the Z-direction to keep the force on the tip constant. This results in a high Z-direction resolution, but because the tip is in contact with the sample, there is also a chance of substrate damage. In this thesis, the profilometer is used to measure the height of the structures by measuring a dummy structure with the same height as the structures [71]. The system used in the MiNaLab is a Dektak 8 profilometer.

Chapter 4

Process development

This chapter is devoted to the fabrication and optimization of a process for the structuring of 4H-SiC. By using the methods outlined in the *Processing* section, pillar structures in SiC have been developed. The process involves many different steps, and each step has been optimized to improve the end result. The available photolithography process in the MiNaLab has been developed for different devices in Si, so the development of such a process for SiC was important for the research group and was one of the goals of this thesis. First, a schematic presentation of the process flow will be shown, and later each step and how it was optimized will be explained. This chapter will also discuss the parameters chosen for each step and the results after altering the parameters.

4.1 Process flow

In Figure 4.1 the process flow developed in this thesis is shown. The substrate used is a (0001) 4H-SiC wafer from Cree, Inc. with a 10 μm epitaxial layer grown 4°off the c-axis with a net doping concentration of $N_D \sim 1 \times 10^{15}$ cm^{-3} [72]. The wafer was cut in 5x5 mm^2 or 11x11 mm^2 samples by a laser cutter.

A $\sim$1 μm layer of SiO_2 was grown in the PECVD chamber with a $SiH_4/N_2/N_2O$ gas chemistry at 30 W RF power and a process pressure of 800 mTorr. The wafer was then covered in a positive photoresist, and the photoresist was patterned in a photolithography step with the design shown in Fig. 4.2 from the LayoutEditor software. Next, a RIE step transferred the pattern from the photoresist to the SiO_2 layer. The patterned SiO_2 layer functioned as a hard mask for a last RIE step which finalized the process by transferring the pattern onto the SiC wafer.

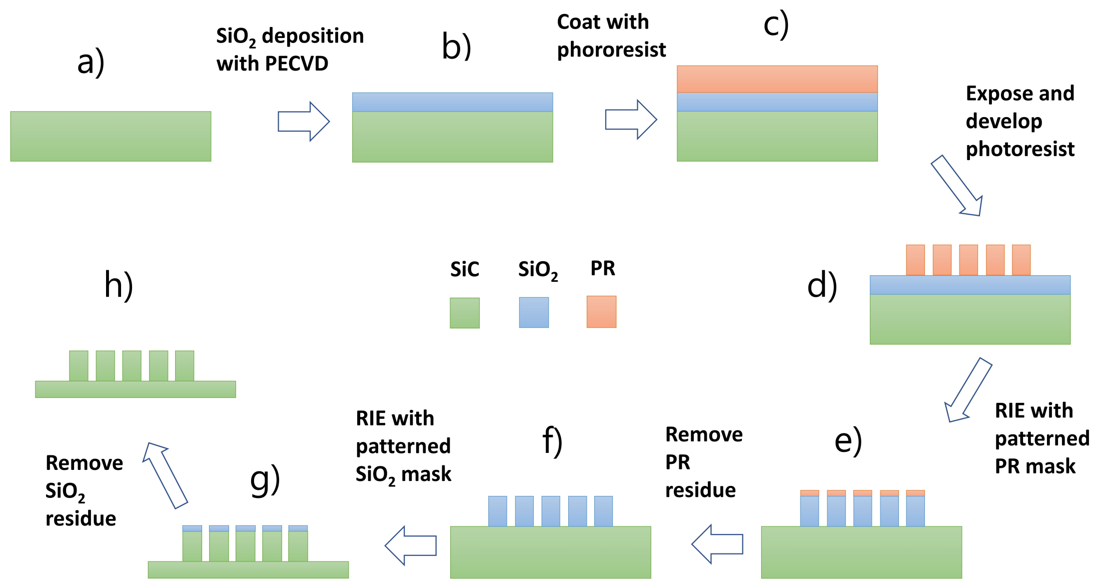

Figure 4.1: Schematic presentation of the fabrication process used in the MiNaLab for structuring of SiC.

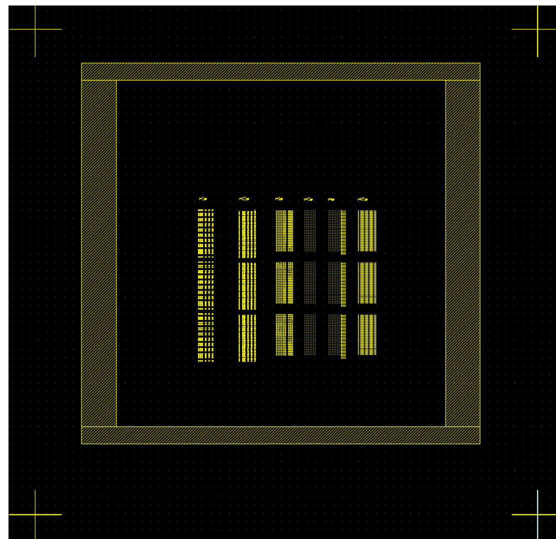

Figure 4.2: Screenshot from LayoutEditor software, showing the lithography design that was exposed to the photoresist. The post stamps in the corners of the design were used for alignment of later photolithography processes.

4.2 Using standard Si-based lithography process

The first attempt at making structures was made following the process flow in Figure 4.1, but none of the steps had been optimized for SiC yet. The photolithography recipe used to make these structures was developed for a different design and for Si rather than SiC. Importantly, the RIE steps used were not optimized for this particular design, and the SiC RIE step was based on other studies and not altered for the RIE system used in the MiNaLab. The results from this first trial are shown in Figure 4.3.

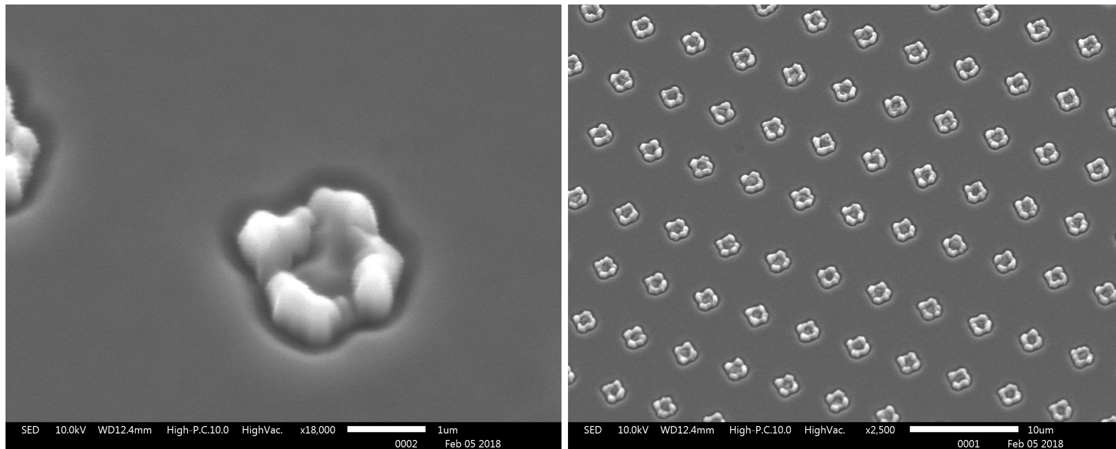

(a) (b)

Figure 4.3: (a) Close up image of SiC structure made by using a Si lithography recipe and standardized etching recipes for both the SiO_2 and SiC etch steps, (b) overview image of the same structures.

Fig. 4.3 shows that the middle of the structure is etched away, and the side walls are rough and slanted. The dimensions of the design were also too small (r=1 μm), approaching the diffraction limit of the photolithography system used. Fig. 4.3 reveal that the Si-based recipe yields unsatisfactory structures. It is difficult to know exactly which step was the culprit of the poor results, but since the RIE of SiO_2 and PR was a known process in MiNaLab, the other two steps were examined and optimized first.

4.3 Optimizing the lithography process for 4H-SiC

As mentioned in Section 3.1.3, there are many variables that may be modified to achieve the optimal photoresist mask. For any given PR thickness and thus spin speed, a unique combination of exposure time and developing time has to be chosen. Since the lithography step is the first step where the design is introduced, any error in this step will carry over to the next steps and also to the final result. Therefore the starting point of an optimization of the fabrication process is at the lithography step.

The starting point of the optimization of the lithography step was to choose a series of parameters and then examine the photoresist mask in an optical microscope to check if the desired result was achieved. It is a time-consuming and iterative process, and requires many trial and error experiments. This step involves numerous attempts. Thus only how the parameters were changed and the outcome will be described and discussed here. The optimal end result was a photoresist mask with sharp edges and vertical sidewalls in the design.

A PR mask was made using the PR S1813 with the process parameters shown in Table 4.1. Firstly, the wafer was cleaned in an ultrasonic acetone bath for 10 minutes, and then dried with a N_2 gas gun. A cleanse in acetone was sufficient for the trial and error experiment performed here and saved time, as the RCA process is more time-consuming. Later, a more thorough cleanse using the RCA cleaning process was used for optimal lithography results. After the cleanse, the wafer was coated with HMDS primer at the same spin speed and duration as was used for the PR. The PR was soft-baked at 110°C for 1 minute between the coating of the wafer and exposing.

Table 4.1: Process parameters in the first lithography optimization attempt

Spin speed [rpm]	Spin duration [s]	Thickness [μm]	Exposure time [ms]	Developing time [s]
5000	60	$\sim$1.3	50	90

Observation in an optical microscope of the PR mask showed that the mask had rough and slanted edges, which could be due to overexposing and over development. Several more trials were performed with varying developing times, but the mask still displayed rough edges and slanted edges. The features in the design were not close to the diffraction limit. The long exposure time was hypothesized as being the culprit of the distorted structures. Since small vibrations are unavoid-

able, having long exposure times will increase the exposure in regions that should not be exposed.

The exposure was varied from 10 ms to 35 ms in 5 ms increments in order to find the optimal exposure time. The spin speed was set to 6000 rpm for 1 minute (thickness $\simeq 1.2\ \mu$m) because the diffraction effect is smaller when the light source is closer to the PR. The developing time was initially set at 60 seconds and then to be optimized later. The developing time was also changed for each particular exposure time if it was observed that the design was not fully developed. This experiment found that the best exposure time was 20 ms for that particular spin speed. It was observed in the optical microscope that the edges of the structures were more defined for shorter exposure times. However, short exposure times resulted in too long developing times, and the developer would start to erode the unexposed PR as well. At 20 ms the pattern had sharply defined edges at developing times just over 1 minute. At larger time intervals, over-exposure occurs. The optimal developing time was then found to be 80 seconds by using the previously mentioned parameters with varying developing times. The optimal lithography parameters are summarized in Table 4.2.

Table 4.2: Optimal process parameters for the lithography step

Spin speed [rpm]	Spin duration [s]	Thickness [μm]	Exposure time [ms]	Developing time [s]
6000	60	$\sim$1.1	20	80

This resulted in a PR mask with defined and sharp edges. The smallest structures had dimensions approaching the diffraction limit of the light source, and thus not possible to realize.

Another challenge with the process was that parts of the PR would loosen from the substrate during development. This was because of poor adhesion of the PR to the substrate, even with HMDS primer. As mentioned in 3.1.3, a dehydration bake after cleaning will remove water from the surface and improve primer adhesion, and thus also PR adhesion. First, a dehydration bake of the wafer at 110°C for 30 minutes was tested, which improved the adhesion. It was later found that a dehydration bake for 10 minutes was as effective as 30 minutes at evaporating water from the surface, and most parts of the PR mask adhered to the substrate during development.

To further improve the adhesion of the PR, a switch from cleaning with ace-

tone to the standard RCA cleaning procedure was carried out. The RCA cleaning procedure is a more rigorous method than cleaning with acetone, especially with regard to organic contamination. These two inclusions to the lithography step drastically increased the adhesion of the PR as well as improved the sharpness of the edges in the mask pattern. The HMDS primer's viscosity is lower than that of the PR, so the spin duration was reduced to 30 seconds to give the same thickness and uniformity as 60 seconds, and a 10 second waiting time before coating with PR was added to let the primer bind more strongly to the surface.

After having some trouble with the alignment of the wafers in the Heidelberg maskless aligner, a switch from 5x5 mm^2 to 11x11 mm^2 wafers both resolved this problem as well as improved the PR mask. This is because the smaller wafers will vibrate more than the larger wafers when the stage is moved around due to the vacuum effect from the pump being stronger for larger wafers.

Lithography recipe for structuring of 4H-SiC

From the experiments, a recipe for a high quality photoresist mask has been established, and is outlined below.

1. Clean the wafer following the standard RCA cleaning procedure.
2. Dehydration bake on a hot plate at 110°C for 10 minutes. Let the wafer cool before proceding to the next step.
3. Apply HMDS primer and let it sit for 10 seconds.
4. Spin the wafer at 6000 rpm for 30 seconds.
5. Let the primer set for 60 seconds.
6. Apply S1813 photoresist and spin the wafer at 6000 rpm for 60 seconds.
7. Softbake at hotplate at 110°C for 60 seconds.
8. Expose the wafer at an exposure time of 20 ms.
9. Develop in MF-321 developer for 80 seconds. Swirl the wafer gently a couple times during development.
10. Rinse the wafer in clean de-ionized water for at least 30 seconds, and then blow dry with N_2 gun until the wafer is completely dry.

4.4 Optimization of reactive ion etch processes

As will be shown later, the PR/SiC etch selectivity is low and will correspondingly limit the size and shape of structures achieved by directly etching with a PR mask. The optimized fabrication process involves two RIE steps with higher selectivity,

each with different mask materials and gas chemistries, to overcome this problem. The two steps are different. Thus, the optimization processes are also different. The standardized RIE recipe used for etching SiC in the MiNaLab has not been optimized for a SiO_2/SiC etch, and a selectivity test to find the best parameters was needed. An optional route of using the PR mask directly on SiC for faster fabrication is also possible but has its limitations.

4.4.1 Optimization of RIE for PR mask and SiO_2

The first RIE step is the etching of SiO_2 with a PR mask, where the goal is to transfer the pattern made by lithography to the SiO_2 layer. As mentioned earlier, the dry etching process uses a CHF_3 /CF_4/O_2 gas chemistry. The etching process is well-known in the MiNaLab, and the selectivity is already known to be 3.7. In order to achieve more vertical sidewalls, the process pressure was decreased from 50 mTorr to 5 mTorr. The change in pressure resulted in a change in etch ratios. This new etch ratio was not measured, as the results from the etch were satisfactory for further characterization. Figure 4.4 shows how a selectivity test is performed.

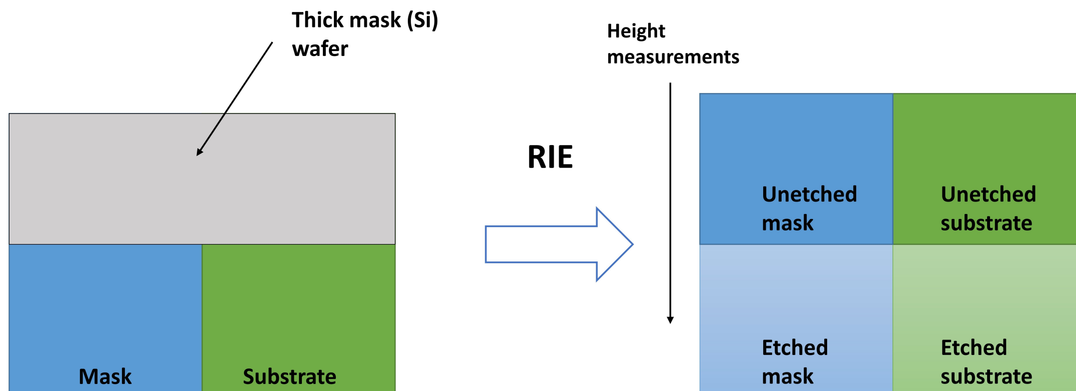

Figure 4.4: Schematics of how a selectivity test is performed. A thick mask covers half of the wafer so that the two different materials are both etched and unetched. The height from unetched to etched is measured with a profilometer with high lateral resolution.

Table 4.3: Process parameters used in the RIE attempts of SiO_2 and PR

Experiment	RF power [W]	Process pressure [mTorr]	CHF_3 gas flow [sccm]	CF_4 gas flow [sccm]	O_2 gas flow [sccm]
1	400	50	24	6	5
2	400	5	24	6	5

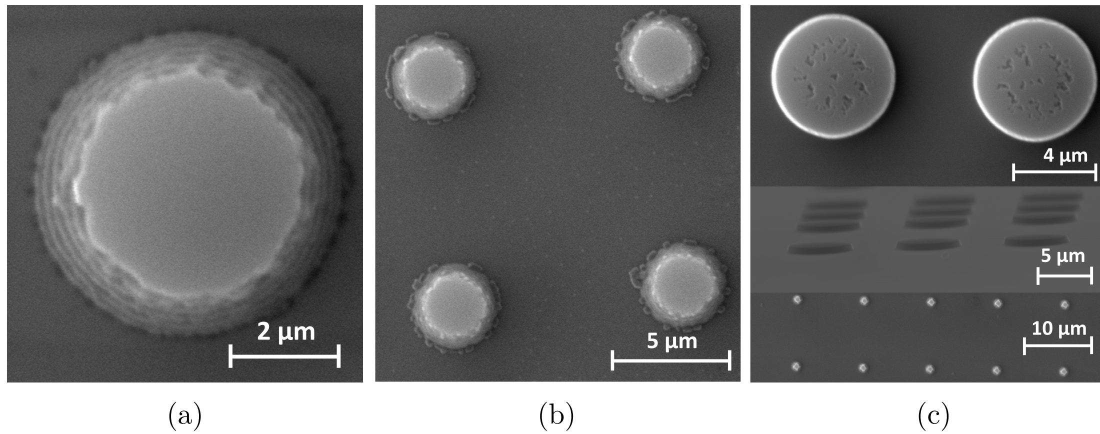

(a) (b) (c)

Figure 4.5: (a) SiO_2 structures from experiment 1 with r=3 μm, (b) and with r=2 μm. In (c), top part of image show SiO_2 structures from experiment 2 with r=3 μm, middle part of image shows tilted view of the same structures and the bottom part shows r=1 μm structures. All images are taken in the SEM at a acceleration voltage of 30 kV.

The standard settings in the RIE recipe for SiO_2/PR resulted in rough and slanted sidewalls on the structures, as shown in Figure 4.5(a). As seen in Fig. 4.5(b), the mask has a slanted sidewall profile with steps, similar to a pyramid. By lowering the process pressure from 50 mTorr to 5 mTorr, more vertical and sharp sidewalls were achieved, as seen in Fig. 4.5(c). The largest structures are circular and have almost vertical sidewalls. The smallest structures (r=1 μm) are not circular and have rough and slanted edges, but this is due to having dimensions approaching the diffraction limit of the photolithography system. The sidewalls are not completely vertical, but for the goal of this thesis, the structures were satisfactory. Often a lowering of process pressure leads to a more directional etch and therefore also steeper sidewalls because the plasma is less dense and there are fewer ion collisions. Thus, the etch rate will also decrease. It is evident from Fig. 4.5(c) that the sidewall profiles are improved.

The residue on top of the structures in Fig. 4.5(c) is highly cross-linked photoresist, which was not possible to remove with ordinary stripping agents. The residue may occur in certain photoresists when they are etched for too long because the plasma bombardment will increase the temperature in the photoresist, and with the addition of deep UV radiation from the plasma, this induces a chemical change in the material [73]. The organic polymer is resistant to most removants. After a typical etch in the CHF_3/O_2 gas chemistry, the photoresist is easily removed with acetone in an ultrasonic bath, and if not, Piranha solution at 150°C was used to remove the remaining residues. However, both these two acids have little to no effect on the resilient photoresist. Another approach is to combust the residue in a O_2 plasma for a few minutes. All of these approaches were attempted but with no effect. Stronger removants such as the TechniStrip Micro NGA II or TechniStrip MLO 07 can be used, but these were not available in the MiNaLab. A different option is to use dimethyl sulfoxide (DMSO) heated to 60-80 °C, but this has not been tested yet [74], because the residue on the structures was removed during the second RIE step.

4.4.2 Optimization of RIE for SiO_2 mask and 4H-SiC

The second RIE step transfers the pattern to the SiC wafer and finalizes the device fabrication. As mentioned in the *Processing* section, SiC etching with SiO_2 is typically performed with fluorine chemistry. This process had to be developed since no prior recipe had been developed, and a more elaborate selectivity test had to be performed. Different gas chemistries will give different etch rates and structure profiles. RF power and pressure also influences the etch result, but other studies show that the gas ratio is the most important parameter in the etching of 4H-SiC [60][61][62]. Table 4.4 shows the different gas chemistries used, and their corresponding etch rates. The RF setpoint was set to 200 W and a process pressure of 10 mTorr for all the experiments. The etch rates were calculated by finding the vertical difference between the unetched and etched parts with a profilometer, similar to the selectivity test setup shown in Figure 4.4.

Table 4.4: Results from selectivity test in the RIE with SF_6/O_2 gas chemistry in varying ratios.

SF_6 [sccm]	O_2 [sccm]	SiC etch rate [nm/min]	SiO_2 [nm/min]	Selectivity [arb. units]
2.5	22.5	20.5	20.9	0.98
7.5	17.5	43.1	28.3	1.52
12.5	12.5	42.7	21.2	2.01
17.5	7.5	46.7	27.6	1.69
22.5	2.5	52.5	35.5	1.48
30	10	53.9	29.2	1.85
30	15	51.3	27.7	1.85
40	10	57.2	34.4	1.66

The selectivity of the 1:1, 3:1 and 2:1 gas ratios were the highest. By increasing the SF_6 gas flow the SiC etch rate increases. Similarly, the SiO_2 etch rate increases, but with the addition of O_2 gas the etch rate of SiO_2 is altered. As mentioned in 3.1.4, this is expected because volatile SiF_x species are created, and the O_2 has the role of binding to the C atoms. Without a proper study on the species present at the different gas flow ratios it is hard to tell which volatile products that are formed. As the 3:1 gas flow ratio is close to the most widely reported in literature (4:1), the 3:1 and 1:1 ratios were used to make structures. 1:1 were chosen because it had a higher selectivity than the 2:1 ratio. The structures made with the two ratios were then imaged in the SEM and then compared. The parameters used in the etch was identical except from the gas flow ratios, and they are given in Table 4.5.

Table 4.5: Process parameters used in the RIE attempts of SiC and SiO_2.

Gas flow ratio	RF power [W]	Process pressure [mTorr]	SF_6 gas flow [sccm]	O_2 gas flow [sccm]	Etch duration [min]
1:1	200	5	12.5	12.5	22
3:1	200	5	30	10	32

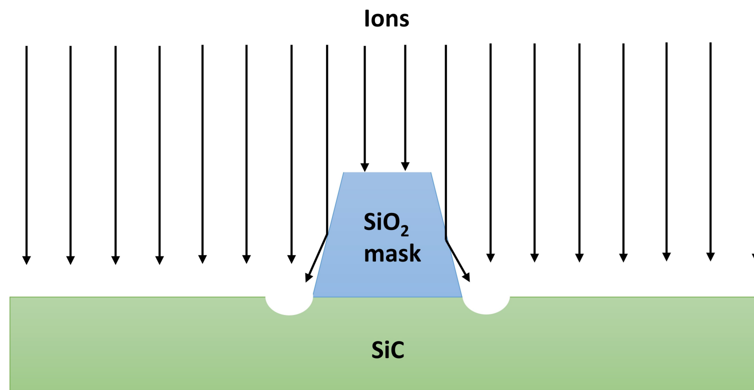

Figure 4.6: Schematic explaining how the trenching effect occurs. The sidewalls are tilted, so the path of the accelerated ions are deviated from the straight path, and the area close to the structures are more strongly etched because there will be more incident ions in this area.

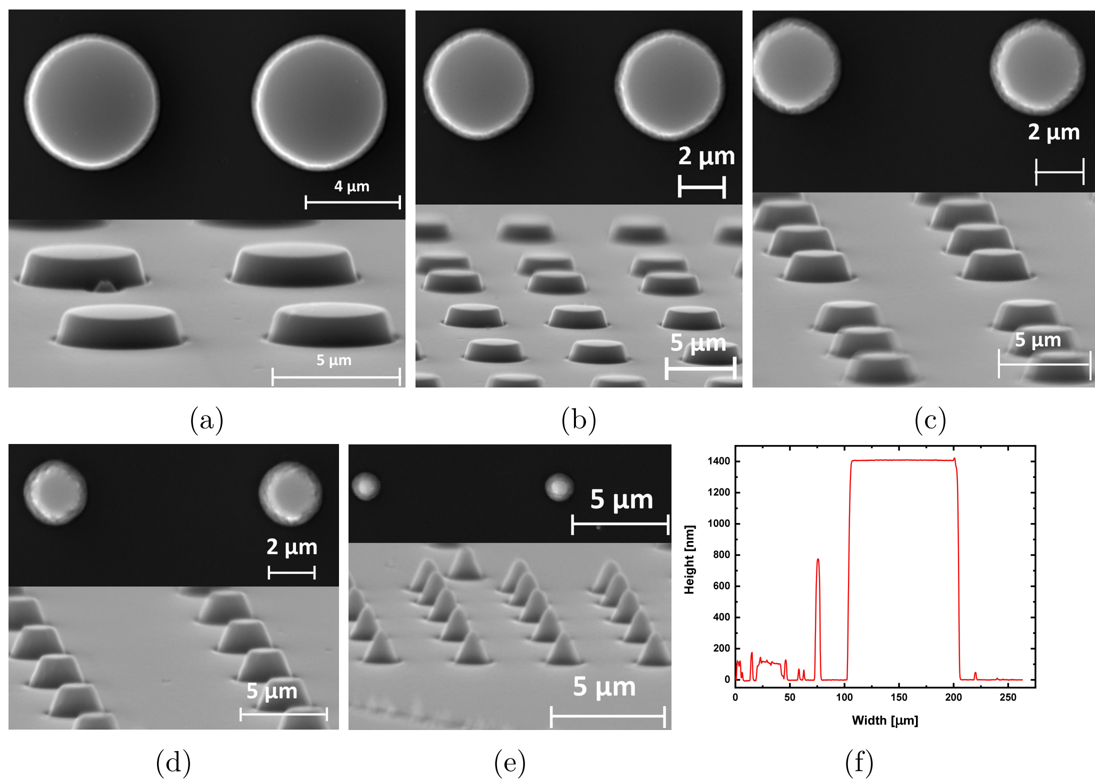

Figure 4.7: (a) The top part of the image are micropillars with r=3 μm seen from above, the lower part is tilted view of the same structues, (b) same as first image, but for structures with r=2.5 μm, (c) r=2 μm, (d) r=1.5 μm, (e) r=1 μm. The structures are made with the 1:1 gas flow ratio. All the images are taken in the SEM with an acceleration voltage of 30 kV. (f) shows the height measurement made with the Dektak profilometer.

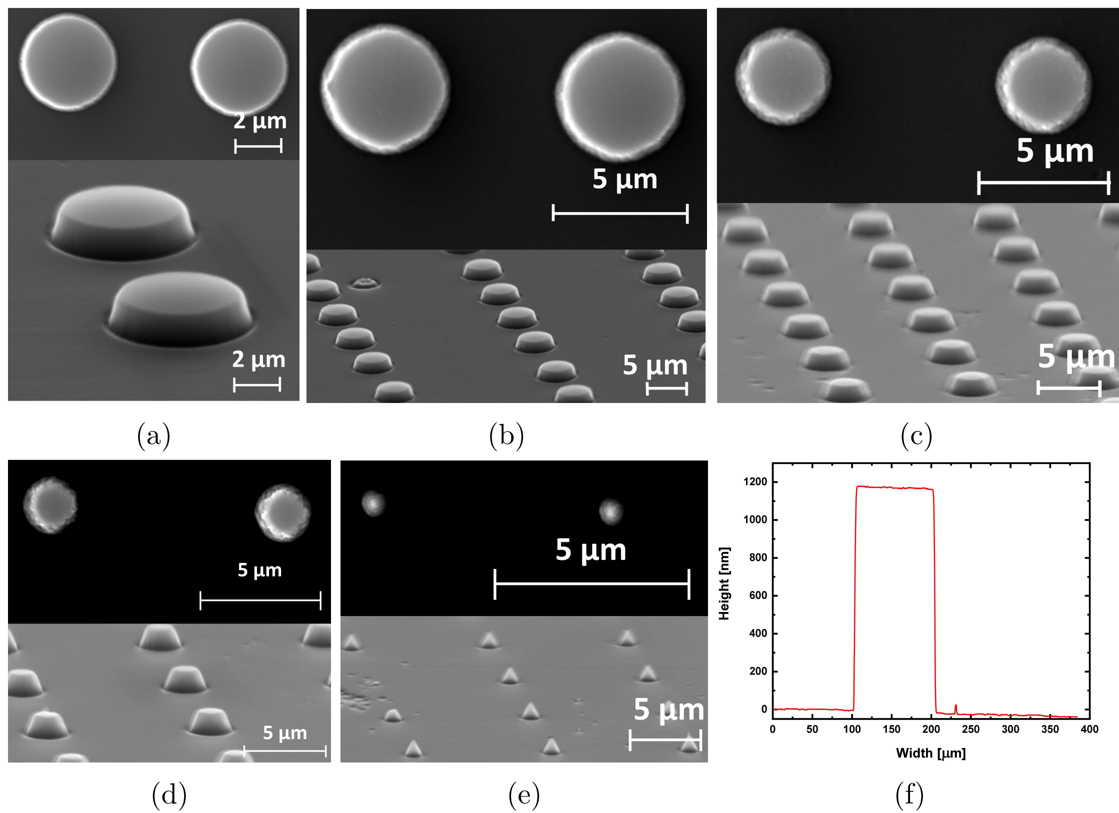

(a) (b) (c)

(d) (e) (f)

Figure 4.8: (a) The top part of the images are micropillars with r=3 μm seen from above, the lower part is tilted view of the same structues, (b) same as first image, but for structures with r=2.5 μm, (c) r=2 μm, (d) r=1.5 μm, (e) r=1 μm. The structures are made with the 3:1 gas flow ratio. All the images are taken in the SEM with an acceleration voltage of 30 kV. (f) shows the height measurement made with the Dektak profilometer.

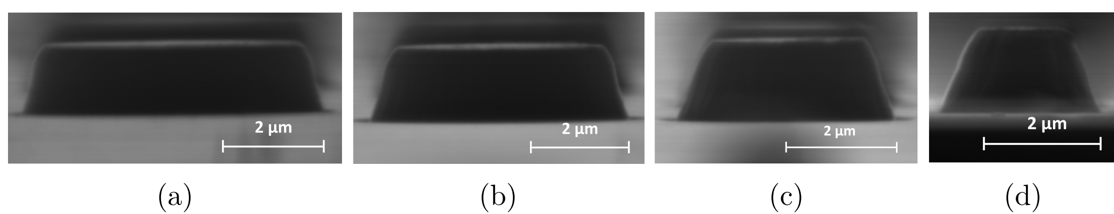

(a) (b) (c) (d)

Figure 4.9: (a) Profile view of micropillars with r=3 μm, (b) r=2.5 μm, (c) r=2 μm and (d) r=1.5 μm. The structures are made with the 3:1 gas flow ratio. All the images are taken in the SEM with an acceleration voltage of 30 kV.

The structures made with the two different gas flow ratios are very similar, both with respect to sidewall profile and edge roughness. Both have the same trend with

decreasing size and a stronger diffraction effect from the photolithography step. Because the selectivity is different for the gas flow ratios, the height is different. Given that the 3:1 ratio has $\simeq$10 nm/min higher SiC etch rate than the 1:1 ratio it is a faster process for making structures. Therefore, for etching as tall structures as possible, the 1:1 ratio is preferred, as the PR mask thickness is limited, and hence the SiO_2 mask will consequently also be limited. A higher selectivity means that less of the sacrificial mask is etched with respect to the target material. The structure morphology is seemingly independent of the gas flow ratio so that each process will be beneficial depending on the objective. None of the etches show sign of micromasking, which is a common effect in the RIE of SiC with SiO_2 masks. However, both the processes have a trenching effect occurring around the structures. The source of the trenching effect is explained in Fig. 4.6. The slanted sidewalls can occur due to redeposition of inert species in the etch chemistry, but by comparing the SiO_2 mask in Fig. 4.5(c) with the SiC structures in Fig. 4.7(a) and 4.8(a), we see that the sidewall profile is similar, so the slanted sidewalls are most likely a product of either the SiO_2/PR etch process or from the photolithography process.

4.4.3 RIE of PR and 4H-SiC

The process outlined so far involves a SiO_2 deposition step and two RIE steps. Thus, the device fabrication is time-consuming. In an attempt to substantially reduce the processing time, a PR mask directly on SiC was attempted. The selectivity was measured to be 0.42 at the highest, which means that the structures made by this process would have a maximum height of PR thickness $\times$ PR/SiC selectivity. Because the height is limited by the resist thickness, the thickness of the PR masks were varied in order to find the optimal PR mask for this shorter process. For a coating with PR mask using a spin speed of 6000 rpm (thickness $\sim$ 1.1 μm), the resulting height of the structures is $\sim$500 nm. Several structures were made using this process, all with different heights and morphology. The parameters used in the RIE process were the same as for the 3:1 gas flow ratio shown in Table 4.6 and used for all the different PR masks. The parameters changed in the photolithography step were spin speed, exposure time, and developing time. For some of the PR masks, the thickness was the same, while the etch time was changed. This experiment was performed simultaneously as the photolithography experiment, so when a PR mask with a given thickness had defined features, that recipe was used as a PR mask for SiC etch. A hardbake at 120°C for 3 minutes after developing the PR masks were tried for all the processes in order to improve the dry etch resistance of the PR mask, and thus increase the selectivity. The PR masks that were hardbaked showed signs of more slanted sidewalls by observing in an optical microscope, and therefore a hardbake was discarded from the process.

Table 4.6: Photolithography processes for the different PR masks.

Process	Spin speed [rpm]	Thickness [μm]	Exposure time [ms]	Developing time [s]	Etch time [min]	Structure height [nm]
A	4500	$\sim$ 1.3	30	55	36	$\sim$825
B	3500	$\sim$ 1.5	30	70	30	
C	5000	$\sim$ 1.2	20	90	20	$\sim$450
D	6000	$\sim$ 1.1	20	80	14	$\sim$425

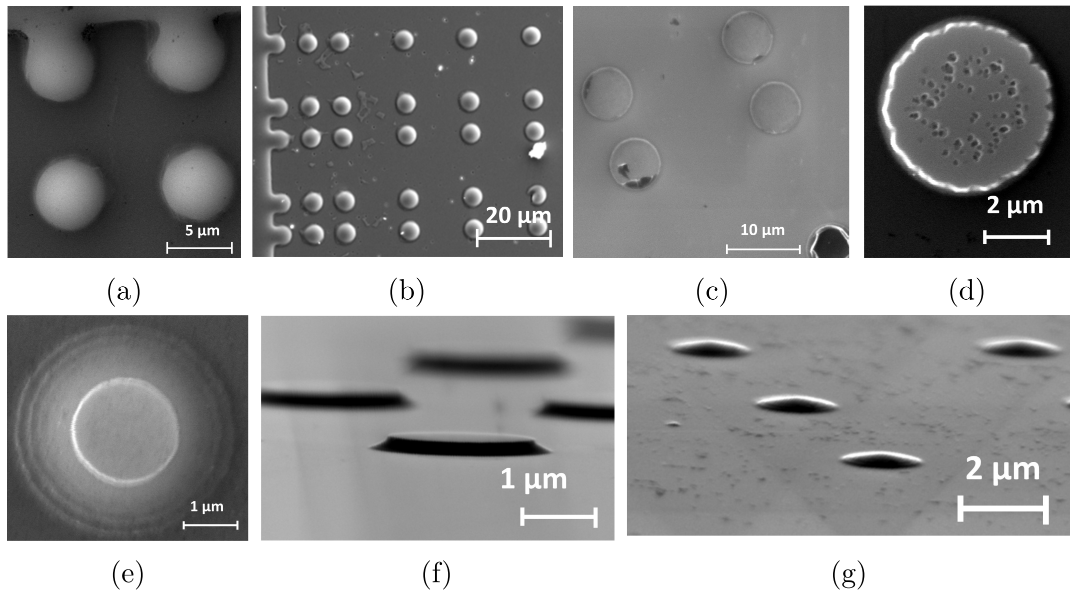

(a) (b) (c) (d)

(e) (f) (g)

Figure 4.10: Image of structures made with process: (a) A, (b) B, (c) C, (d)-(g) D. Process parameters are shown in Table 4.6. All the images are taken in the SEM with an acceleration voltage of 10 kV for (b) and (c), and 30 kV for the other images.

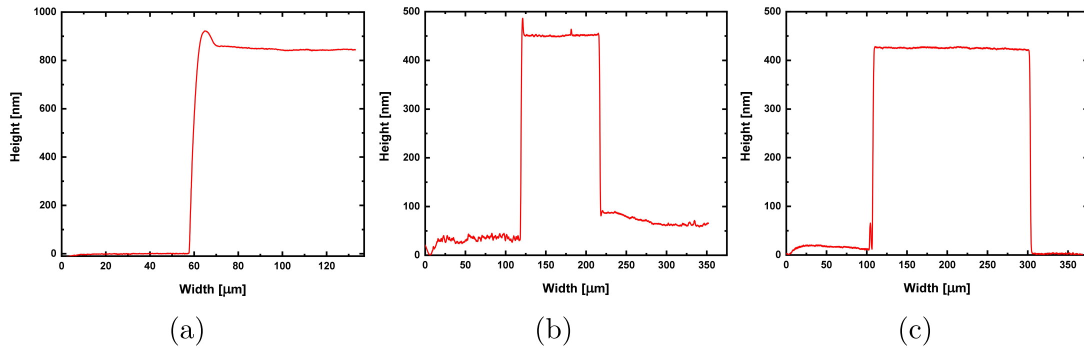

(a) (b) (c)

Figure 4.11: Height measurements of the structures fabricated by process: (a) A, (b) C, (c) D. Process parameters are shown in Table 4.6. The measurements were performed with the Dektak32 profilometer.

Different PR masks were explored with the same etch chemistry, where only the etch time was varied. The structures in Fig. 4.10(a) have structural similarities to SILs with a dome-like appearance. They also have a lot of PR residue on the sample surface that was not removable, so the long etch created cross-linked PR that redeposited on the surface. Fig. 4.11(a) shows that the height of the structures is ∼825 nm. For process B, the PR thickness and etch time were decreased, seen in Table 4.6. Fig. 4.10(b) shows that the structures also have a dome-like appearance. The structures fabricated by process A (Fig. 4.10(a)) and B (4.10(b)) we see that the PR mask is completely etched, resulting in the underlying structures being exposed to the ion bombardment. Because the PR mask is very easily etched, parts of the mask are removed quicker, and as a result the edges of the underlying structure is etched more than in the middle. This could be due to the mask not being completely uniform in thickness, or it could be a result of slanted sidewalls in the mask. There is also a redeposition of etch products, shown in Fig. 4.10(a) and 4.10(b). The redeposition could explain the slanted sidewalls observed in the structures. When these gas products are created, some of them are ventilated out of the chamber. But if they are created close to the structures, they may deposit on the structures instead of escaping the substrate. A more careful RIE study is needed to identify the exact mechanism and species involved in this etch process.

In order to overcome the problem of rounded surfaces on the structures, a shorter etch was performed. The first experiment resulted in more flat structures, as shown in Fig. 4.10(c), but they still had rounded edges. The height of the structures was ∼450 nm, as shown in Fig. 4.11(b). The structures also revealed much cross-linked PR being present on the structures. A shorter etch with a thinner mask was tested to have more defined PR mask edges and etching for a shorter time to create less cross-linked PR. For the PR mask with thickness=1.1

μm, a maximum structure height of ∼450 nm is possible, and Fig. 4.10(d)-4.10(g) shows the result of stopping the etch after 14 minutes. The etch resulted in structures with a height of ∼425, as shown in Fig. 4.11(c). The surfaces are very flat, and no cross-linked PR was created. The sample was not cleaned after the etch in order to identify what was removable, so the black residue observed in Fig. 4.10(d) is not cross-linked PR like in the other processes. Fig. 4.10(e)-4.10(g) show no sign of cross-linked PR. Because the sidewalls are very slanted and the height limit is poor because of the low selectivity of PR/SiC, neither of the processes are optimal for device fabrication of waveguides with vertical sidewalls and high aspect ratios. When the size decreases, the structures look more like SILs than waveguides. The structures also have the same trend we have seen earlier for the other RIE processes, that when the size decreases, the diffraction effect more strongly influences the structure morphology. Process D, with process parameters shown in Table 4.6 and resulting structures shown in Fig. 4.10(d)-4.10(g), is the optimal process for best structure morphology, and by over-etching the PR mask, dome-like structures like the ones in Fig. 4.10(a) could be made, but with less PR residue and better surface morphology. Thus the shorter route of directly etching SiC with a PR mask proved to be unsuccessful for the creation of cylindrical waveguides but instead was found to be a process for creating other interesting photonic structures like SILs in 4H-SiC.

4.5 Metal deposition

In order to produce Schottky contacts on the structures to investigate the effect of charge-state control of the defects, the PVD e-beam evaporator was used to layer a 32 nm thin nickel film on the structures. The pillars were only partially covered so the lithography design was altered by inverting the design so the mask only exposed parts of the structures. When the Ni film was deposited, only parts of the structures were covered. Then a lift-off procedure was performed in an ultrasonic acetone bath for 10 minutes. SEM images of the results are shown in Figure 4.12.

The alignment of the PR mask on the structures was challenging because of the size. As seen in Fig. 4.12, only some of the structures were covered with Ni, and metal contacts for the structures with r=1.5 μm and smaller were not achieved. The metal layer is smaller relative to the structure than for the r=3 μm case. In the tilted view, one can observe residue from Ni films that missed the structures, proving that the alignment process partially missed. This later proved to be an advantage for the characterization of the charge-state control because a comparison between pillars with and without Schottky contacts could be performed.

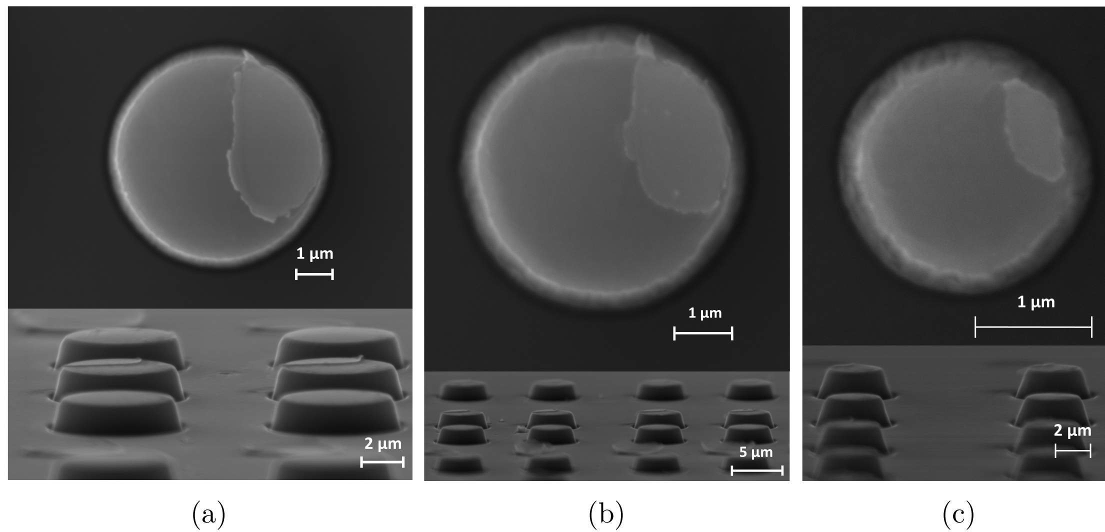

(a) (b) (c)

Figure 4.12: SEM images of structures with (a) r=3 μm, (b) r=2.5 μm, (c) r=2 μ. The top panels are images taken from above, and the lower panels are taken at an tilted angle. The Ni metal layer is the thin film on the right side of the structure. An acceleration voltage of 20 kV was used in the SEM.

In order to achieve an optimal metal contact, the manual alignment process in the Heidelberg maskless aligner has to be carefully executed. After the development of the PR mask used in this process, we observed in an optical microscope that parts of the mask were properly aligned with the structures despite the smallest structures being fully covered with PR mask. The process aimed to make Schottky contacts on the structures and then investigate the charge-state control of the defects in CL spectroscopy. The sizes of the structures were not important, so the results after the deposition were satisfactory.

Chapter 5

Results and discussion

This chapter is devoted to the characterization of the photonic structures and their properties using cathodoluminescence, both spectral and angle-resolved. Firstly, the most promising structures were implanted to generate defects. Next, the silicon vacancy signal was identified, and the CL detection optimized to maximize the detection of the intensity emaniting from the silicon vacancy. Importantly, we report on how the manufactured micro- and nanostructures impact the single-photon emission from V_{Si}, and how the Schottky barrier diodes affect the charge state of the defects situated within the depletion region. A discussion on the structures and their optical properties will also be provided.

5.1 Defect generation in the structures

From the device process developed, the most promising structures were chosen for further studies. The structures selected, including the introduction of defects by ion implantation, are shown in Figure 5.1.

Fig. 5.1(a) shows the structures made with PR directly on SiC, with a height of ~825 nm. The structures have dome-like profiles, similar to SILs. However, the over-etch of the PR resulted in substantial surface contamination because of redeposition of cross-linked PR. The structures in Fig. 5.1(b) and 5.1(c) were made by the same etch process but with a thinner PR mask. The change in mask thickness and etch duration resulted in shorter structures with a more flat surface, but the structures in Fig. 5.1(b) still had curved edges. In Fig. 5.1(c), the structures shown have flat surfaces and significantly tilted sidewalls, and there was no sign of surface contamination from redeposited PR. The height of the structures in Fig. 5.1(b) and 5.1(c) were ~425-450 nm. The different structures fabricated by the PR directly on SiC processes, shown in Fig. 5.1(a)-5.1(c), had substantially different morphology, so all were implanted to study their photonic properties.

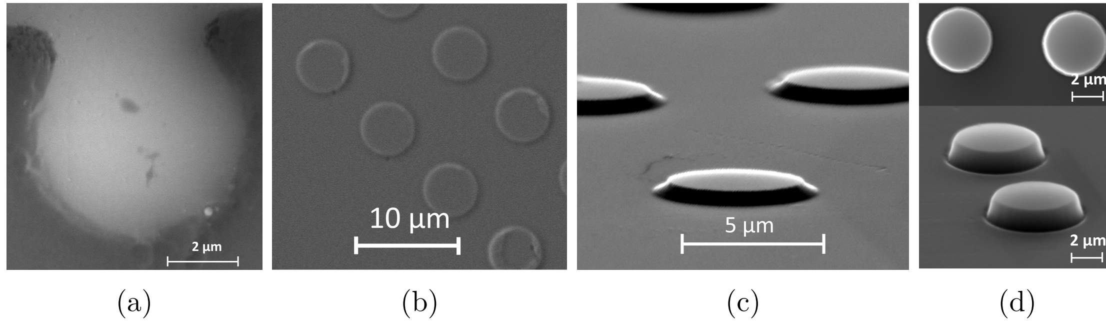

(a) (b) (c) (d)

Figure 5.1: Structures made with PR mask on SiC process with varying PR mask thickness: (a) 1.3 nm, (b) 1.2 nm, (c) 1.1 nm. Panel (d) shows structures made with a SiO_2 mask with the 3:1 gas ratio. The SEM images in (b) and (c) are taken at an acceleration voltage of 10 kV, and (a) and (d) with 30 kV.

In Chapter 4, it was shown that utilizing the fabrication process with a SiO_2 mask resulted in significantly improved structures compared to the PR on SiC process, with better sidewall profiles, structure morphology, surface contamination and height. From the SiO_2/SiC process, there was no significant difference in the structure morphology between the two optimal processes with different gas ratios. Thus, the structures fabricated by the 3:1 gas ratio, shown in Fig 5.1(d), were implanted for further study. See Tables 4.5 and 4.6 for additional information on the corresponding processing parameters.

The samples shown in Fig. 5.1 were implanted with 21 keV He ions to a fluence of 1×10^{11} cm^{-2}. The samples were already structured, so a comparison between defect emission intensity from the wafer and the structures could be performed. The ion range and vacancy generation in the material can be simulated using Monte Carlo calculations as implemented in the SRIM code (the Stopping and Range of Ions in Matter [75]). Results from the simulations of 21 keV He impacts in SiC are shown in Fig. 5.2, where the vacancy generation using displacement energy of 15 eV for Si is shown in Fig. 5.2(a), while the distribution of He is displayed in Fig. 5.2(b).

Figure 5.2 reveals that the V_{Si} is expected to be found from the surface and until a depth of approximately 200 nm, peaking at 150 nm. The projected range of the He ions is 200 nm. Thus, both the defect generation and He ions are found well within the structures. It is also worth to note that the fluence is relatively high, and isolated defect emission is not expected to be found, but this study focus rather on the emission from an ensamble of defects.

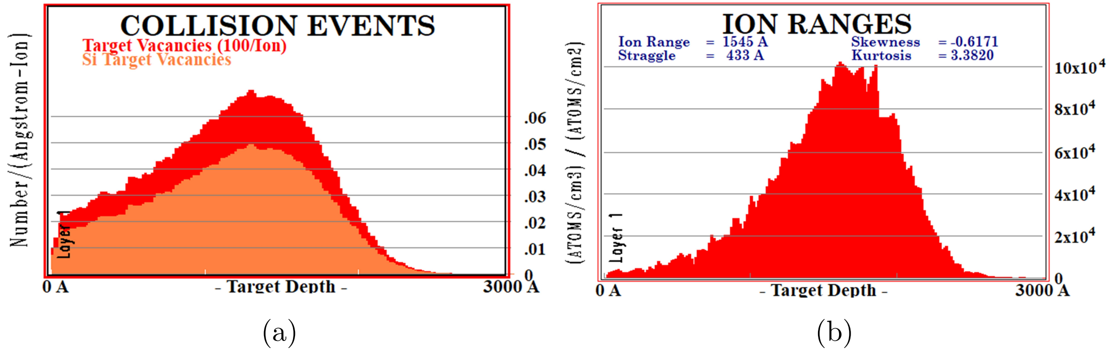

(a) (b)

Figure 5.2: Simulations from SRIM with 21 keV He implantation at a normal incident angle. Panel (a) shows the number of V_{Si} per angstrom relative to the depth in the material, and (b) shows the projected range of the ions.

5.2 Identification of the silicon vacancy

CL spectroscopy was used to identify the V_{Si} in the implanted samples. The CL setup is included in the SEM instrumentation. The SEM electron beam excites several states in the semiconductor. Certain states will produce luminescence, and the CL emission from the sample is gathered on a diffraction grating to produce a spectrum. In Figure 5.3, a typical CL spectrum from a 4H-SiC wafer implanted with the same parameters as mentioned above is shown.

Fig. 5.3(b) shows the spectrum obtained from the irradiated 4H-SiC sample from the SiO_2/SiC 3:1 gas ratio process shown in Fig. 5.1(d). Fig. 5.3(a) shows a broader CL spectrum of the same sample. The figures display the intensity measured at the detector as a function of emission wavelength. A filter blocking out light with $\lambda < 700$ nm was utilized in Fig. 5.3(b) because the emission from other deep level defects in 4H-SiC is strong and broad, and if not filtered out, will reduce the contrast of the other emission in the spectrum, as seen in Fig. 5.3(a). In this work, we are mainly interested in the emission from V_{Si}. Thus, emission from the band gap and other defect states are considered unwanted signals. Applying a filter will also involve a significant loss of detection sensitivity in the non-filtered parts of the spectrum. The loss of detection sensitivity is observed in Fig. 5.3(a), where the spectrum with filter (blue) has a reduced emission intensity compared to the non-filtered spectrum (red).

The V1' ZPL attributed to V_{Si}, as described in Section 2.4, is identified at 858 nm and the associated PSB at longer wavelengths, demonstrating that the V_{Si} was successfully created by ion implantation. However, the V1 ZPL (862 nm) is close to the V1' ZPL, so the peak indicated in Fig. 5.3(b) can be a combination of the two ZPLs. Since the V1' is attributed to the V_{Si}, the latter label is used from here

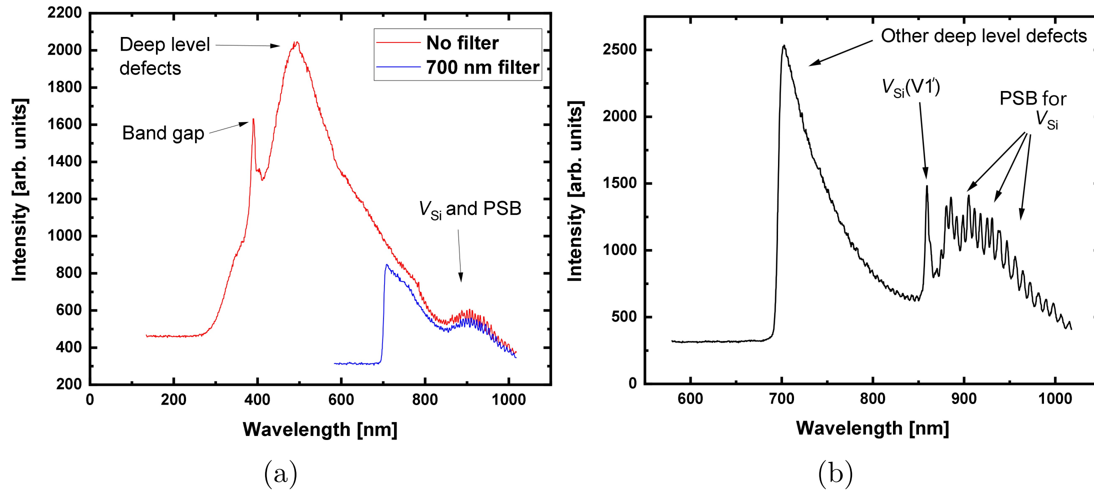

(a)

(b)

Figure 5.3: CL spectra from 4H-SiC at a temperature of 80 K. Panel (a) shows a CL spectrum of the near band edge and deep level emission compared to a spectrum with a long pass filter at 700nm, while (b) contains the near infrared emission (NIR) after filtering with a long pass filter. The e-beam used had an acceleration voltage of 20 kV and a probe current of 0.5 nA at a temperature of 80 K.

on.

The other implanted structures in Fig. 5.1 were also measured in the CL spectrometer to analyze their optical properties and are shown in Fig. 5.4 with their respective emission spectra. The CL measurements were performed to ensure that the V_{Si} was successfully implanted in all the samples.

Figure 5.4 shows the CL spectra for the irradiated structures in Fig. 5.1. Figure 5.4 reveal that in all the structures, there is emission from the V_{Si} defect in the V1' and/or V1 ZPLs and the associated PSBs, indicating the presence of the single negatively charged silicon vacancy, V_{Si}^{-}. Near band edge emission is also present in all the samples. The V1' ZPL is very sharp for the structures made from process A (PR on SiC process, seen in Fig. 5.1(a)), as shown in 5.4(a). All the CL measurements show that the phonon-sideband emission is strong, and for 5.4(c), the V1' line is overlapping with other emission lines. As all the samples were implanted together, there should statistically be only a minor difference in the defect concentrations between them. Since the material structure is the same for the CL measurements, the differences in the spectra are likely due to local variations in the defect concentration and different CL setup parameters (mirror alignment, fluctuations in temperature, specimen preparation, all the other CL acquisition settings were identical).

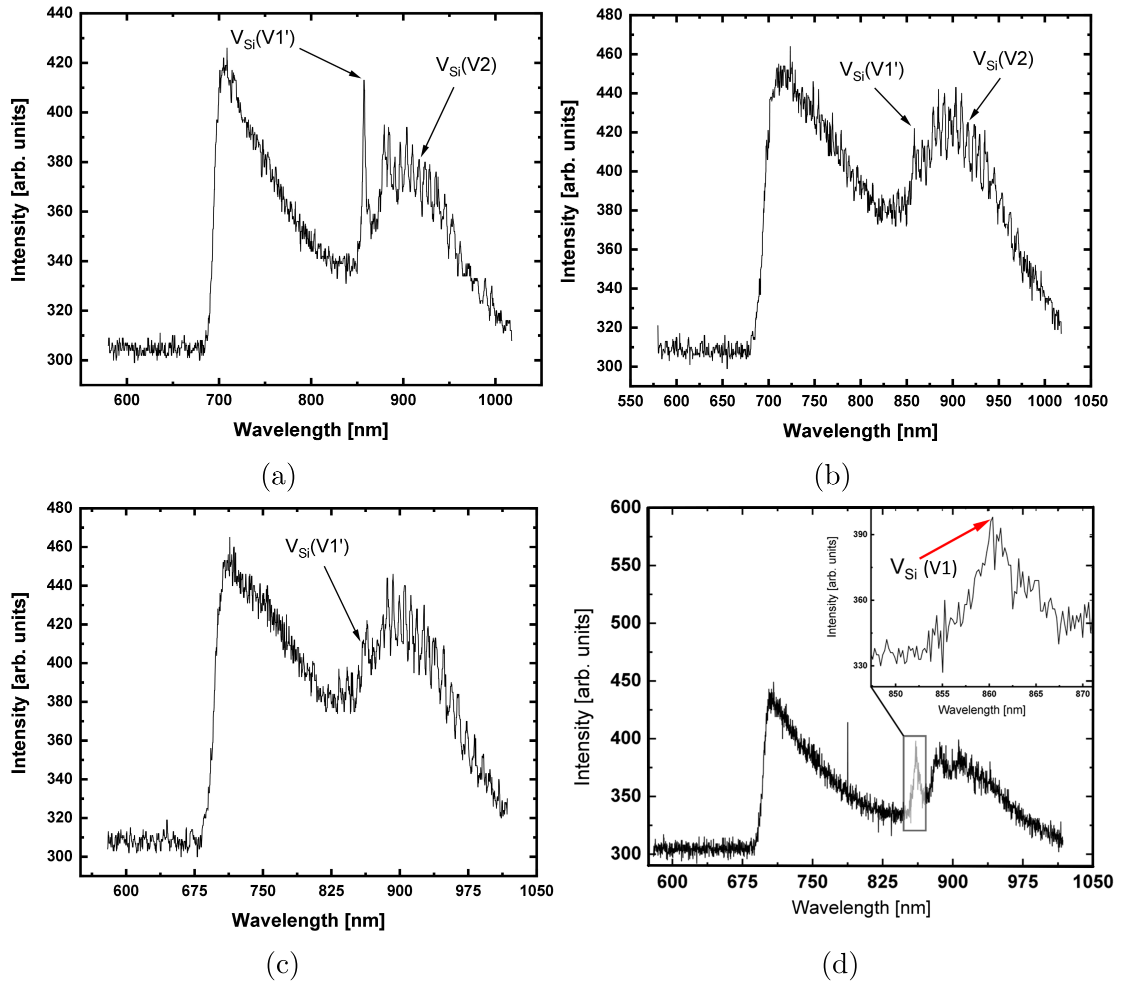

Figure 5.4: CL spectra from structures made by the PR/SiC process shown in; (a), from the dome-like structures (see 5.1(a), (b), from the shorter and flatter structures (see Fig. 5.1(b), (c), from the structures with flat surface and tilted sidewalls (see Fig. 5.1(c)). Panel (d) shows the CL spectrum from the structures fabricated with the SiO_2/SiC process (see 5.1(d)). The CL measurements were taken with an acceleration voltage of 10 kV and a probe current of 0.15 nA. All the CL measurements were collected from outside the structures (on the wafer) at a temperature of 80 K.

Generally, the CL intensity emanating from the samples was low, and the beam properties were not ideal for examining the silicon vacancy. Thus, after identifying the defect in all the samples, optimization of the CL signal was performed to find the optimal beam properties.

5.3 Optimization of the CL signal

In this section, an optimization of the CL signal and how the electron beam influences the sample will be explained. When utilizing a CL spectrometer to analyze materials, one must know the appropriate parameters for the incident electron beam. When the parabolic mirror is correctly aligned, the signal from the sample is only dependent on the acceleration voltage and the probe current. The acceleration voltage defines the energy of the electrons, while the probe current defines the number of electrons present in the beam. These two parameters were varied in order to achieve the best possible CL signal without damaging the sample.

5.3.1 Current test

As the probe current increases, the signal strength increases, similarly the signal-to-noise ratio. However, as the beam diameter increases, the resolution of the image will be lower. The beam will also damage the sample more when the probe current is increased. An example of such damage is shown in Fig. 5.5(a). Depending on the material examined, stronger probe currents will cause charging of the sample, which can result in image artifacts such as drifting of the image. For semiconductors, more incident electrons will result in stronger CL emission from the band gap and defects. Therefore a test of the emission current will give information about the optimal current to use to examine the V_{Si}.

Figure 5.5(b) shows CL spectra for varying probe currents. In Fig. 5.5(c) the highest probe current from 5.5(b), 0.5 nA, is compared to a probe current of 3.0 nA from the same sample but at a different location. Fig. 5.5(b) shows that as the probe currents are raised, the overall intensity is enhanced. As the probe current increases, more V_{Si} states are excited, but simultaneously are states excited that we are not interested in, like the PSB and other deep level defects. There is no significant enhancement in the emission intensity of the V_{Si} relative to the other features in the CL spectra.

Fig. 5.5(c) illustrates the difference in intensity and shape of the spectrum using significantly different probe currents (0.5 nA vs 3 nA). Utilizing too high probe currents will excite so many states that it is difficult to distinguish the V_{Si}. The measurements performed in Fig. 5.5(c) are from the same sample but not performed in the same session. Hence the measurement parameters may differ somewhat, and the 3.0 nA measurement has only slightly higher intensity than the V_{Si} in the 0.5 nA measurement. This is most likely because the mirror was better aligned for the measurement series, for currents from 0.1-0.5 nA, illustrated in Fig. 5.5(b).

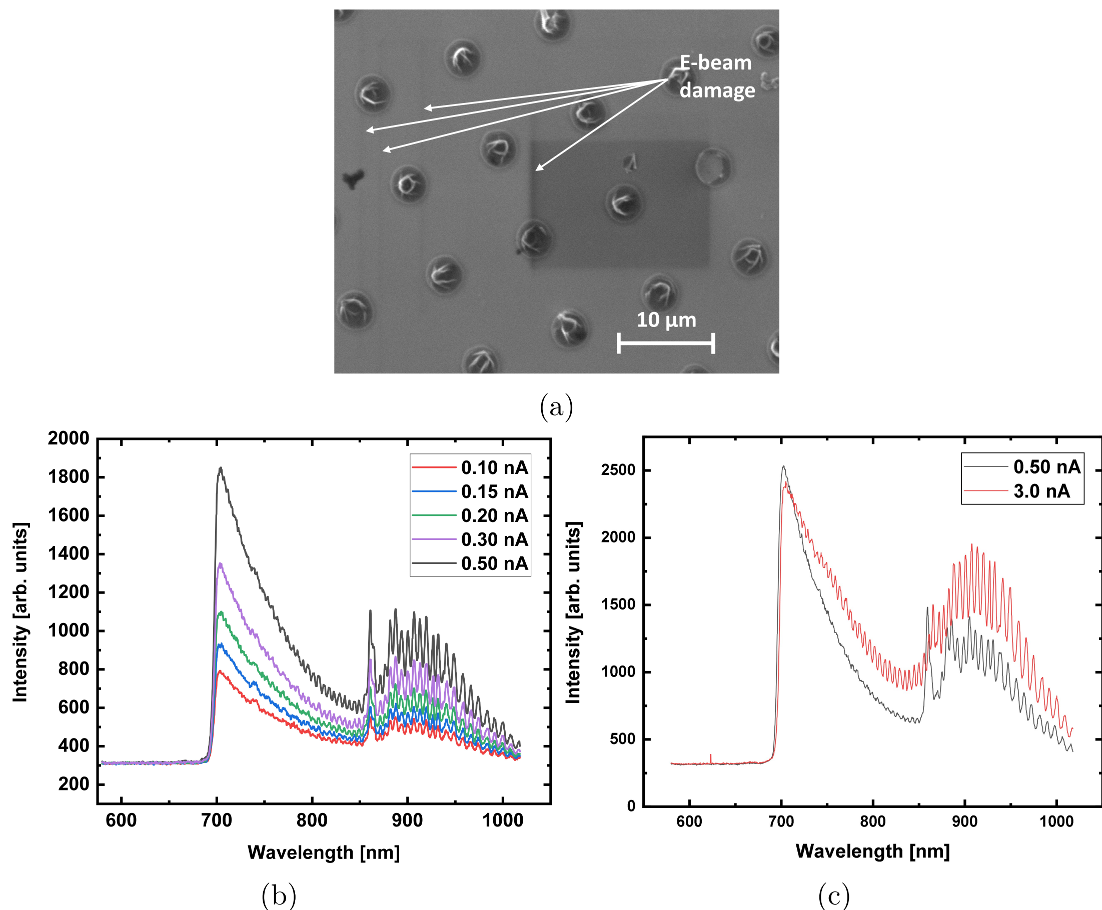

Figure 5.5: (a) is a SEM image demonstrating the beam damage that occurs at too high probe currents (acceleration voltage of 20 kV and probe current of 3.0 nA). Panel (b) is a CL measurement series with alternating currents from 0.10 nA to 0.50 nA. Panel (b) compare the 0.5 nA and 3.0 nA probe currents. All the measurements are performed at an acceleration voltage of 20 kV at a temperature of 80 K.

The sampling is also from a different location on the sample. The goal here was to examine how the probe current affects the emission intensity and the sample surface. Thus, the 3.0 nA measurement gave useful information about the consequences of utilizing too high probe currents, although the measurements can not be directly compared. Additionally, a high probe current will cause significant damage to the sample, as shown in Figure 5.5(a) for probe current of 3.0 nA and an acceleration voltage of 20 kV.

From this current test and other CL measurements not shown here, it was found that depending on the sample surface contamination and the mirror alignment, a

probe current in the range 0.1 nA to 0.5 is appropriate for acquiring a spectrum with high signal-to-noise ratio and high resolution from the V_{Si} in 4H-SiC.

5.3.2 Voltage test

The interaction mainly only depends on the incident electron energy from a given sample, which is determined by the acceleration voltage. By varying the acceleration voltage, it is thus possible to estimate the implanted defects' depth profile. By comparing the attained spectra for different acceleration voltages with SEM simulations from a software such as CASINO and simulations from TRIM, the depth profile of the defects can be approximated. CASINO is a software that simulates the electron trajectory from incident electron beams in solid materials [76].
In the experiment to ascertain the defect depth profiles, the probe current was held constant at 2 nA for all the measurements. The reason for using a high probe current was to obtain a high signal-to-noise ratio, and not necessarily to distinguish the V_{Si}. The projected depth was found to be around 200 nm in the SRIM simulation (see Fig. 5.2). Fig. 5.6 shows the CL spectra for the different acceleration voltages.

Fig. 5.6 shows that as the acceleration voltage is increased and we probe deeper into the sample, the emission intensity from all states is enhanced. The signal-to-noise ratio is also higher for higher acceleration voltages. However, the emission intensity from the V_{Si} relative to the emission intensity from the other deep level defects is suppressed for higher acceleration voltages, as seen in Fig. 5.6. The lines at the right in the spectra indicate the relative emission intensity of the defects with respect to the highest intensity in each spectrum. The relative defect emission intensity is strongest at an acceleration voltage of 2.5 kV. By comparing with the simulations performed in CASINO in Appendix B, the electron beam's probe depth for an acceleration voltage of 2.5 kV is approximately 70 nm in 4H-SiC. For an acceleration voltage of 5 kV, the probe depth is approx. 200 nm. The TRIM simulations in Fig. 5.2 showed that the V_{Si} concentration peaked at approx. 150 nm. We expect the near band edge emission intensity and deep defect emission intensity from other defects to increase proportional to the interaction volume, and thus also to the acceleration voltage. However, based on the TRIM simulations, the V_{Si} is prevalent only in the first 200 nm of the material. As we probe deeper into the material, we expect to see a reduction in the relative emission intensity from the V_{Si}, which the trend observed in Fig. 5.6 reveals.
Fig. 5.6 also shows that at low acceleration voltages, the signal-to-noise ratio is low, and to achieve a satisfactory signal, a higher acceleration voltage should be used. An acceleration voltage of 10 kV would yield a high signal-to-noise ratio but a lower V_{Si} emission intensity. To overcome the problem of lower relative emission signal from the V_{Si}, the defects can be implanted deeper into the material. The

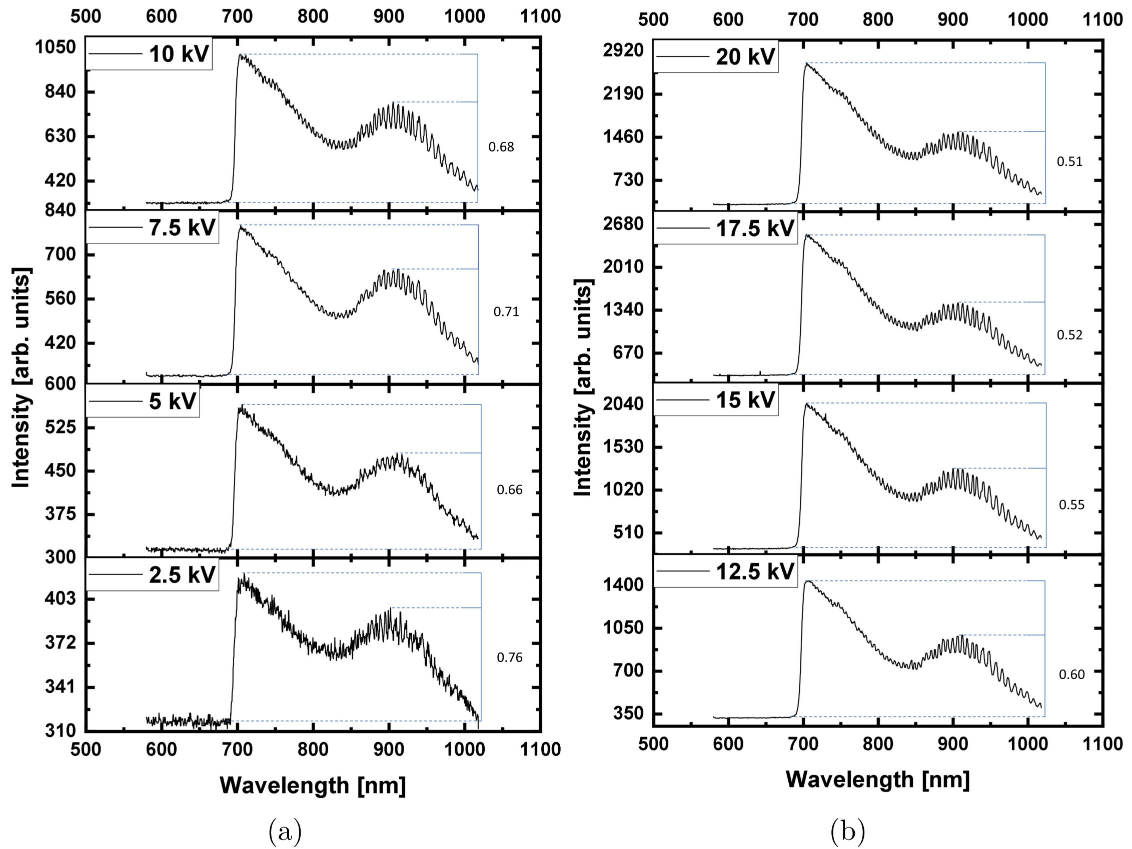

(a) (b)

Figure 5.6: CL measurements series with alternating acceleration voltage from (a) 2.5 to 10 kV, and (b) 12.5 to 20 kV. The probe current was held constant at 2 nA at a temperature of 80 K.

results provided here are based on simulations, thus to properly examine the depth of the implanted defects, other characterization techniques should be used.

From the voltage test, the optimal acceleration voltage was found to be 10 kV. Unfortunately, the SEM filament had begun to degrade, so a higher acceleration voltage had to be used for subsequent measurements.

From the CL optimization, it was also found that the exposure time was a significant parameter for high quality CL measurements. Exposure time is the duration the detector is exposed to each CL pixel, while acquisition time is the total time for complete CL measurement (exposure time $\times$ number of pixels). In general, a longer exposure time resulted in a CL signal with higher intensity and a high signal-to-noise ratio, but the exposure time should be chosen depending on the type of measurement performed.

5.4 Cathodoluminescence measurements of the $V_{\rm Si}$ emission from the structures

Hitherto, the $V_{\rm Si}^{-}$ has been identified in all the samples. To investigate how the photonic properties of the structures influence the $V_{\rm Si}^{-}$ emission intensity, a CL intensity mapping of the structures was performed. The most promising structures made with the SiO_2/SiC process with 3:1 gas ratio were again examined, as they were closest to the objective of cylindrical waveguides. Figure 5.7 shows a CL intensity mapping of the structures.

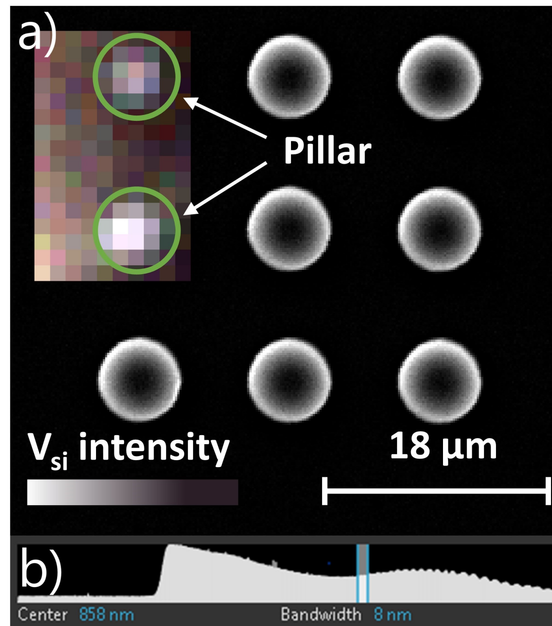

Figure 5.7: Panel (a) shows a CL mapping of the structures made with the SiO_2/SiC process with 3:1 gas ratio with r=3 μm. The green lines in the CL intensity map outline the structures. The acceleration voltage used was 20 kV and the probe current 2 nA, at 80 K. In panel (b), the broadband filter setting is shown with the interval chosen.

Fig. 5.7(a) displays the SEM image of the structures with a CL intensity map superimposed on the image. Fig. 5.7(b) shows the bandwidth setting used in the post-production software Odemis. The bandwidth was set to 8 nm centered on 858 nm to highlight the intensity from the $V_{\rm Si}^{-}$. The grayscale bar indicates the intensity of each pixel relative to the bandwidth, meaning that brighter pixels had stronger emission intensity in the chosen wavelength interval. The exposure time of each pixel was set to 1 second, and a long pass filter at 700 nm was used to block out near band edge emission.

As demonstrated in Fig. 5.7(a), the intensity from within the V_{Si}^{-} is considerably stronger from the structures compared to outside. In the selected bandwidth there is about an 2-fold increase in emission intensity compared to the emission from the wafer. Thus, the photonic properties of the structures will enhance the emission intensity from the V_{Si}^{-}.

The smaller structures were also measured by similar means, but due to errors during the acquisition of the measurements, the results for the structures with r=2.5 μm, 2 μm and 1.5 μm were not included here. The smallest structures with r=1 μm were succesfully measured, and a CL map measurement is shown in Fig. 5.8(a).

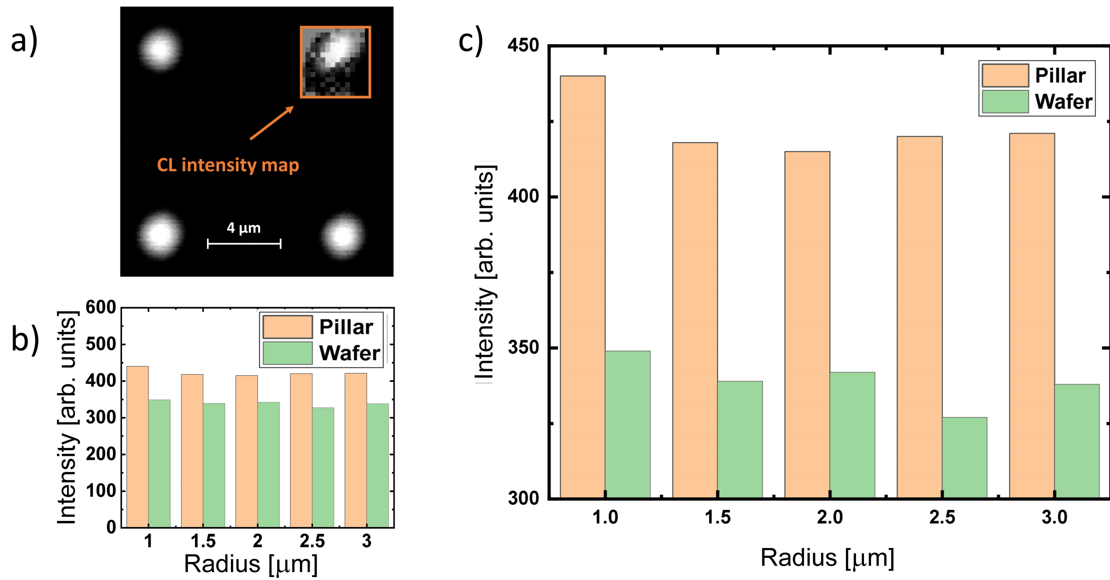

Figure 5.8: Panel (a) shows a CL map superimposed on a SEM image of the r=1 μm structures made with the SiO_2/SiC process with 3:1 gas ratio. The acceleration voltage used was 20 kV and the probe current 2 nA, at 80 K. Panel (c) shows a bar chart of the CL emission of the different sized structures compared to the wafer. Panel (c) is a zoomed inlet of the same chart with a different y-scale.

Fig. 5.8 shows the SEM image of the r=1 μm structures with a CL intensity map superimposed on the image. The same bandwidth as in Fig. 5.7 was used. As seen in Fig. 5.8, there was some drift of the image, but not significant for the purpose of this measurement. The drift occured due to a long exposure time (10 s). The bright pixels in the middle of the structure in Fig. 5.8 reveals that the V_{Si}^{-} emission intensity is enhanced in the pillar, compared to the emission from the wafer.

Fig. 5.8(b) shows a bar chart of the intensity of the different sized structures compared to that of the wafer. These measurements were not from the same session as the measurements in Fig. 5.7 and 5.8. Fig. 5.8(c) shows a zoomed inlet of the same bar chart to highlight the differences in emission intensity. A bandwidth of 8 nm centered on 858 nm was chosen for these measurements also. Indeed Fig. 5.8(c) confirm that the emission intensity from the pillars is enhanced compared to the wafer for all structures. There is no significant difference between the emission intensity from the pillars with size r=3-1.5 μm. However, for the structure with r=1 μm, the emission intensity is stronger than all the other structures. The measurements were only performed at one pillar for each size, so more data is required to validate if there is an statistically significant difference in the emission intensities. Moreover, at r=1 μm, the size of the photonic structure is approaching the wavelength of the V1' line (858 nm). Thus, Fig. 5.8(b) may indicate a waveguiding effect occuring for the smallest pillars. As seen in Fig. 4.8, the shape of the r=1 μm structure is not cylindrical, so how this shape influences the V_{Si}^{-} emission should be studied.

The enhancement of the defect emission intensity proves that the pillars may act as photonic structures for the V_{Si}. In order to conclude if there is a waveguiding effect occuring, i.e., propagation in discrete modes, further study on the radiation profiles of the structures should be performed. Such measurements are presented in the next section.

5.5 Angle-resolved emission from the 4H-SiC structures

So far, the silicon vacancy has been identified in all the samples and CL measurements on the micropillars revealed an nearly 2-fold increase in emission intensity from the micropillars, indicating a waveguiding effect. In this section, the photonic properties of the structures will be examined more closely. The structures chosen for the measurements were the cylindrical pillars made with the SiO_2/SiC process with 3:1 gas ratio, because they were proven to enhance the emission intensity of the V_{Si}.

5.5.1 Angle-resolved cathodoluminescence measurements

To examine the radiation profile of the structures, angle-resolved cathodoluminescence (ARCL) was used. This technique had not been used in the research group previously. Thus an important objective was to develop AR measurements and the related analysis at MiNaLab. As described in Section 3.2.3, an ARCL measurement will give information about the intensity with respect to the emitted direction above the sample. The signals are collected by a parabolic mirror and projected onto a CCD screen. The software transforms the 2D image on the CCD screen into a polar plot. These polar plots are 2D representations of the hemisphere above the sample. A 2D polar plot will describe the far-field radiation pattern of materials and photonic structures. Each point in the plot has a unique θ and ϕ angle associated with it, as shown in Figure 5.9. The brightness of each point gives the intensity originating from the associated angles.

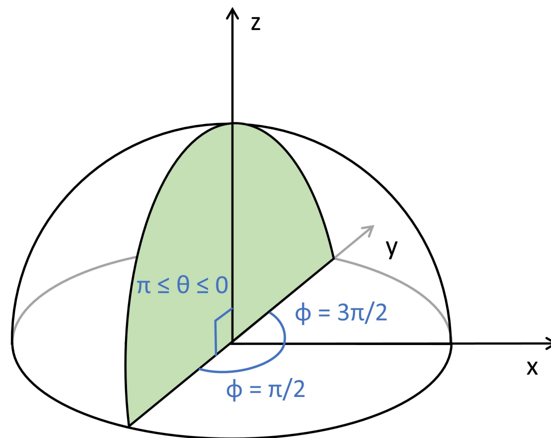

Figure 5.9: Shows the unit hemisphere, with the green plane indicating where the cross-section polar plots are extracted from.

Fig. 5.9 shows the unit hemisphere above the sample. A green plane is highlighted at $\phi=\pi/2$ and $3\pi/2$. By varying the θ angle in this cross-section plane, the side view of the radiation pattern can be plotted to reveal the radiation profile of the material. Most semiconductors emit incoherent CL signals and are Lambertian emitters. There may be surface effects such as plasmons present, which will have different radiation profiles, but generally, the near band edge emission and the defect emission are substantially stronger. Thus, by comparing the radiation patterns and profiles of the micropillars and the wafer, the photonic properties of the fabricated structures can be determined.

When preparing for an AR measurement, the CCD screen had to be aligned with the signal from the mirror. An image from the CCD screen assisted this alignment, but it was found that the probe currents used to do the CL measurements described above did not produce an image on the CCD screen because the emission signal was too weak. Therefore the probe current was increased to values that normally would cause damage to the sample (as seen in Fig. 5.5(a)) and drift in the image. Damage of SiC usually occurs when the beam is stationary for more extended time durations (> 2 minutes) at high probe currents. However, AR measurements are short (max. 120 seconds), so the sample damage was negligible. Without a filter, the emission was strong, so low exposure times were used to avoid damage of the image sensors. When using a filter, the exposure time was increased to achieve an image with similar intensity as with no filter. Measurements with and without filter were performed to examine any difference in the radiation profile from the near band edge and the defects.

For every AR measurement, a dark measurement was performed by blanking the e-beam. This is performed to remove background effects and artifacts. When changing the e-beam acceleration voltage, small shifts in the e-beam position occurs. The complication of this was that the dark AR measurements were not performed at exactly the same position on the structures. In some instances, this resulted in AR measurements with significant background noise that had to be discarded.

AR measurements were performed on all the different sized structures shown in Fig. 4.8 made with the SiO_2/SiC process with 3:1 gas ratio. Fig. 5.10 and 5.12 show these AR measurements. The remaining AR measurements are included in Appendix C.

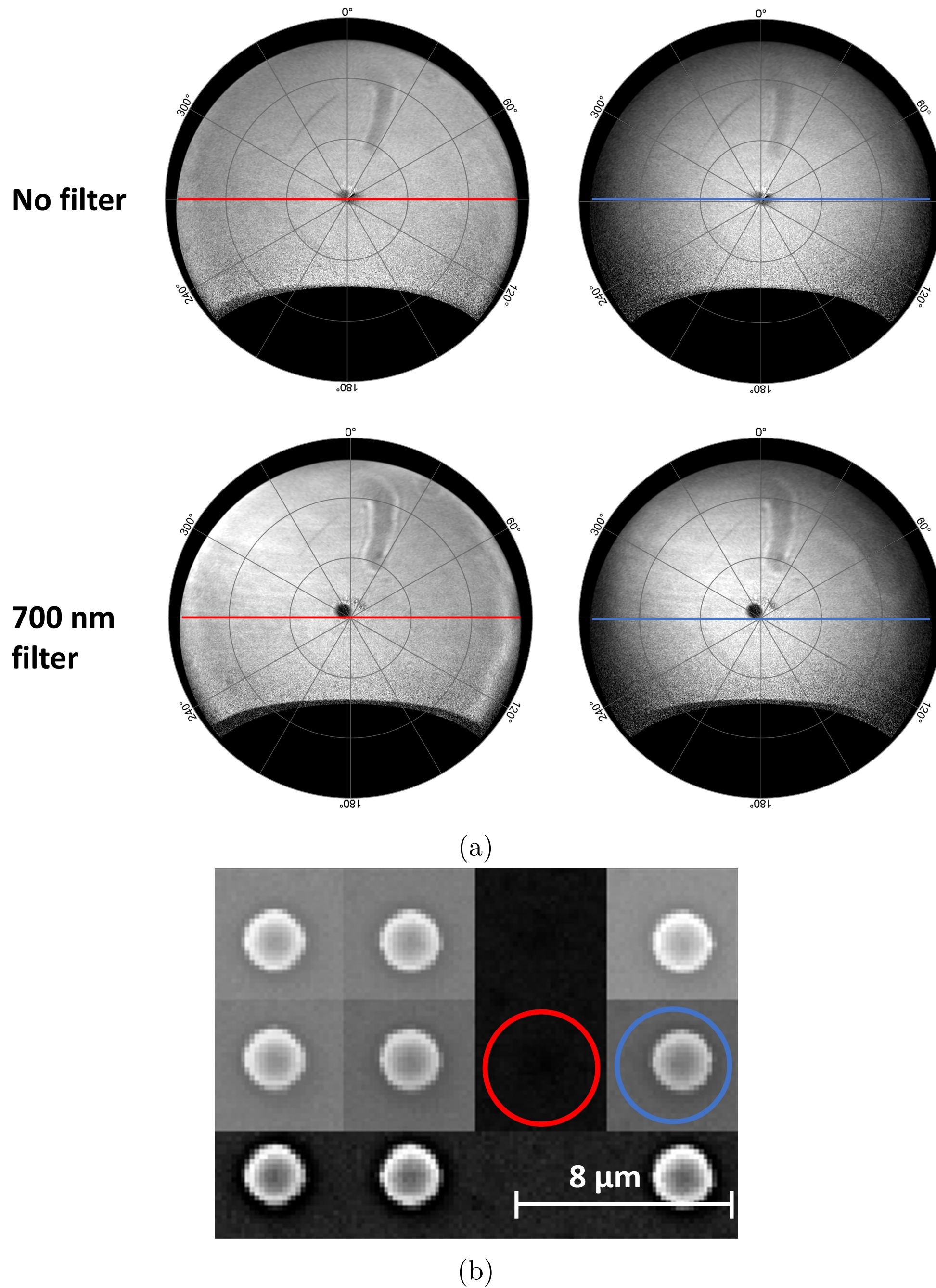

Figure 5.10: (a) shows polar plots of AR measurements done on a structure (blue) with r=3 μm and a wafer (red), with measurement position indicated by the color codes in the SEM image in (b). The acceleration voltage used was 20 kV, and the probe current was 2 nA, at a temperature of 80 K.

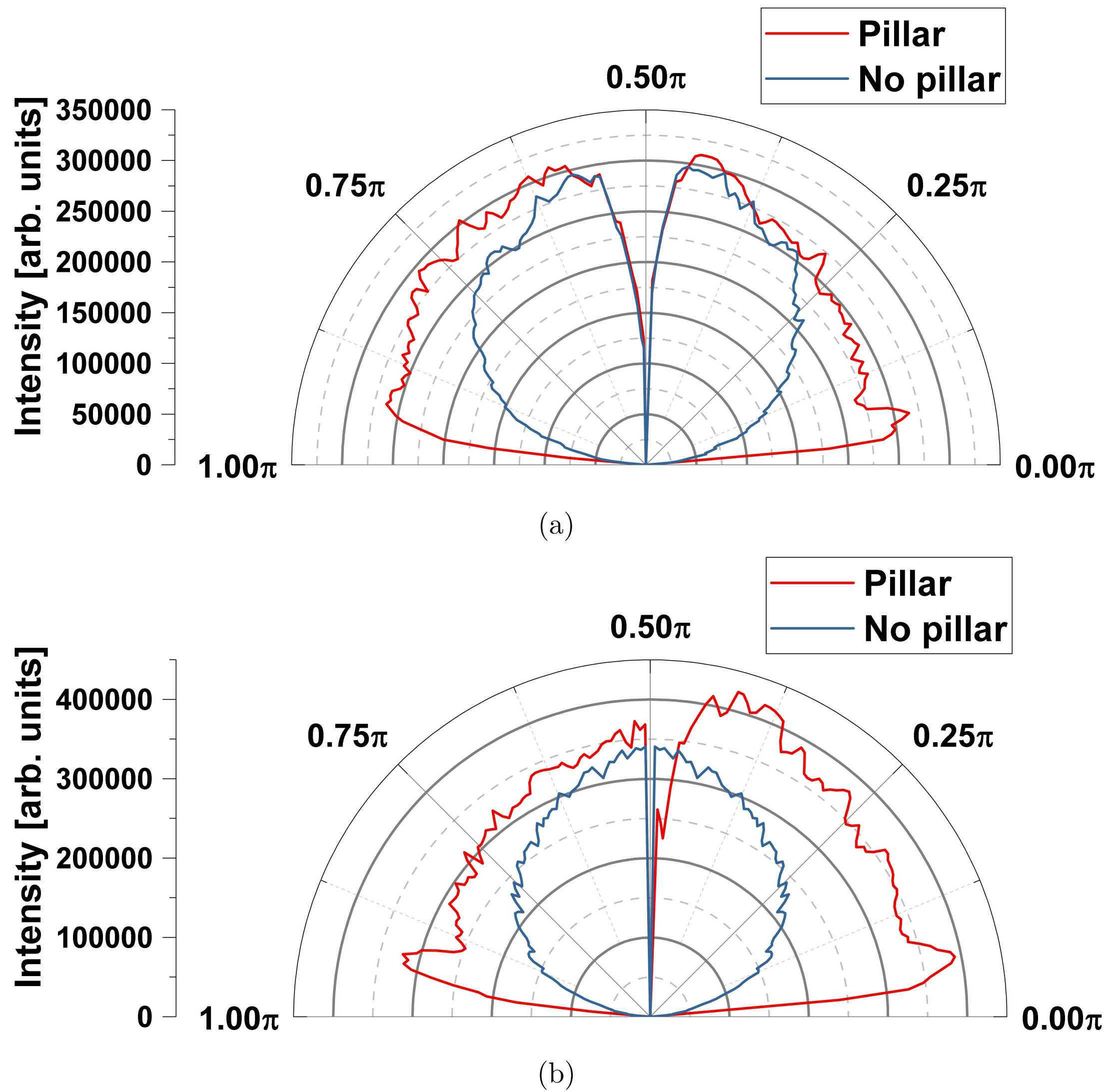

Figure 5.11: (a) and (b) are polar plot cross-sections at $\phi=\pi/2$ and $3\pi/2$ on the structures with r=3 μm. (a) is from the measurement without filter, and (b) is with a 700 nm filter. The acceleration voltage used was 20 kV, and the probe current was 2 nA, at a temperature of 80 K.

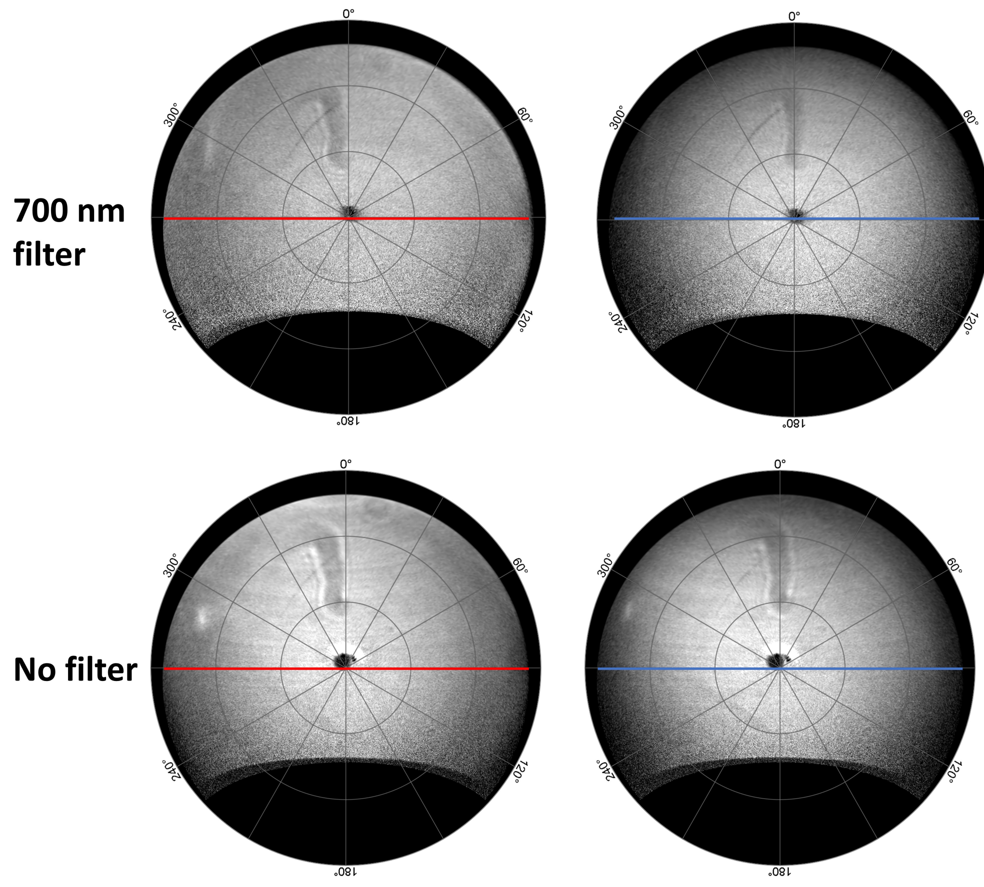

(a)

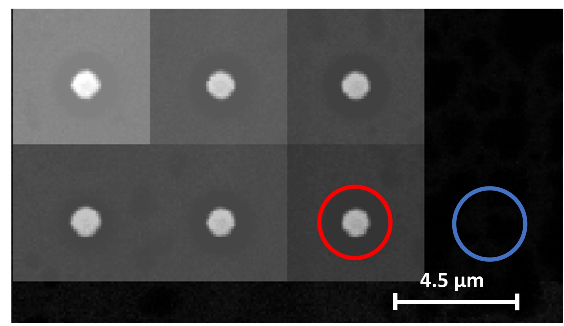

(b)

Figure 5.12: (a) shows polar plots of AR measurements done on a structure (red) and a wafer (blue) with r=1.5 μm, with measurement positions indicated by the color codes in the SEM image in (b). The acceleration voltage used was 20 kV, and the probe current was 2, nA at a temperature of 80 K.

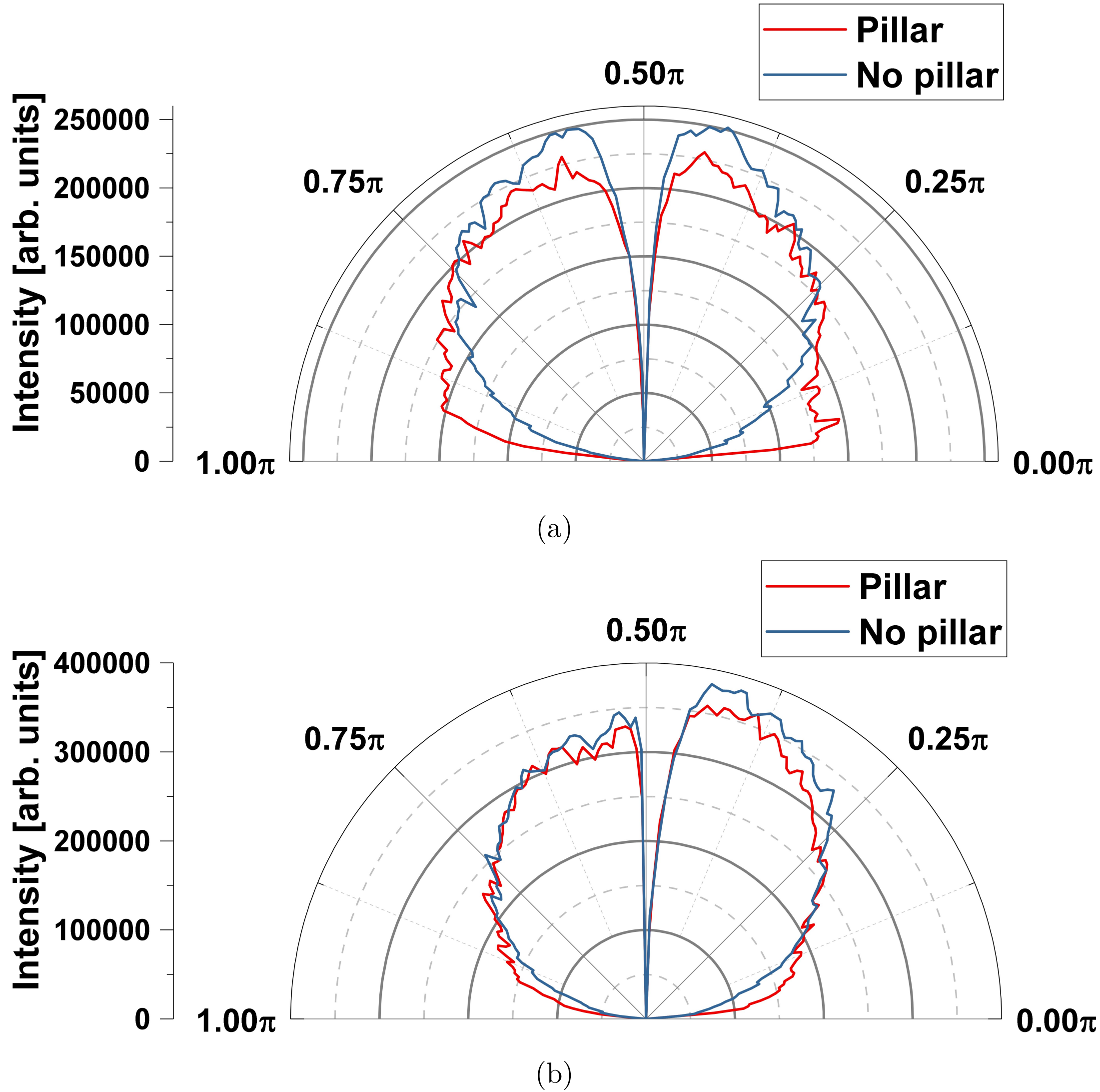

Figure 5.13: (a) and (b) are polar plot cross-sections at $\phi=\pi/2$ and $3\pi/2$ on the structures with r=1.5 μm. (a) is from the measurement without filter, and (b) is with a 700 nm filter. The acceleration voltage used was 20 kV, and the probe current was 2 nA, at a temperature of 80 K.

Figures 5.10(a) and 5.12(a) show the polar plots from the structures compared to the wafer. There is zero intensity in the middle of the plots, which results from the hole in the mirror for the incident electron beam. The exposure times for the filter measurements were 60 seconds and 10 seconds for the no filter case.

The SEM images in Fig. 5.10(b) and 5.12(b) indicate from where the polar plots are acquired. Fig. 5.11(a), 5.11(b), 5.13(a), and 5.13(b) show how the intensity

varies over the θ angle in the structures compared to the wafer at a cross-section in ϕ angle (cross-section illustrated in Fig. 5.9), and describes the radiation profiles.

In Fig. 5.10(a), the polar plots show an increase in intensity in the r=3 μm pillars for all angles compared to that of the wafer, and this is confirmed in Fig. 5.11(a) and 5.11(b) (shown in red). The radiation profiles in Fig. 5.11(a) and 5.11(b) reveal an increase in emission intensity for all θ angles compared to the wafer. An interesting effect is the spike in intensity for the widest θ angles. By comparison, the radiation profile of the wafer (shown in blue in Fig. 5.11(a) and 5.11(b)) is very close to a Lambertian emitter, which is what we expect from SiC. AR measurements were performed on the structures with r=3 μm and r=2 μm as well, with similar radiation profiles. They are shown in Appendix C. None of the polar plots shown in Fig. 5.10(a) have far-field radiation patterns that indicate a waveguiding effect, which is expected since the size of the structures is significantly larger than the wavelength of the emitted light.

In Fig. 5.12(a), the polar plots show an increase in intensity for certain angles, but not the angles where Fig. 5.13(b) and 5.13(a) are sampled. Fig. 5.13(a) even shows a decrease in intensity for small θ angles. Fig. 5.13(a) shows that the radiation profile of the structure is nearly identical to that of the wafer. Since the defect emission originates from approximately 150 nm into the structure, we expect to observe a difference in the radiation profiles of the smaller structures relative to the wafer. An explanation for the low emission intensity from the smallest structures is that when the measurements in Fig. 5.12 were completed, the acquisition area was set in a way, so multiple structures were included in the same measurement. Because the structures are smaller than the previous ones, but the magnification was the same, it was not easy to properly center each scan on a structure. In Fig. 5.13(b), the radiation profile of the structure is almost identical to the wafer, and in 5.13(a) the intensity is lower than that from the wafer. In addition to the problem with the acquisition of the measurement, the interaction volume is large for an acceleration voltage of 20 kV. Thus, areas around the structure will also emit and contribute to the signal.

For ideal waveguides, the EM waves will travel as discrete modes. However, this effect is not observed for any of the structures shown in Fig. 5.10 and 5.12, since the structures are significantly larger than the wavelength of the emitted light. Thus a model based on geometric optics can explain the increase in intensity observed in the structures. Such a model is shown in Fig. 5.14.

Fig. 5.14 shows how light rays with origin in the material are refracted as they meet the air-SiC interface. At a certain angle called the *critical angle*, no light will escape the interface. The schematic representation of the structures shows how they will increase the amount of light that escapes the material. The tilted

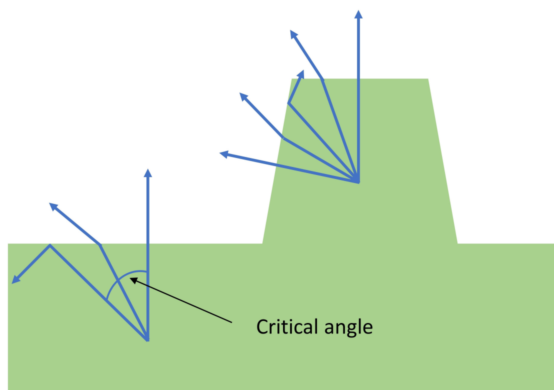

Figure 5.14: A schematic representation of light rays emitted from defects that reside in the wafer and the structures. Light incident on the interface at angles wider than a critical angle will be subjected to total internal reflection.

sidewalls of the structures explain how the intensity increases, as observed in Fig. 5.11(a) and 5.11(b) for the widest θ angles. At these angles, the light rays will be normally incident on the interface and thus not refracted. Since more light is escaping from the sides of the the pillars than if the sidewalls were straight, they have similar properties to a lens. This means that the structures influence the emission of the material by increasing the amount of light that escapes the semiconductor-air interface by a combination of total internal reflection and a lens-like effect from the tilted sidewalls. The overall effect is an increase in the numerical aperture relative to the wafer.

As explained in Section 2.5, SILs are used to increase the numerical aperture of a material by fabricating a lens with a high-refractive-index solid material. For semiconductor materials with a high refractive index, like diamond and SiC, SILs can overcome the problem of low luminescence emission [55][13][56][57][58]. The commonly used fabrication of SILs in diamond involves focused ion milling. This method is time consuming and not feasible for large scale manufacturing [55]. Sardi *et al.* proposed a fabrication method of SILs involving RIE of SiC with a photoresist mask [55], similar to the process developed in this thesis. The SILs fabricated showed a 3.4 times enhancement in collection efficiency of implanted V_{Si} single photon emitters, as measured by confocal microscopy [55]. The study by Sardi *et al.* also discuss different shaped SILs based on simulations in the software Comsol. They compare round shaped SILs (as in Fig. 2.12) with elliptical shaped and cone shaped with a flat tip. The cone shaped photonic structure simulated were similar to the structure shown to the right in Fig. 5.14 and the smaller structures fabricated by the SiO_2-on-SiC process in this thesis (r=1.5 μm, r=1 μm). In the simulation, the cones were significantly superior at enhancing the

collection efficiency (18 times enhancement) compared to the round and elliptical shaped SILs [55].

Thus, the structures fabricated in this thesis are promising for enhancing the emission intensity and are potentially feasible for large scale manufacturing. ARCL is new and not yet an established technique in the MiNaLab, so the results presented here and the learning process by acquiring them will be beneficial for future work on both 4H-SiC and other materials.

5.6 Charge-state control of the V_{Si}

The process developed in this thesis included a method for depositing metal layers on the structures. Schottky barrier diodes were fabricated by depositing nickel on parts of the structures, and an example of such a Schottky contact is shown in Figure 5.15.

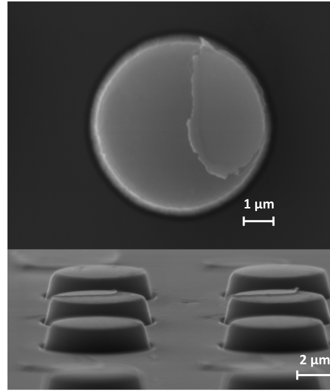

Figure 5.15: Structure with r=3 μm. The top panel of the SEM image is taken from above the structure, and the lower panel is taken at a tilted angle. The Ni metal layer is the thin film on the right side of the structure in the top panel. The SEM image is taken at an acceleration voltage of 20 kV.

The structures in Fig. 5.15 were made with the 3:1 gas ratio, and the metal layer deposited was approximately 32 nm thick. The structures were implanted with helium ions before the metal deposition to form the V_{Si} defects.
In a Schottky barrier diode, a depletion region is formed in a volume around the junction. The different charge states of the defects follow the band edges, see Fig. 2.11, such that a shift in the Fermi level can alter the occupation of the defect states. The height of the Schottky barrier and the width of the depletion region depend on the doping of the semiconductor and the work function of the metal used.

In this thesis, nickel is used as a metal layer, and the depletion region width is calculated by Eq. (2.13) to be 2.3 μm without applied bias. Note that the SEM-CL system did not allow for external bias to be applied to the sample, hence only the built-in voltage of the Schottky contact was used here. Outside of the junction, the V_{Si}^{3-} charge-state is preferred as the Fermi level is close to the conduction band edge, and this is the charge state closest to the Fermi level. Formation of a Schottky barrier between the Ni and SiC causes band bending in the semiconductor. Inside the depletion region, the singly negative charge state of V_{Si} will therefore dominate. From this, we expect to see a stronger emission intensity from the V_{Si}^{-} in the depletion region as compared to outside, and that the intensity decreases when moving further away from the Schottky junction.
To examine the charge-state control of the Schottky contact, the structures in Fig. 5.15 were analyzed with CL.

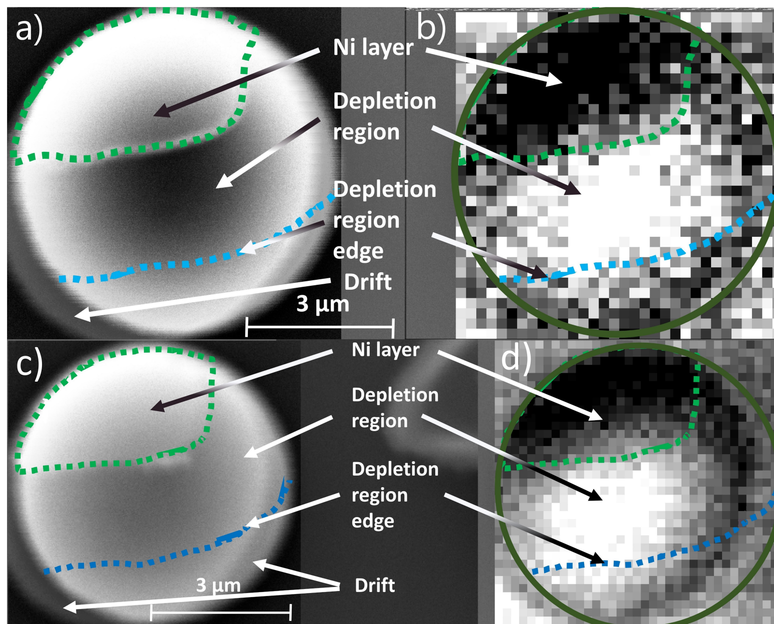

Figure 5.16: (a) and (c) are SEM images of a structure made with the 3:1 gas flow ratio with r=3 μm, but from different CL measurements. Panels (b) and (d) are CL intensity maps of the same structure. A bandwidth of 8 nm centered on 858 nm is used to filter out the V_{Si} signal . The Ni layer and depletion region edge are illustrated by green and blue dotted lines, respectively. The depletion region edge is marked at a distance of approximately 2.3 μm from the metal contact. An acceleration voltage of 20 kV and probe current of 0.3 nA were used for the electron beam at a temperature of 80 K.

Figure 5.16 shows SEM images in (a) and (c) with both the Ni layer and

depletion region highlighted by green and blue lines, respectively. The blurry parts of the structures are image drift due to the charging of the sample. In Fig. 5.16(b) and (d) the CL intensity maps are superimposed on the SEM image. Each pixel corresponds to a CL measurement point. A bandwidth setting was used in the post-production software. The bandwidth was set to 8 nm centered on 858 nm to highlight intensity from the V_{Si}^{-}, as was shown in Fig. 5.7(b). The grayscale of the pixels indicates the intensity relative to the bandwidth. The exposure time of each pixel was set to 1 second in both measurements. Note that Fig. 5.16 displays overall intensity reaching the detector, not only the V1' V_{Si} line. However, a long pass filter at 700 nm was used to block out emission from the near band edge and other deep level defects.

The results shown in Fig. 5.16 reveal low CL emission from the Ni layer, which is expected. Metals with no nanostructures only have CL emission due to surface effects like plasmons, but they are generally substantially weaker than the CL emission from semiconductors. An acceleration voltage of 20 kV was used. Thus the probe depth was larger than the Ni layer, and the SiC underneath yielded some CL emission. Fig. 5.16 reveals that in the depletion region, the emission intensity from the V_{Si}^{-} is significantly stronger than from other places on the structure and on the wafer. The V_{Si}^{-} emission close to the edges of the structure is also lower than in the middle. At the edge of the depletion region, the emission is gradually becoming lower. Note that the acquisition time was long, resulting in a significant drift of the sample. This could be due to charging, thermal expansion due to heating of the sample stage, or vibrations from the outside environment. The temperature was kept at 80 K through all the measurements by continuously reapplying liquid N_2 to the sample stage cooling system, and the system is designed to withstand vibrations, so the image drift is most likely due to the charging of the sample. It is not straightforward to precisely know exactly what effects occur at the structure edges inside the depletion region because the drift in the image is significant at the structure edges. If the V_{Si} intensity is lower here than in the middle, a comparison of V_{Si} intensity from a structure with and without a Schottky contact has to be compared to understand how the charge-state control influences the defect emission.

From the optimization of the CL signal, it was found that longer exposure times gave substantially better CL emission signals. However, long acquisition times resulted in a substantial drift, distorting the CL intensity around the pillars. The CL measurements in Fig. 5.16 above used short exposure times, so another measurement was performed with an exposure time of 10 seconds. To avoid long acquisition time, a smaller area was chosen to reduce the drift. This result is shown in Fig. 5.17.

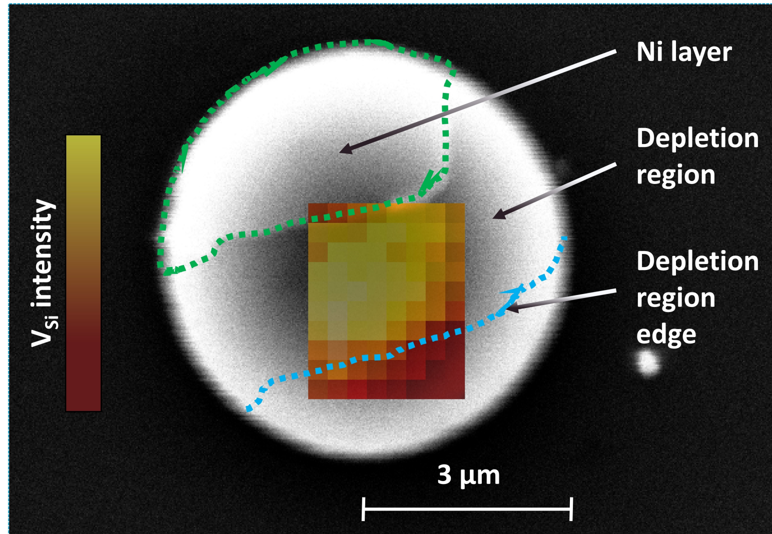

Figure 5.17: An SEM image of a structure made with the 3:1 gas flow ratio and with r=3 μm. A CL intensity map is shown in the middle of the structure. The red/yellow color bar represents the intensity in the bandwidth, and the colors are added for illustrative purposes. The Ni layer and depletion region edge is illustrated by green and blue dotted lines, respectively. The depletion region edge is marked at a distance of 2.3 μm from the metal contact. An acceleration voltage of 20 kV and probe current 0.3 nA was used for the e-beam.

The CL intensity map in Fig. 5.17 shows a considerably higher resolution than in Fig. 5.16, and there is no visible drift in the image. As the previous measurements, a long pass filter at 700 nm was used. The results in Fig. 5.17 reveal that the V_{Si}^{-} emission intensity is substantially increased in the depletion region. The enhancement of emission intensity for the V_{Si}^{-} indicates that charge-state control was achieved by utilizing a Schottky barrier diode. Since a smaller area was examined, the drift was negligible. With a longer exposure time, the CL emission signal has significantly higher intensity than in the previous measurements. In Fig. 5.16, the V_{Si}^{-} intensity is decreasing close to the edge of the depletion region. Due to drift in the sample, it was impossible to determine if this intensity reduction occurred due to the photonic structures or an error during acquisition. The CL acquisition area in Fig. 5.17 is close to the middle of the structure. Thus, to to fully understand the charge-state control of the V_{Si}^{-}, the whole structure should be measured. To examine the whole structure without having too much image drift, smaller sections should be measured one at a time, and then combined to understand how the Schottky contact influences the V_{Si} charge state. Such measurements should be compared to a high resolution CL mapping of the structures without Schottky contacts to examine the effects that occur at the edges of the

structures. Unfortunately, there was not enough time for such measurements in this thesis, and should rather be persuaded in further work.

Chapter 6

Concluding remarks and further work

In this thesis, advancements have been made in establishing silicon carbide and its quantum compatible defects as a candidate for novel and existing quantum technologies. In particular, the silicon vacancy (V_{Si}) has been incorporated into photonic structures to overcome the current obstacle of low emission intensity from the defect. In the first part of this thesis, a device fabrication process was developed. Two different processes have been made to realize photonic structures in 4H-SiC: 1) By utilizing a photoresist mask patterned by photolithography and subsequently transferring the design to the SiC wafer by reactive ion etching (RIE), structures with different morphology have been made. The photoresist thickness was varied to change the structure morphology; 2) The process was performed by depositing a SiO_2 layer with plasma chemical vapor deposition (PECVD) on a SiC. Next, with photolithography, the SiO_2 layer was patterned with a photoresist mask in a reactive ion etching step. The patterned SiO_2 layer was then used as a hard mask for a subsequent RIE step, finalizing the photonic structure. Structures from processes 1) and 2) were implanted with He ions to generate V_{Si}.

The V_{Si} was identified in all the samples via detection of the V1 and V1' zero-phonon lines (ZPLs). The structures fabricated by process 2) were measured in cathodoluminescence (CL) spectroscopy and angle-resolved cathodoluminescence (ARCL) spectroscopy. The CL measurements revealed nearly 2-fold enhancement in the emission intensity of the V_{Si} in the structures compared to that of the wafer. Moreover, the ARCL measurements provided radiation profiles which revealed that the photonic structures behave similarly to a solid immersion lens (SIL).

In addition, we developed a method for fabrication Schottky barrier diodes on top of the photonic structures for charge-state control of the V_{Si}. A thin nickel layer was deposited on the structures with physical vapor deposition (PVD) through a lift-off process with a photoresist mask. CL measurements revealed an enhance-

ment of V_{Si} emission intensity in the depletion region of the Schottky contact, demonstrating the successful charge-state control of the defect.

The work in this thesis is promising for the further development of silicon carbide as a material for quantum technology and other uses. We offer a scalable fabrication process of photonic structures in silicon carbide, structures that enhance the V_{Si} emission intensity and provide the option for charge-state control.

6.1 Suggestions for further work

Important results were found in this work, but unfortunately, the time limit restricted further progress. For the interested reader or the ambitious researcher, some suggestions for further work are listed below.

- The structures fabricated by the PR on SiC process were implanted and the V_{Si} was identified, but a CL mapping of the V_{Si} emission intensity and ARCL measurement of the radiation profiles of the structures were not performed.
- Further development of the PR on SiC process could potentially offer large scale production of SILs. Thus, over-etching and hard-baking of the PR should be explored. Imaging of the PR morphology should also be performed, e.g., by SEM or AFM.
- The height of the structures fabricated by the SiO_2 on SiC process has a theoretical limit of 4-5 μm with the techniques available in the MiNaLab. For further work, a thicker layer of SiO_2 should be used to etch deeper into SiC. Thus, the selectivity of the PR/SiO_2 etch step should be properly determined. The morphology of the PR should also be examined to understand how the sidewalls can be modified, particularly how it changes with post-baking at a hotplate.
- The concentration of V_{Si} was large, so each photonic structure contained many defects. To have exactly one defect in each structure, a lower implantation fluence should be used.
- The process for fabricating Schottky contacts should be further developed, e.g., by making smaller contacts, contacts mounted on the side or contacts which can be manipulated by an external bias.
- CL mapping and ARCL measurements of the smaller structures fabricated by the SiO_2 on SiC process.

Appendix A

Cylindrical waveguide theory

We first start by considering the Maxwell curl equations

$$\nabla \times \vec{H} = j\omega\varepsilon\vec{E} \qquad\qquad \nabla \times \vec{E} = -j\omega\mu\vec{E}, \tag{A.1}$$

and writing the components out in cylindrical coordinates.

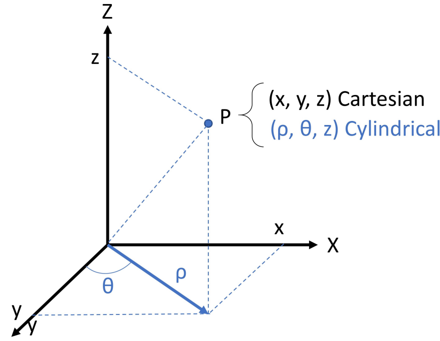

Figure A.1: Cartesian to cylindrical coordinates.

$$\nabla \times \vec{H} = \begin{bmatrix} \frac{1}{\rho}\hat{a}_\rho & \hat{a}_\phi & \hat{a}_z \\ \frac{\delta}{\delta\rho} & \frac{\delta}{\delta\phi} & \frac{\delta}{\delta z} \\ H_\rho & \rho H_\phi & H_z \end{bmatrix} = j\omega\varepsilon(E_\rho\hat{a}_\rho + E_\phi\hat{a}_\phi + E_z\hat{a}_z). \tag{A.2}$$

After writing out $\nabla \times \vec{H}$ and $\nabla \times \vec{E}$ of the two curl equations and dividing out the unit vectors and refining, we end up with six equations:

$$\frac{1}{\rho}\frac{\delta H_z}{\delta \phi} + j\beta H_\phi = j\omega\varepsilon E_\rho \qquad (i) \qquad \frac{1}{\rho}\frac{\delta H_z}{\delta \phi} + j\beta E_\phi = -j\omega\mu H_\rho \qquad (iv)$$

$$-j\beta H_\rho - \frac{\delta H_z}{\delta \rho} = j\omega\varepsilon E_\phi \qquad (ii) \qquad -j\beta E_\rho - \frac{\delta E_z}{\delta \rho} = -j\omega\mu H_\phi \qquad (v)$$

$$\frac{1}{\rho}\left(\frac{\delta \rho H_{phi}}{\delta \rho} - \frac{\delta H_{rho}}{\delta \phi}\right) = j\omega\varepsilon E_z \quad (iii) \qquad \frac{1}{\rho}\left(\frac{\delta \rho E_{phi}}{\delta \rho} - \frac{\delta E_{rho}}{\delta \phi}\right) = -j\omega\mu H_z \quad (vi)$$

Here β is the phase constant and $\frac{\delta \vec{H}}{\delta z} = \frac{\delta \vec{E}}{\delta z} = -j\beta\vec{E}$. We now have the longitudinal components E_z and H_z and the transverse components E_ϕ, E_ρ, H_ϕ and H_ρ. The next step is to use *(i)* through *(vi)* to solve for the individual transverse components. This gives us

$$E_\rho = -\frac{j}{k_c^2}\left(\beta\frac{\delta E_z}{\delta \rho} + \frac{\omega\mu}{\rho}\frac{\delta H_z}{\delta \phi}\right), \tag{A.3}$$

$$E_\phi = -\frac{j}{k_c^2}\left(\frac{\beta}{\rho}\frac{\delta E_z}{\delta \phi} + \omega\mu\frac{\delta H_z}{\delta \rho}\right), \tag{A.4}$$

$$H_\phi = \frac{j}{k_c^2}\left(\frac{\omega\varepsilon}{\rho}\frac{\delta E_z}{\delta \phi} - \beta\frac{\delta H_z}{\delta \rho}\right), \tag{A.5}$$

$$H_\rho = -\frac{j}{k_c^2}\left(\omega\varepsilon\frac{\delta E_z}{\delta \rho} - \frac{\beta}{\rho}\frac{\delta H_z}{\delta \phi}\right), \tag{A.6}$$

where k_c is the cut-off wave number and is given by $k_c^2 = \omega^2\mu\varepsilon - \beta^2$ and k is the wave number and is given by $k^2 = \omega^2\mu\varepsilon$. We can now define transverse electric (TE) waves as waves having no electric field vector component in the z-direction ($E_z = 0$) and similarly transverse magnetic (TM) waves as having no magnetic field vector component in the z-direction ($H_z = 0$). We now want to find the modes of the TE and TM waves.

TE modes

Remembering that we have $E_z = 0$ the problem of finding the TE modes is reduced to the eigenvalue problem

$$\nabla^2 H_z + k^2 H_z = 0, \tag{A.7}$$

which is a linear partial differential equation known as the Helmholtz equation. Solving this in cylindrical coordinates is a tedious process, but with the help of seperation of variables and clever thinking we end up with

$$H_z = J_n\left(k_c \rho\right)\left(A \sin(n\phi) + B \cos(n\phi)\right) e^{-j\beta z}, \qquad n = 0, 1, 2, ... \tag{A.8}$$

where $J_n(k_c P)$ is a Bessel's function of the first order, and the $e^{-j\beta z}$ term is included for the z-direction. At $\rho = a$ (if we let a be the radius of the waveguide), the tangential component of the E-field will be zero, namely $E_z = 0$. Then insert the new H_z into (4) and remembering that $E_z = 0$, and this combined with the boundary condition we have

$$0 = E_\phi(\rho, \phi, z) = \frac{j\omega\mu}{k_c}\left(A \sin(n\phi) + B \cos(n\phi)\right) J_n'(k_c a) e^{-j\omega z}.$$

In order for the equality to be true, $J_n'(k_c a) = 0$, which means that $k_{c_{n,m}} = \frac{P'_{n,m}}{a}$, where $P'_{n,m}$ is the m'th root of J_n'. We can now define a new propagation constant $\beta_{n,m} = \sqrt{k^2 - k_c^2}$ with this constraint. From this we also find the cut-off frequency

$$f_c = \frac{k_c}{2\pi\sqrt{\mu\varepsilon}} = \frac{P_{n,m}}{2\pi a\sqrt{\mu\varepsilon}}. \tag{A.9}$$

The general equations (A.3) to (A.6) can now be written specifically for the TE mode:

$$E_\phi = \frac{j\omega\mu}{k_c}\left(A \sin(n\phi) + B \cos(n\phi)\right) J_n'(k_c a) e^{-j\omega z} \tag{A.10}$$

$$E_\rho = -\frac{j\omega\mu n}{k_c^2}\left(A \cos(n\phi) - B \sin(n\phi)\right) J_n(k_c a) e^{-j\omega z} \tag{A.11}$$

$$H_\phi = -\frac{j\beta n}{k_c^2}\left(A \cos(n\phi) + B \sin(n\phi)\right) J_n(k_c a) e^{-j\omega z} \tag{A.12}$$

$$H_\rho = -\frac{j\beta}{k_c}\left(A \sin(n\phi) + B \cos(n\phi)\right) J_n'(k_c a) e^{-j\omega z} \tag{A.13}$$

$\frac{E_\rho}{H_\phi} = \frac{-E_\phi}{H_\rho} = \frac{\eta k}{\beta} = Z_{TE}$ is the wave impedance of the TE mode.

TM modes

This time $H_z = 0$ and we have to solve the Helmholtz equation for E_z. The procedure is much of the same, and we end up with

$$k_c = \frac{P_{n,m}}{a}, \tag{A.14}$$

$$\beta_{n,m} = \sqrt{k^2 - k_c^2} = \sqrt{k^2 - \left(\frac{P_{n,m}}{a}\right)^2}, \tag{A.15}$$

and the electric and magnetic field components:

$$E_\rho = -\frac{j\beta}{k_c} = (A\sin(n\phi) + B\cos(n\phi))\, J_n'(k_c\rho)e^{-j\beta z} \tag{A.16}$$

$$E_{phi} = -\frac{j\beta n}{k_c^2}\,(A\cos(n\phi) - B\sin(n\phi))\, J_n(k_c\rho)e^{-j\beta z} \tag{A.17}$$

$$H_{rho} = \frac{j\omega\varepsilon n}{k_c^2\rho}\,(A\cos(n\phi) - B\sin(n\phi))\, J_n(k_c\rho)e^{-j\beta z} \tag{A.18}$$

$$H_\phi = -\frac{j\omega\varepsilon}{k_c} = (A\sin(n\phi) + B\cos(n\phi))\, J_n'(k_c\rho)e^{-j\beta z} \tag{A.19}$$

As earlier, $\frac{E_\rho}{H_\phi} = \frac{E_\phi}{H_\rho} = \frac{\eta\beta}{k} = Z_{TM}$ is the wave impedance of the TM mode.

Now we have the tools to make some calculations on a given material. In order to calculate the cut-off frequency and TE and TM modes for SiC, we need the Bessel function zeros [77]. The first few roots for the $J_{n,m}$ and $J'_{n,m}$ first order Bessel functions are found in table A.1 and A.2 below.

Table A.1: Zeros for $J_{n,m}$

n	J_0	J_1	J_2	J_3
1	2.4048	3.8317	5.1356	6.3802
2	5.5201	7.0156	8.4172	9.7610
3	8.6537	10.1735	11.6198	13.0152

Table A.2: Zeros for $J'_{n,m}$

n	J_0	J_1	J_2	J_3
1	3.8317	1.8412	3.0542	4.2012
2	7.0156	5.3314	6.7061	8.0152
3	10.1735	8.5363	9.9695	11.3459

Appendix B

CASINO simulations

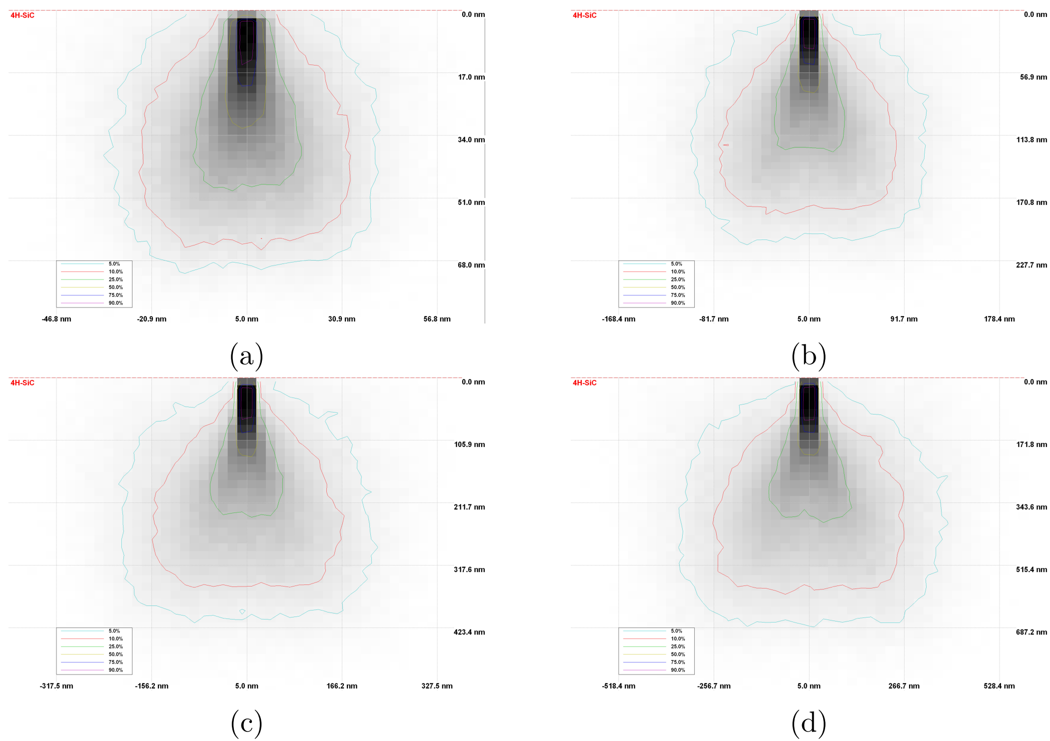

Figure B.1: Monte carlo simulations of electron tracjectories in 4H-SiC at acceleration voltage of (a) 2.5 kV, (b) 5 kV, (c) 7.5 kV, (d) 10 kV. The simulations were done in the CASINO v2 software [76].

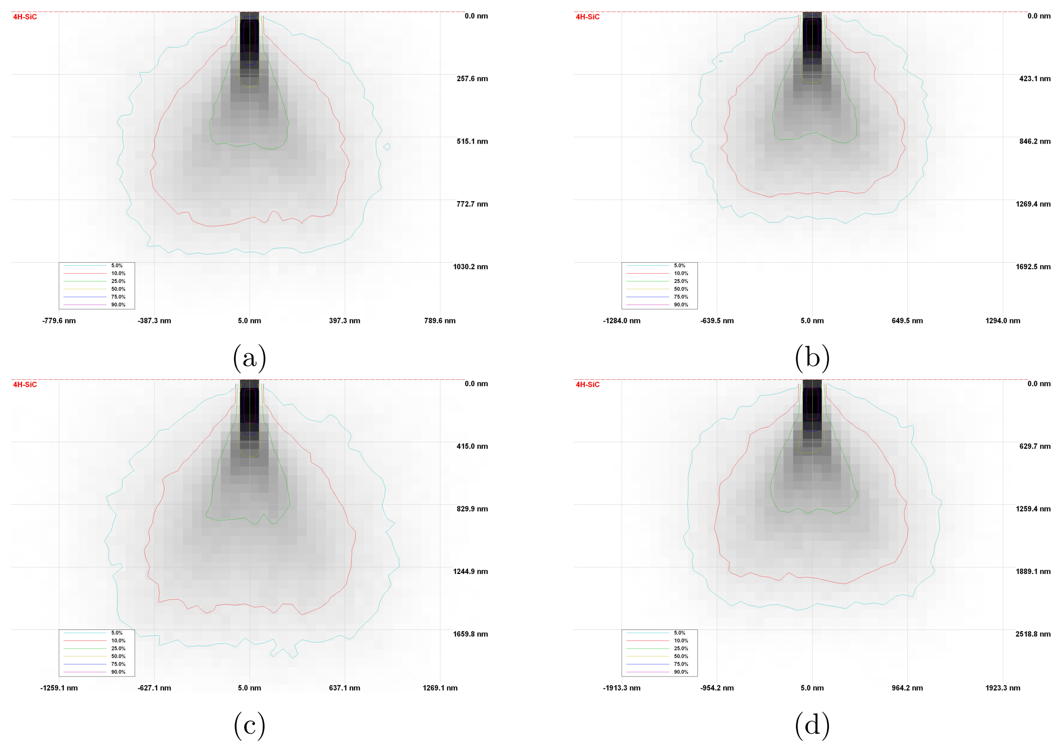

Figure B.2: Monte carlo simulations of electron tracjectories in 4H-SiC at acceleration voltage of (a) 12.5 kV, (b) 15 kV, (c) 17.5 kV, (d) 20 kV. The simulations were done in the CASINO v2 software [76].

Appendix C

Radiation profiles of structures with r=3 μm and r=2 μm

3 μm pillars

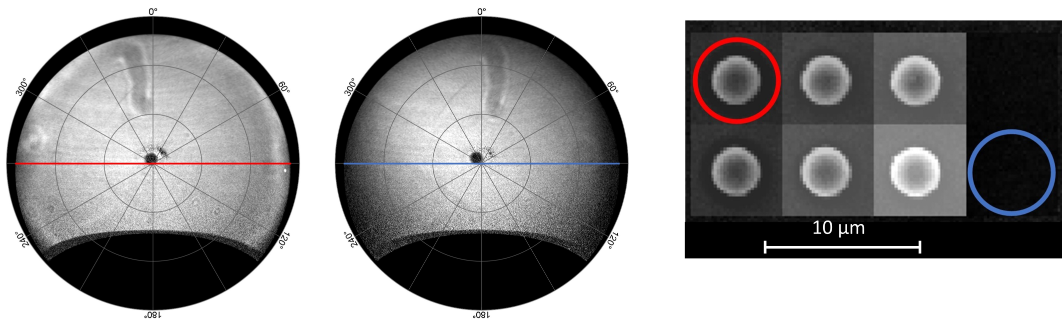

Figure C.1: With 700 nm longpass filter

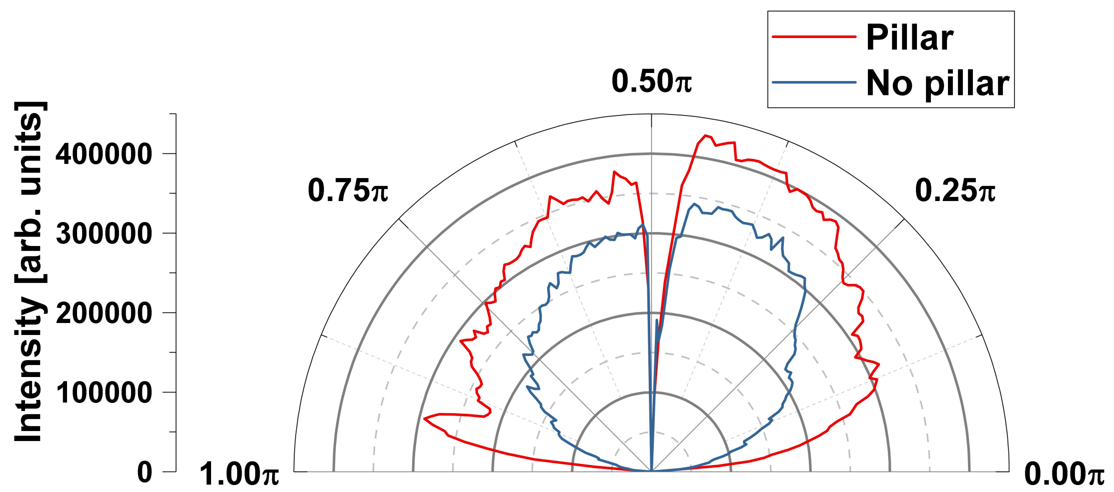

Figure C.2: With 700 nm longpass filter

2 μm pillars

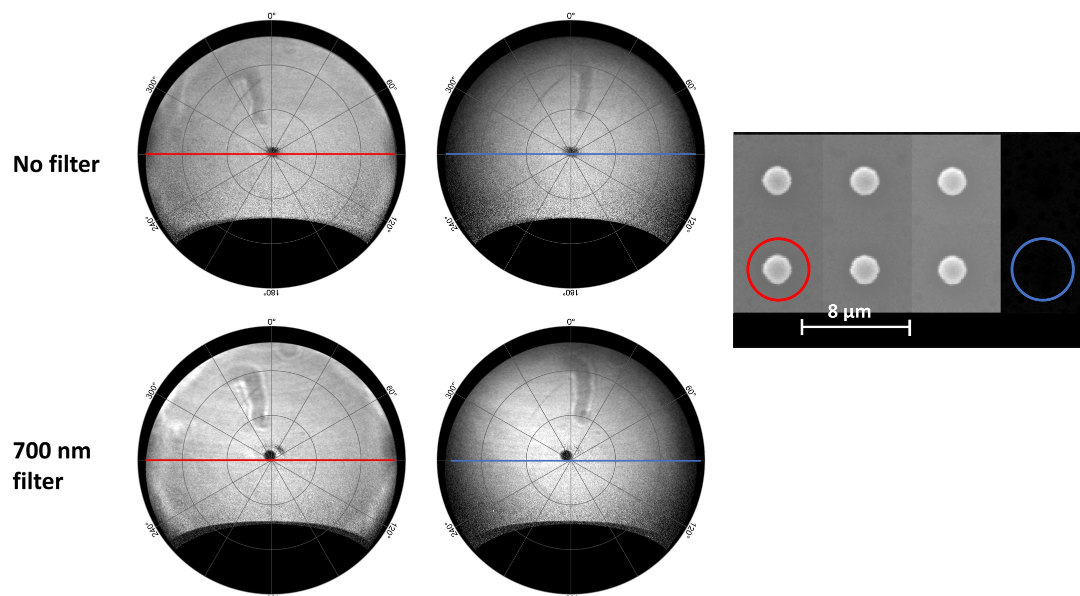

Figure C.3: No filter

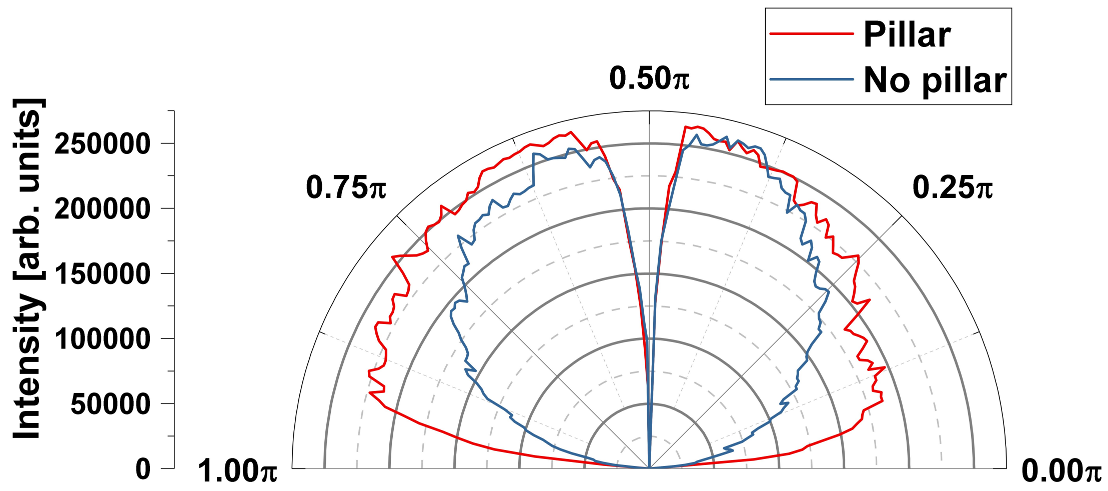

Figure C.4: No filter

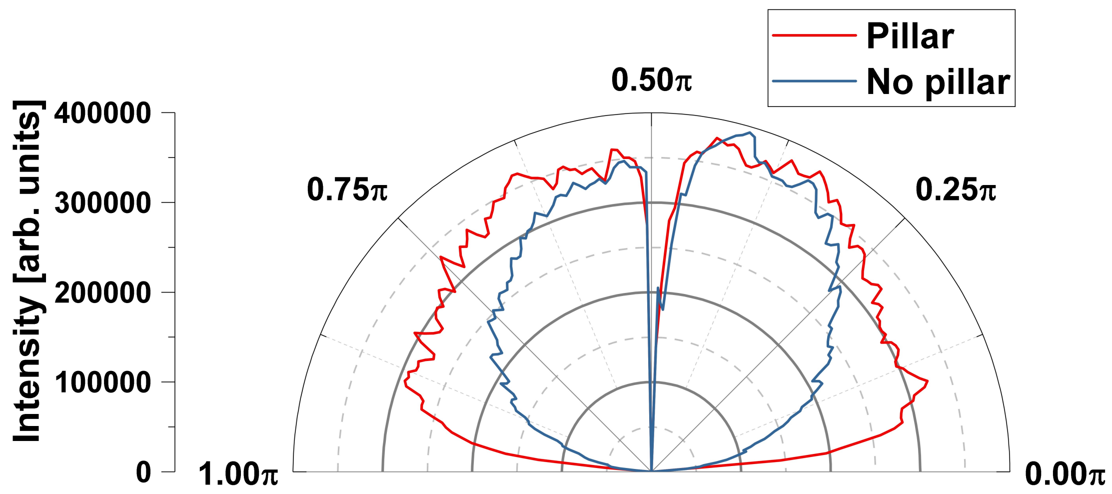

Figure C.5: With 700 nm longpass filter

Bibliography

[1] M. Riordan, *The Lost History of the Transistor*, edited by I. spectrum, (2004) https://spectrum.ieee.org/tech-history/silicon-revolution/the-lost-history-of-the-transistor.

[2] G. E. Moore, Electronics **38**, 114–117 (1965).

[3] S. E. P. Wood, “Sequential 3D Cyclic ADC”, Master thesis (Oslo, 2021).

[4] M. E. Bathen, “Point defects in silicon carbide for quantum technologies: identification, tuning and control”, PhD thesis (Oslo, 2020).

[5] A. Einstein, Annalen der Physik **322** (1905).

[6] A. Beiser, *Concepts of modern physics*, 6th ed. (McGraw-Hill, 2003).

[7] A. G. J. MacFarlane, J. P. Dowling, and G. J. Milburn, Philosophical transactions of the Royal Society of London **361**, 1655–1674 (2003).

[8] R. P. Feynman, International Journal of Theoretical Physics **21**, 467–488 (1982).

[9] E. Knill, Nature **463**, 441–443 (2010).

[10] F. Arute, K. Arya, R. Babbush, D. Bacon, J. C. Bardin, R. Barends, R. Biswas, S. Boixo, F. G. S. L. Brandao, D. A. Buell, B. Burkett, Y. Chen, Z. Chen, B. Chiaro, R. Collins, W. Courtney, A. Dunsworth, E. Farhi, B. Foxen, et al., Nature **574**, 505–510 (2019).

[11] L. C. Bassett, A. Alkauskas, A. L. Exarhos, and K.-M. C. Fu, Nanophotonics **8**, 1867–1888 (2019).

[12] M. E. Bathen, A. Galeckas, J. Müting, H. M. Ayedh, U. Grossner, J. Coutinho, Y. K. Frodason, and L. Vines, npj Quantum Information **5**, 1–9 (2019).

[13] M. Widmann, S.-Y. Lee, T. Rendler, N. T. Son, H. Fedder, S. Paik, L.-P. Yang, N. Zhao, S. Yang, I. Booker, A. Denisenko, M. Jamali, S. A. Momenzadeh, I. Gerhardt, T. Ohshima, A. Gali, E. Janzén, and J. Wrachtrup, Nature Materials **14**, 164–168 (2015).

[14] C. F. de las Casas, D. J. Christle, J. Ul Hassan, T. Ohshima, N. T. Son, and D. D. Awschalom, Applied Physics Letters **111**, 262–403 (2017).

[15] M. Radulaski and J. Vuckovic, to appear as a chapter in The Proceedings on Latest Achievements in Physics on the Occasion of the 20th Anniversary of the "Prof. Dr. Marko V. Jaric" Foundation (2018).

[16] N. Iwamoto and B. G. Svensson, in *Defects in Semiconductors*, Vol. 91, edited by L. Romano, V. Privitera, and C. Jagadish, Semiconductors and Semimetals (Elsevier, 2015), pp. 369–407.

[17] D. J. Griffiths, *Introduction to quantum mechanics*, 3rd ed. (Cambridge University Press, 2018).

[18] T. Hiramoto, Nature Electronics **2**, 557–558 (2019).

[19] D. P. DiVincenzo, Fortschritte der Physik **48**, 771–783 (2000).

[20] T. D. Ladd, F. Jelezko, R. Laflamme, Y. Nakamura, J. L. O'Brien, and C. Monroe, Nature **464**, 45–53 (2010).

[21] J. R. Weber, W. F. Koehl, J. B. Varley, A. Janotti, B. B. Buckley, C. G. V. de Walle, and D. D. Awschalom, Proceedings of the National Academy of Sciences **107**, 8513–8518 (2010).

[22] A. Acín, I. Bloch, H. Buhrman, T. Calarco, C. Eichler, J. Eisert, D. Esteve, N. Gisin, S. J. Glaser, F. Jelezko, S. Kuhr, M. Lewenstein, M. F. Riedel, P. O. Schmidt, R. Thew, A. Wallraff, I. Walmsley, and F. K. Wilhelm, New Journal of Physics **20**, 080201 (2018).

[23] A. F. Kockum and F. Nori, in *Fundamentals and Frontiers of the Josephson Effect*, Springer Series in Materials Science (Springer International Publishing, 2019), pp. 703–741.

[24] C. H. Bennett and G. Brassard, Theoretical Computer Science **560**, 7–11 (2014).

[25] O. Goldreich, *Foundations of Cryptography: Volume 1, Basic Tools* (Cambridge University Press, 2001).

[26] N. Gisin, G. Ribordy, W. Tittel, and H. Zbinden, Reviews of Modern Physics **74**, 145–195 (2002).

[27] N. Gisin and R. Thew, Nature Photonics **1**, 165–171 (2007).

[28] M. G. Kuzyk, American Journal of Physics **87**, 325–327 (2019).

[29] C. Degen, F. Reinhard, and P. Cappellaro, Reviews of Modern Physics **89**, 035002 (2017).

[30] S. Castelletto and A. Boretti, Journal of Physics: Photonics **2**, 022001 (2020).

[31] C. Kittel, *Introduction to solid state physics*, 8th ed. (Wiley, 2005).

[32] B. G. Streetman, *Solid state electronic devices*, 7th ed., global ed. (Pearson, 2016).

[33] M. A. Reshchikov and H. Morkoç, Journal of Applied Physics **97**, 061301 (2005).

[34] I. Pelant and J. Valenta, *Luminescence Spectroscopy of Semiconductors* (Oxford University Press, 2012).

[35] P. Debye, Annalen der Physik **17**, 49–92.

[36] P. Debye, Zeitschrift für Physik A **348**, 398–408.

[37] T. Aichele, U. Herzog, M. Scholz, and O. Benson, AIP Conference Proceedings **750**, `10.1063/1.1874555` (2004).

[38] M. W. Doherty, N. B. Manson, P. Delaney, F. Jelezko, J. Wrachtrup, and L. C. Hollenberg, Physics Reports **528**, 1–45 (2013).

[39] A. Beveratos, S. Kühn, R. Brouri, T. Gacoin, J.-P. Poizat, and P. Grangier, The European Physical Journal D **18**, 191–196 (2002).

[40] M. Markham, J. Isoya, J. Achard, N. Mizuochi, R. Kolesov, G. Balasubramanian, J. Tissler, V. Jacques, P. R. Hemmer, F. Jelezko, J. Wrachtrup, P. Neumann, J. Beck, and D. Twitchen, Nature Materials **8**, 383–387 (2009).

[41] P. E. Barclay, K.-M. C. Fu, C. Santori, A. Faraon, and R. G. Beausoleil, Physical Review X **1**, 1–7 (2011).

[42] L. Gordon, J. R. Weber, J. B. Varley, A. Janotti, D. D. Awschalom, and C. G. Van de Walle, MRS Bulletin **38**, 802–807 (2013).

[43] D. J. Christle, A. L. Falk, P. Andrich, P. V. Klimov, J. U. Hassan, N. T. Son, E. Janzén, T. Ohshima, and D. D. Awschalom, Nature Materials **14**, 160–163 (2015).

[44] F. Fuchs, B. Stender, M. Trupke, D. Simin, J. Pflaum, V. Dyakonov, and G. V. Astakhov, Nature Communications **6**, 7578 (2015).

[45] V. Ivády, J. Davidsson, N. T. Son, T. Ohshima, I. A. Abrikosov, and A. Gali, Physical Review B **96**, 161114(R) (2017).

[46] M. E. Bathen and L. Vines, Advanced Quantum Technologies, `10.1002/qute.202100003` (2021).

[47] W. F. Koehl, B. B. Bckley, F. J. Heremans, G. Calusine, and D. D. Aswchalom, Nature **479**, 84–87 (2011).

[48] J. W. Steeds, Physical Review B **80**, 245202 (2009).

[49] Z. Mu, S. A. Zargaleh, H. J. von Bardeleben, J. E. Fröch, H. Cai, X. Yang, J. Yang, X. Li, I. Aharonovich, and W. Gao, Nano Letters **20**, 6142–6147 (2020).

[50] G. Wolfowicz, C. P. Anderson, B. Diler, O. G. Poluektov, F. J. Heremans, and D. D. Awschalom, Science Advances **6**, eaaz1192 (2020).

[51] J. Stark, Annalen der Physik **43**, 965–983 (1914).

[52] E. Hecht, *Optics*, 5th ed., global ed. (Pearson, 2017).

[53] H. Engan, *Waveguide propagation*, tech. rep. (NTNU, Department of Physics, Institutt for elektronikk og telekommunikasjon, Trondheim, Norway, 2006).

[54] M. Radulaski, M. Widmann, M. Niethammer, J. L. Zhang, S.-Y. Lee, T. Rendler, K. G. Lagoudakis, N. T. Son, E. Janzén, T. Ohshima, J. Wrachtrup, and J. Vučković, Nano Letters **17**, 1782–1786 (2017).

[55] F. Sardi, T. Kornher, M. Widmann, R. Kolesov, F. Schiller, T. Reindl, M. Hagel, and J. Wrachtrup, Applied Physics Letters **117**, 22105 (2020).

[56] A. Sipahigil, M. L. Goldman, E. Togan, Y. Chu, M. Markham, D. J. Twitchen, A. S. Zibrov, A. Kubanek, and M. D. Lukin, Physical Review Letters **108**, 143601–143601 (2012).

[57] L. Marseglia, J. P. Hadden, A. C. Stanley-Clarke, J. P. Harrison, B. Patton, Y.-L. D. Ho, B. Naydenov, F. Jelezko, J. Meijer, P. R. Dolan, J. M. Smith, J. G. Rarity, and J. L. O'Brien, Applied Physics Letters **98**, 133107 (2011).

[58] J. P. Hadden, J. P. Harrison, A. C. Stanley-Clarke, L. Marseglia, Y.-L. D. Ho, B. R. Patton, J. L. O'Brien, and J. G. Rarity, Applied Physics Letters **97**, 241901 (2010).

[59] *S1800® series photo resists*, online product manual, Shipley (UK, Marlborough, 2021).

[60] J. Choi, L. Latu-Romain, E. Bano, F. Dhalluin, T. Chevolleau, and T. Baron, Journal of physics D: Applied Physics **45**, 235204 (2012).

[61] L. Jiang, R. Cheung, R. Brown, and A. Mount, Journal of Applied Physics **93**, 1376–1383 (2003).

[62] M. Lazar, H. Vang, P. Brosselard, C. Raynaud, P. Cremillieu, J.-L. Leclercq, A. Descamps, S. Scharnholz, and D. Planson, Superlattices and Microstructures **40**, 388–392 (2006).

[63] M. Lazar, F. Enoch, F. Laariedh, D. Planson, and P. Brosselard, in Materials Science Forum, Vol. 679-680 (2011), pp. 477–480.

[64] M. Ozgur and M. Huff, Journal of Microelectromechanical Systems **26**, 456–463 (2017).

[65] O. Seok, Y.-J. Kim, and W. Bahng, Physica Scripta **95**, 045606 (2020).

[66] M. D. M, "Vacuum Evaporation and Vacuum Deposition", in *Handbook of Physical Vapor Deposition (PVD) Processing*, 2nd ed. (Elsevier, 2010), pp. 195–235.

[67] R. R. Natasha Erdman David C. Bell, *Springer Handbook of Microscopy*, 1st ed. (Springer International Publishing, 2019), pp. 229–318.

[68] T. Coenen, B. J. Brenny, E. J. Vesseur, and A. Polman, MRS Bulletin **40**, 359–365 (2015).

[69] T. Coenen, E. J. R. Vesseur, and A. Polman, Applied Physics Letters **99**, 143103 (2011).

[70] B. J. M. Brenny, T. Coenen, and A. Polman, Journal of Applied Physics **115**, 244307 (2014).

[71] M. Tosa, in *Compendium of Surface and Interface Analysis*, 1st ed. (Springer, 2018).

[72] `https://www.cree.com/`.

[73] *Dry etching*, online product manual, MicroChemicals® (Ulm, Germany, 2021).

[74] *Photoresist removal*, online product manual, MicroChemicals® (Ulm, Germany, 2021).

[75] *The Stopping and Range of Ions in Matter*, `http://www.srim.org/`.

[76] *Monte Carlo Simulation of Electron Trajectory in Solids*, `https://www.gel.usherbrooke.ca/casino/`.

[77] E. W. Weisstein, *Bessel Function Zeros.* MathWorld, `https://mathworld.wolfram.com/BesselFunctionZeros.html`.